Advanced Engineering Research

Theoretical and scientific-practical journal

Vol. 22
no. 3
2022

ISSN 2687-1653

1 Mechanics

2 Machine Building and Machine Science

3 Information Technology, Computer Science, and Management

DOI 10.23947/2687-1653

vestnik-donstu.ru

Theoretical and scientific-practical journal

Published since 1999

Quarterly
July-September 2022

ISSN 2687-1653
DOI: 10.23947/2687-1653

Advanced Engineering Research

Vol. 22, no. 3

Founder and publisher – Federal State Budgetary Educational Institution of Higher Education Don State Technical University (DSTU)

The journal was known as Vestnik of Don State Technical University (until August 2020)

Included in the list of peer-reviewed scientific editions where the basic research results of doctoral, candidate's theses should be published (State Commission for Academic Degrees and Titles List) in the following research areas:

01.02.01 – Analytical Mechanics (Engineering Sciences)
01.02.04 – Deformable Solid Mechanics (Engineering Sciences)
01.02.04 – Deformable Solid Mechanics (Physicomathematical Sciences)
01.02.06 – Dynamics, Strength of Machines, Gear, and Equipment (Engineering Sciences)
05.02.02 – Engineering Science, Drive Systems and Machine Parts (Engineering Sciences)
05.02.04 – Machine Friction and Wrear (Engineering Sciences)
05.02.07 – Technology and Equipment of Mechanical and Physicotechnical Processing (Engineering Sciences)
05.02.08 – Engineering Technology (Engineering Sciences)
05.02.10 – Welding, Allied Processes and Technologies (Engineering Sciences)
05.02.11 – Testing Methods and Diagnosis in Machine Building (Engineering Sciences)
05.13.11 – Software and Mathematical Support of Machines, Complexes and Computer Networks (Engineering Sciences)
05.13.17 – Foundations of Information Science (Engineering Sciences)
05.13.18 – Mathematical Simulation, Numerical Methods and Program Systems (Engineering Sciences)

The journal is indexed and archived in the Russian Science Citation Index (RSCI), in the International Database EBSCO (Academic Search Ultimate Magazines and Journals), Dimensions, CyberLeninka, ROAD, GoogleScholar. The journal is a member of Directory of Open Access Journals (DOAJ), Association of Science Editors and Publishers (ASEP) and CrossRef.

Certificate of mass media registration ЭЛ № ФС 77 – 78854 of 07.08.2020 is issued by the Federal Service for Supervision of Communications, Information Technology, and Mass Media

The issue is prepared by:

Inna V. Boyko, Marina P. Smirnova (English version)

Founder's, Publisher's and Printery Address:

Gagarin Sq. 1, Rostov-on-Don, 344003, Russia. Phone: +7 (863) 2-738-372

E-mail: vestnik@donstu.ru http://vestnik-donstu.ru/

CONTENTS

MECHANICS

UDC 539.374
https://doi.org/10.23947/2687-1653-2022-22-3-180-192

Original article

Selection and Identification of a Model of Elasto-Viscoplasticity of the Filled Fluorocomposite according to Free and Constrained Compression Tests

Dmitriy S. Petukhov ✉, **Anatoliy A. Adamov**, **Ilya E. Keller**
Institute of Continuous Media Mechanics UrB RAS, 1, Academika Koroleva St., Perm, Russian Federation
✉ petuhovds@mail.ru

Abstract

Introduction. Properties of filled composites based on polytetrafluoroethylene allow them to work at high contact pressures, reciprocating nature of shear loads, and in a wide temperature range. Due to this, they are used as antifriction layers of bearing parts with ball segment. To simulate the mechanical behavior of such materials under operating conditions, adequate constitutive equations of elasto-viscoplasticity and methods of their identification according to the data of basic experiments are needed.

Materials and Methods. The tensor-linear model of elasto-viscoplasticity should be identified according to the data of tests on free compression of samples. They were subjected to loading up to a maximum deformation of 10 %, allowed to remain, unloaded, and then, a similar loading cycle up to 160 MPa under constrained compression was carried out. The experiment with a composite based on polytetrafluoroethylene filled with 40 wt. % fine bronze, was conducted at room temperature. Tests for constrained compression were performed for two values of the strain rate, and for free compression — for three values of the strain rate in the range of $10^{-6} - 10^{-3}\ s^{-1}$. For the description, two models of elasto-viscoplasticity were considered, representing modifications of Swain and Kletschkowski's models and corresponding to the connection of a viscoelastic or elastic nonlinear viscous element with a plastic or endochronic element. An integral operator with a Kohlrausch kernel was considered as a viscoelastic element.

Results. The results of the constrained compression tests made it possible to separate the elastic relationship of volumetric deformations and average stresses from the constitutive relations. The data of free compression cycles at different strain rates were used to determine the material constants of the model. For this purpose, an efficient search algorithm based on the simplex method of minimizing the discrepancy was implemented. Both models discovered the importance of the plastic component (independent of the deformation rate) for a qualitative description of the stress cycling that accompanied the cyclic deformation, as well as their dependence on the strain rate.

Discussion and Conclusions. Both models of elasto-viscoplasticity described correctly the behavior of the studied fluorocomposite under loading conditions close to the operating conditions of the antifriction layers of the bearing parts with ball segment. They can be considered as a basis for their further generalization, taking into account the dependence on temperature.

Keywords: elasto-viscoplasticity, constitutive equations, filled fluorocomposite, identification, free and constrained compression, trapezoidal loading.

Acknowledgments. The authors are grateful to A. V. Khokhlov, leading researcher of Institute of Mechanics, Lomonosov Moscow State University, for a fruitful discussion of the work.

Funding information. The research is done with the financial support from RFFI and Perm Krai within the frame of research project no. 20–48–596012.

For citation. D. S. Petukhov, A. A. Adamov, I. E. Keller. Selection and Identification of a Model of Elasto-Viscoplasticity of the Filled Fluorocomposite according to Free and Constrained Compression Tests. Advanced Engineering Research, 2022, vol. 22, no. 3, pp. 180–192. https://doi.org/10.23947/2687-1653-2022-22-3-180-192

Introduction. Properties of filled composites based on polytetrafluoroethylene (PTFE) allow them to work in a wide temperature range at high contact pressures and reciprocal sliding on the counterbody. Due to this, they are used as antifriction layers of bearing parts with a ball segment[1, 2]. PTFE as a base for antifriction polymer composites in a wide temperature range shows high stability of properties and exceptionally low coefficients of friction, sliding and rest. The introduction of fillers helps to significantly increase the wear resistance, stiffness and yield strength, as well as reduce the creep of the composite without marked increase in the friction coefficients. The rheological properties of the antifriction material should provide feasibility during the operation of the product in the temperature range from less than –50 to +50 °C:

– at calculated values of the compressive load of at least 60 MPa;

– at its peak values up to 150 MPa;

– at a normalized range of cyclic shear deformations.

The predictability of changes in the properties and thickness of the antifriction layer under its hinge mounting also matters.

During the operation of the materials under consideration, it is required to assess the performance of antifriction layers of the support parts with a ball segment, to predict the resource for the entire service life (up to 50 years). To do this, you need to construct and identify adequate constitutive equations of elasto-viscoplasticity according to the data of basic experiments. Models describing the rheological behavior of filled fluorocomposites are also important for calculating the operational properties of shaft seals and rods in high-power diesel engines[3]. To calculate the behavior of products under load during installation (for short periods of time), it is important that the models correctly describe the plastic (elastoplastic, viscoplastic) properties of the material. To calculate the behavior of products during operation (for long periods of time), it is required to adequately represent the phenomena of relaxation, creep, and cyclic creep (ratcheting).

Rheological models of filled fluorocomposites describing cycles of loading, holding, and unloading in wide ranges of time and strain rates are rarely found in the literature. We can specify only work [1] that meets all these requirements. It proposes a model corresponding to the parallel connection of endochronic and nonlinear viscous elements. This model describes all uniaxial tensile tests[4] at room temperature. It is about:

– loading curves up to 0.08 strain with strain rates $10^{-4} - 10^{-2}\,s^{-1}$;

– relaxation curves for 10 h with constant strain of 0.03–0.08;

– hysteresis loops in the load cycle up to 0.1 strain, short-term hold and unloading with subsequent hold.

[1] EAD 050009-00-0301. Spherical and cylindrical bearing with special sliding material made of fluoropolymer. EOTA. Product regulation. URL: https://www.nlfnorm.cz/en/ehn/6189

[2] Stanton JF, Roeder CW, Campbell TI. Appendix C: Friction and Wear of PTFE Sliding Surfaces. NCHRP Report 432: High-Load Multi-Rotational Bridge Bearings. Washington, DC: TRB; 1999. 413 p.

[3] Hai Sui, Heiko Pohl, Achim Oppermann, et al. Material and Computational Analysis of PTFE Seals. SAE Paper Series. 1995:951055. URL: https://www.sae.org/publications/technical-papers/content/951055/?src=2001-01-1118

[4] Material and Computational Analysis of PTFE Seals.

One-dimensional constitutive equations containing seven material constants were written, as well as their tensor generalization for the geometrically linear case. The authors point out that the endochronic plasticity model makes it possible to describe a continuous change in plastic deformation during loading and unloading. This is typical for polymer materials and is not typical for metals. Note that in [1], the endochronicity parameter was not used, which allowed regulating the characteristic range of transition to the plastic state. In addition, the paper[5] describes similar curves for temperatures up to 120 °C, and strain rates in the range of 10^{-4}–100 s^{-1}, relaxation curves with a sharp increase in temperature up to 100 °C, and relaxation curves under uniaxial compression.

A tensor geometrically nonlinear model is presented in [2]. It describes the behavior of filled fluorocomposites under various monotonic and cyclic loading histories in various stress states and at arbitrary temperatures. A viscoplastic rheological element in a series connection with a viscoelastic one is taken into account. On the whole, this model satisfactorily describes the curves corresponding to the experiments [1], but it is much more complicated and requires fourteen material constants. In [3], the model [4] is used to describe microindentation cycles of a filled fluorocomposite. The rheological block diagram is similar to [2], but it takes into account the relaxation time spectrum of the viscoelastic element. In [3], the model [4] is used to describe microindentation cycles of a filled fluorocomposite. The rheological block diagram is similar to [2], but it takes into account the relaxation time spectrum of the viscoelastic element.

The model [5] was designed to describe features of the elastoplastic behavior of solid polymers under cyclic uniaxial loading. The evolutionary equations for its internal variable, stresses and plastic deformations, had nonlinear cross-connections, therefore, the model did not correspond to any rheological structural scheme. The measure of internal time characteristic of the endochronic theory of plasticity was used. Twenty-one constants were required to identify the model.

The nonlinear one-dimensional Maxwell-type viscoelastic plasticity model [6–9] contains only two material functions. It describes incomplete recovery of deformations in the load-unloading cycle and cyclic creep (ratcheting) with asymmetric loading cycles. Nonlinear viscoelasticity models with fractional integro-differentiation operators are characterized by flexibility with a small number of material constants and functions [7]. It is necessary to investigate the applicability of such nonlinear models to describe the behavior of polymer materials in the loading and unloading cycle with holds [10–13]. Papers [14, 15] are devoted to the identification of linear models of viscoelasticity based on the results of indentation tests. In [16, 17], the dynamic mechanical analysis results are used for this purpose, but the significant nonlinearity of the materials studied in this work does not allow using this technique. Ratcheting of PTFE composites is experimentally investigated in [18, 19], but there is no mathematical description of the results.

Paper [8] presents a method for identifying a model of isotropic elastoplastic behavior of filled composites based on PTFE and ultrahigh molecular weight polyethylene based on experimental data on free and constrained compression. Due to the peculiarities of the rheology of plastics [9], the methods [10] are applicable to them. This approach makes it possible to determine:

– the elastic volume compressibility function;

– the hardening function for shear elastoplastic properties within the framework of the theory of plastic flow.

Thus, the operating conditions of the products in question, the mechanical properties of polymer materials, and the presented literature analysis serve as the basis for further research.

Let us highlight the basic test for free compression of cylindrical samples of 20×20 mm. It consists of load cycles up to 0.1 deformation, a short-term hold of fifteen minutes, and unloading with a subsequent hold of fifteen minutes. In this way, data can be determined to describe elastic, plastic and viscous components of deformation, relaxation and reverse

[5] Material and Computational Analysis of PTFE Seals.

creep with residual deformations. A similar definition of hardness is provided by the standard[6]. Loading is performed at three strain rates in the range of 10^{-6}–10^{-3} s^{-1}. Besides, the samples are tested for constrained compression to a stress of 160 MPa at two strain rates from the same range. All tests are repeated for values from the operating temperature range of the polymer material. These data should be sufficient to identify a suitable model of elasto-viscoplastic compressible material with nonlinear elastic compressibility.

First of all, we are interested in the possibilities of describing experimental data at room temperature with the simplest elasto-viscoplasticity models of the type proposed in [1] and [4], which differ in structural schemes.

Materials and Methods. A composite based on PTFE PN 90 filled with 40 wt. % of fine bronze was chosen as the simulated material. Cylindrical samples with a diameter and height of 20 mm were made by pressing and sintering a mixture of powders. The following experiments were conducted to select and then identify the model:

– for constrained compression with a single nonzero component of the strain tensor;

– for free compression with a single nonzero component of the stress tensor.

In the first case, friction along the lateral boundary was excluded by lubrication, in the second — by a thin film of PTFE and grease.

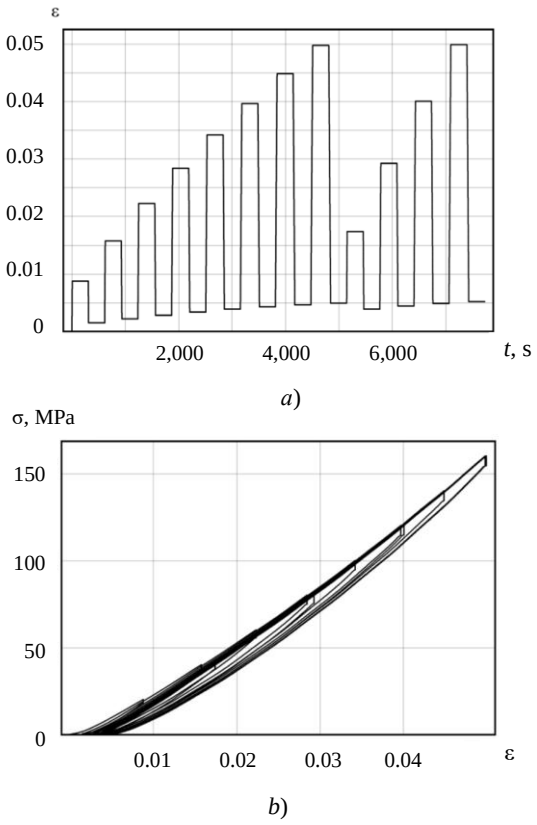

Fig. 1. Cyclic tight compression test: *a* — program; *b* — hysteresis curve

The experiments were aimed at identifying irreversible volumetric deformations and volume-elastic properties of the material. The first test was cyclic constrained compression with increasing amplitude (Fig. 1 *a*). It set the value of the deformation rate $\dot{\varepsilon} = 2.5\times10^{-3}\ s^{-1}$ and the pause between unloading and loading for 300 s. During the first few cycles, a residual volume strain equal to approximately 5×10^{-3} accumulated (Fig. 1). It changed slightly when the sample was held in the unloaded state.

[6] GOST 4670-2015 (ISO 2039-1:2001). Plastics. Determination of hardness. Ball indentation method. Interstate Council for Standardization, Metrology and Certification. Moscow: Standartinform; 2016. 10 p. (In Russ.)

Further, compression tests were carried out up to 160 MPa with a significantly slower strain rate $\dot{\varepsilon} = 2.5 \times 10^{-5}\ s^{-1}$ and subsequent unloading (Fig. 2 *a*):

– of undeformed sample (1);

– of the same sample repeatedly (2);

– of the sample after the cyclic test shown in Figure 1 (3).

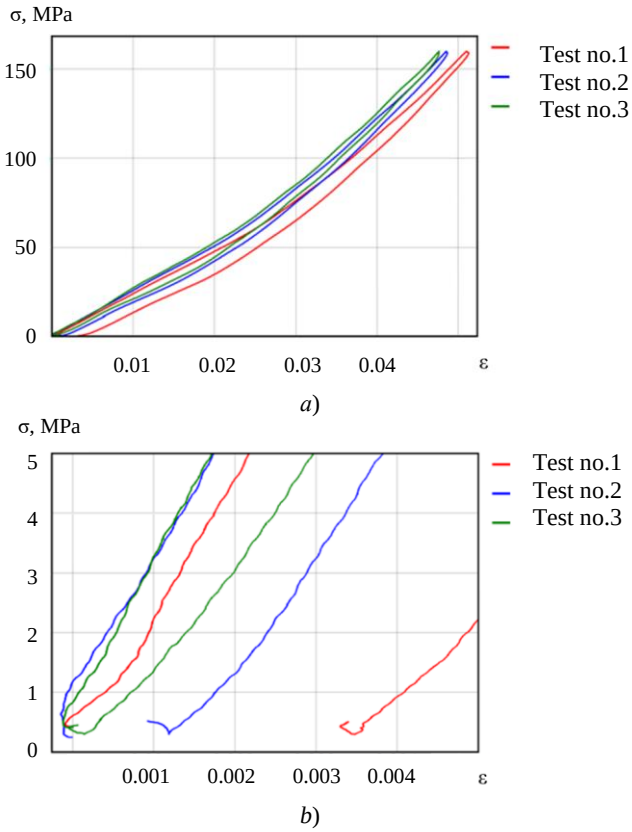

Fig. 2. Slow tight compression tests: *a* — loading diagrams; *b* — initial and final sections of diagrams

Tests of the same sample were carried out in a day.

As can be seen in Figure 2 *b*, in the experiment with a new sample, the maximum residual strain of about 3.5×10^{-3} is observed. On repeated testing, it amounted to 1×10^{-3}. In the third test, there is no residual strain. The properties of the material under cyclic constrained compression are accompanied by a transient irreversible process and are stabilized in several cycles.

The bulk properties were determined from the third test (Fig. 2 *a*), in which there are no residual strains. In this paper, bulk strains are assumed to be nonlinearly elastic. The data is described by a quadratic dependence:

$$\sigma = M(\varepsilon)\varepsilon; \quad M(\varepsilon) = a_0 + a_1\varepsilon; \quad a_0 = 2.4\ \text{hPa}; \quad a_1 = 22.1\ \text{hPa}. \tag{1}$$

Here, σ, ε — axial components of the Cauchy stress tensors and logarithmic strains; M — constrained compression modulus, which is related to the bulk compression modulus K by the ratio:

$$M(\varepsilon_v) = 3\frac{K(\varepsilon_v)\left(3K(\varepsilon_v) + E_\infty\right)}{9K(\varepsilon_v) - E_\infty}, \tag{2}$$

where E_∞ — equilibrium Young's modulus (independent of bulk strain); $\varepsilon_v = \varepsilon_{ii}$, ε_{ij} — components of the logarithmic strain tensor.

Value $E_\infty = 690\ \text{MPa}$ was obtained with the slope of the curve $\sigma(\varepsilon)$ under uniaxial compression in the vicinity of $\sigma = 1\text{MPa}$ and relaxation 8.65 %.

Using (1), (2) and 9.38 % correction for the compliance of the machine in the tight compression test, it is possible to obtain the desired dependence $K(\varepsilon_v)$, which differs slightly (maximum by 0.03 %) from linear:

$$\sigma_m = K(\varepsilon_v)\varepsilon_v; \quad K(\varepsilon_v) = b_0 + b_1\varepsilon_v; \quad b_0 = 2.1\,\text{hPa}; \quad b_1 = 22.2\,\text{hPa}, \tag{3}$$

where $\sigma_m = \frac{1}{3}\sigma_{ii}$, σ_{ij} — components of the Cauchy stress tensor.

Experiments to determine the relationship between average stress and volume strain were carried out on samples previously tested by constrained compression with irreversible volume strain. The same applies to the free compression experiments described below and required to determine the relationship of the deviatory parts of stress and strain tensors. As a result, the model reflected the properties of the compacted material. In production, processes associated with irreversible bulk strain occur under the crimping of a layer of antifriction polymer material during the assembly of the structure of the support part and do not affect the further behavior of the material.

Uniaxial compression tests were carried out to determine the relationships between the deviatory parts of stress and strain tensors. Figure 3 shows the results of experiments for three values of strain rates $\dot{\varepsilon} = 4.63\times10^{-6}\,\text{s}^{-1}$, $2.35\times10^{-5}\,\text{s}^{-1}$, $2.27\times10^{-3}\,\text{s}^{-1}$. Further, the data from these experiments will be interpreted in the framework of a one-dimensional model. When formulating a three-dimensional model, the elastic volume part can be excluded from these relations.

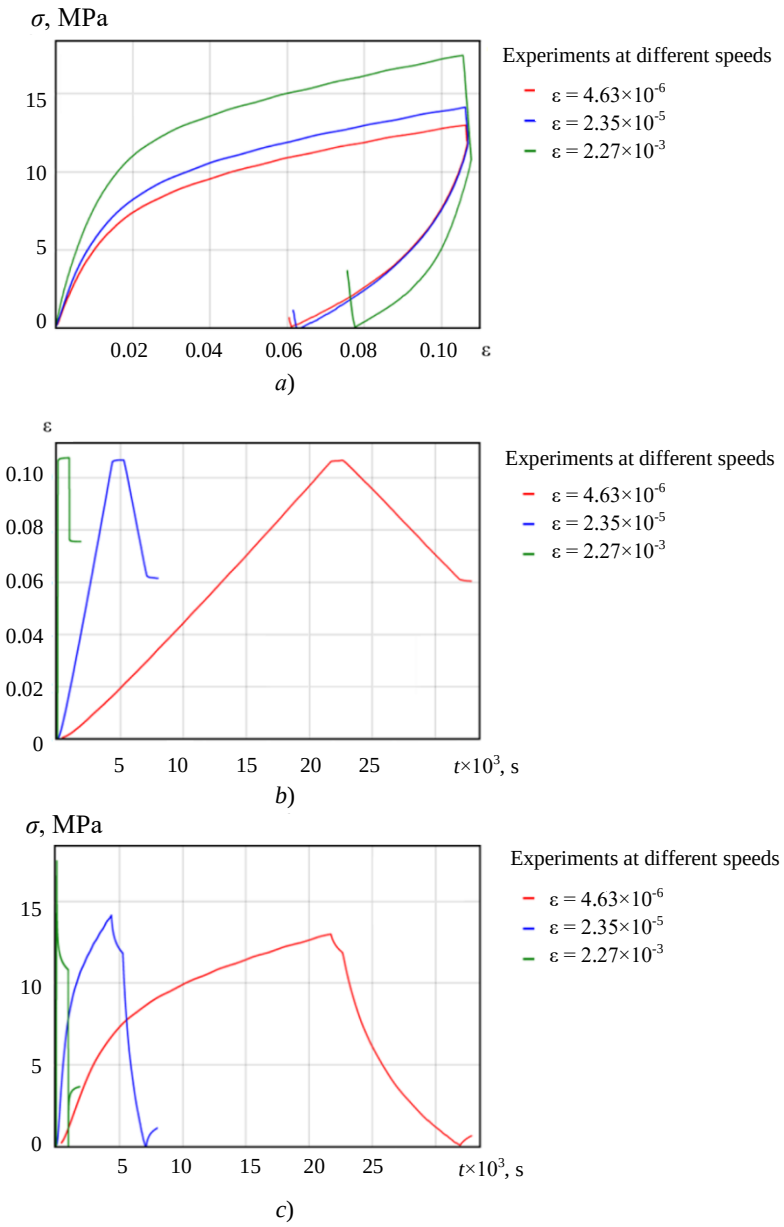

Fig. 3. Uniaxial compression experiment with three different speeds:
a — loading diagrams; *b* — deformation histories; *c* — stress histories

When choosing a suitable model, it turned out that the experimental data in Figure 3 were not described by the relations of a linear viscoelastic medium:

$$\sigma(t)=\int_0^t R(t-\tau)\dot{\varepsilon}(\tau)d\tau = R_0\left(\varepsilon(t)-\int_0^t \Gamma(t-\tau)\varepsilon(\tau)d\tau\right), \tag{4}$$

where $\sigma(t)$, $\varepsilon(t)$ — stress and strain histories used to describe elastomers and polymers [10].

There have been attempts to use expressions for relaxation functions $R(t)$ or relaxation rates $\Gamma(t)$ with a different number of parameters: the sum of exponents, the Robotnov fractional-exponential function[7], the Koltunov kernel[8], the kernel from the work of T. L. Smith[9], the Kohlrausch kernel [10]:

$$R(t)=R_\infty+\sum_{i=1}^{4}R_i\exp(-\alpha_i t);\ \ \Gamma(t)=At^{\alpha-1}\sum_{n=0}^{\infty}\frac{(-\beta)^n t^{n\alpha}}{\Gamma(\alpha(n+1))};\ \ \Gamma(t)=\frac{A\exp(-\beta t^m)}{t^{1-\alpha}};$$
$$R(t)=R_\infty+\frac{R_0-R_\infty}{1+(t/\tau_0)^\alpha};\ \ R(t)=R_\infty+(R_0-R_\infty)\exp\left(-(t/\tau_0)^\alpha\right). \tag{5}$$

Here, R_∞, R_0, R_i, α, β, τ_0 — material constants; Γ — gamma function, as well as monotonic approximation by cubic splines at eight points, whose coordinates served as parameters.

Models were considered, in which, in addition to viscous ones, plastic irreversible deformations were taken into account. Two basic models of this type were investigated.

Basic model 1 (Fig. 4 *a*) is a combination of models [4] and [10] and assumes a sequential connection of three elements.

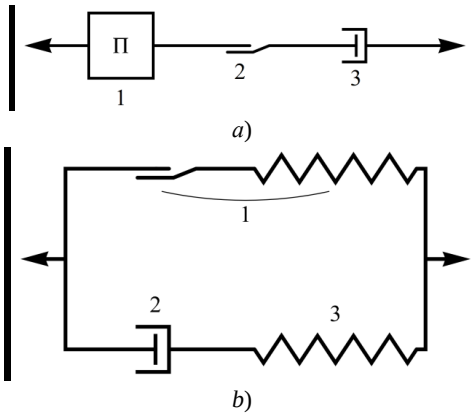

Fig. 4. Block diagrams of basic models: *a* — model 1; *b* — model 2

1. Linear viscoelastic element with Kohlrausch kernel [10]:

$$\varepsilon_1(t)=\int_0^t \Pi(t-\tau)\dot{\sigma}(\tau)d\tau,\qquad \Pi(t)=\frac{1}{R_\infty}+\left(\frac{1}{R}-\frac{1}{R_\infty}\right)\exp\left(-\left(\frac{t}{\tau_0}\right)^\alpha\right), \tag{6}$$

where R, R_∞, τ_0, α — material constants, the first two have the physical meaning of instantaneous and equilibrium modules.

2. Plastic element with linear hardening:

$$\dot{\varepsilon}_2(t)=\begin{cases} k\dot{\sigma}(t), & \sigma\ge\sigma_u\vee\sigma\le-\sigma_u \\ 0, & -\sigma_u\le\sigma\le\sigma_u \end{cases}, \tag{7}$$

where σ_u, k — material constants.

3. Linear-viscous element:

$$\dot{\varepsilon}_3(t)=\eta^{-1}\sigma(t), \tag{8}$$

where η — material constant.

The final expression for strains:

$$\varepsilon(t)=\varepsilon_1(t)+\varepsilon_2(t)+\varepsilon_3(t). \tag{9}$$

[7] Rabotnov YuN. Polzuchest' ehlementov konstruktsii. Moscow: Nauka; 1966. 752 p. (In Russ.)
[8] Koltunov MA. Singulyarnye funktsii vliyaniya v analize relaksatsionnykh protsessov. Prochnost' i plastichnost'. Moscow: Nauka; 1971. P. 640–645. (In Russ).
[9] Smith TL. Ehmpiricheskie uravneniya dlya vyazkouprugikh kharakteristik i vychisleniya relaksatsionnykh spektrov. Vyazkouprugaya relaksatsiya v polimerakh. Moscow: Mir; 1974. P. 44–56. (In Russ).

Model (6)–(9) is solved with respect to strains, therefore, it is convenient to have stress histories for its identification $\sigma(t)$ (Fig. 3 *c*).

The block diagram of basic model 2 (Fig. 4 *b*), borrowed from [1], is a parallel connection of two elements.

1. Endochronic plastic element with nonlinear elastic part:

$$\dot{\varepsilon}_p(t)=\frac{\sigma_1(t)}{Y}\left|\dot{\varepsilon}(t)\right|;\ \sigma_1(t)=A\,\mathrm{sign}\left(\varepsilon(t)-\varepsilon_p(t)\right)\ln\left(1+B\left|\varepsilon(t)-\varepsilon_p(t)\right|\right), \tag{10}$$

where ε_p — an internal parameter that has the meaning of irreversible strain of the element, Y, A, B — material constants.

2. A pair of sequentially connected nonlinear-viscous (2) and linear-elastic (3) elements:

$$\dot{\varepsilon}_2(t)=\frac{1}{\eta}\mathrm{sign}\left(\sigma_2(t)\right)\left|\mathrm{sh}\left(\frac{\sigma_2(t)}{\sigma_0}\right)\right|^k, \tag{11}$$

$$\sigma_3(t)=\sigma_2(t)=c\varepsilon_3(t), \tag{12}$$

where sign — argument sign; η, σ_0, k, c — material constants.

The resulting expression for stresses:

$$\sigma(t)=\sigma_1(t)+\sigma_2(t). \tag{13}$$

Model (10)–(13) is solved with respect to stresses, therefore, it is convenient to have strain histories for its identification $\varepsilon(t)$ (Fig. 3 *c*). Expression $\sigma_1(t)$ in (13) is solved as the solution to a system of algebraic differential equations (10), and $\sigma_2(t)$ — as a system solution (11), (12) taking into account $\varepsilon(t)=\varepsilon_2(t)+\varepsilon_3(t)$.

Research Results. Residual minimization between experimental strain histories (Fig. 3 *b*) and model predictions allowed us to find seven material constants of base model 1:

$$\begin{gathered} R=895\ \text{MPa};\ R_\infty=205\ \text{MPa};\ \tau_0=1.66\times10^3\ \text{s};\ \alpha=0.64; \\ \sigma_u=10.2\ \text{MPa};\ k=0.0095\ \text{MPa}^{-1};\ \eta=9.28\times10^6\ \text{s}. \end{gathered} \tag{14}$$

The simplex method is used as a search procedure. Comparison of the calculated and experimental data is shown in Figure 5.

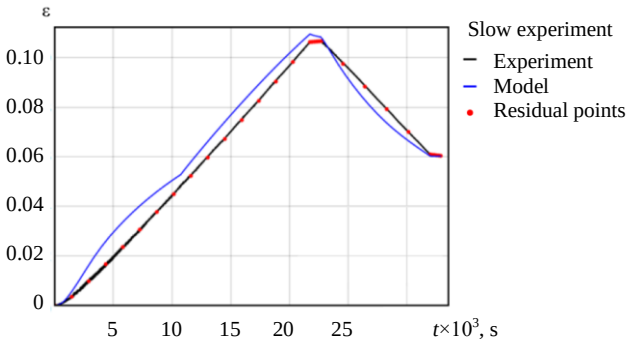

a)

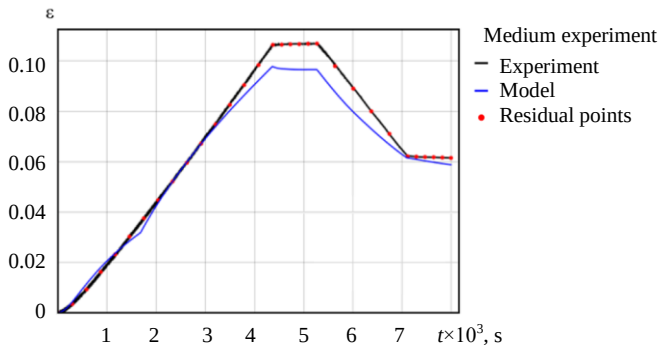

b)

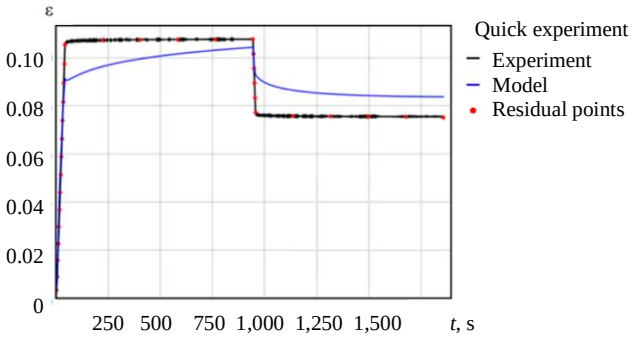

c)

Fig. 5. Comparison of experimental data and base model 1 predictions:

a — $\dot{\varepsilon} = 4.63\times10^{-6}\ \text{s}^{-1}$; b — $\dot{\varepsilon} = 2.35\times10^{-5}\ \text{s}^{-1}$; c — $\dot{\varepsilon} = 2.27\times10^{-3}\ \text{s}^{-1}$

Residual minimization between the experimental stress histories (Fig. 3 *b*) and the model predictions allowed us to detect seven material constants of base model 2:

$$\begin{gathered} \text{Y} = 20.3\,\text{MPa};\ \text{A} = 6.01\,\text{MPa};\ \text{B} = 61.8; \\ \eta = 6.81\cdot10^{6}\ \text{s};\ \sigma_0 = 0.66\,\text{MPa};\ \text{k} = 1.08;\ \text{s} = 681\,\text{MPa}. \end{gathered} \tag{15}$$

Here, strain histories were considered to be given (Fig. 3 *b*). Comparison of the calculated and experimental data is shown in Figure 6.

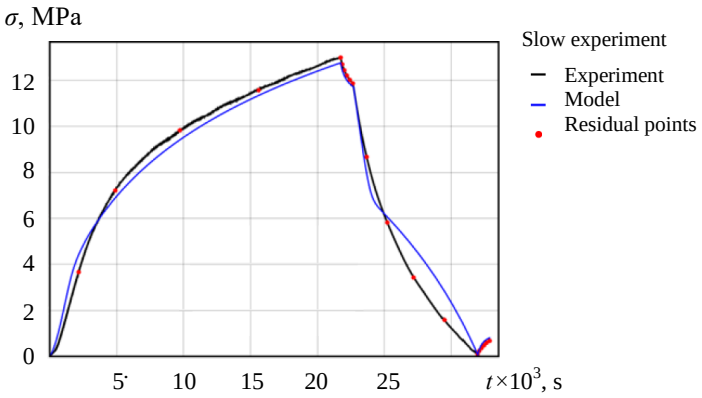

a)

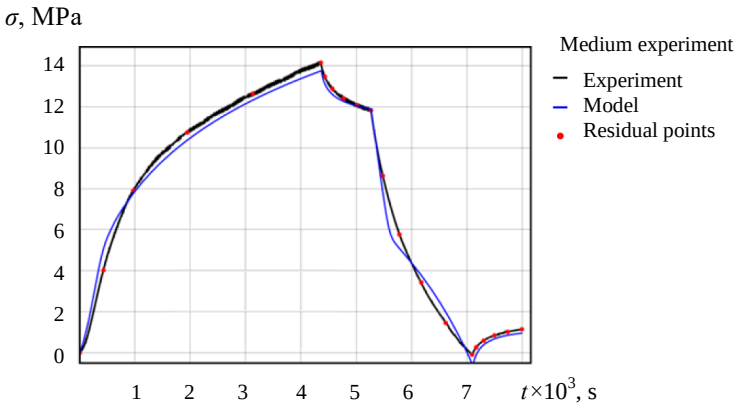

b)

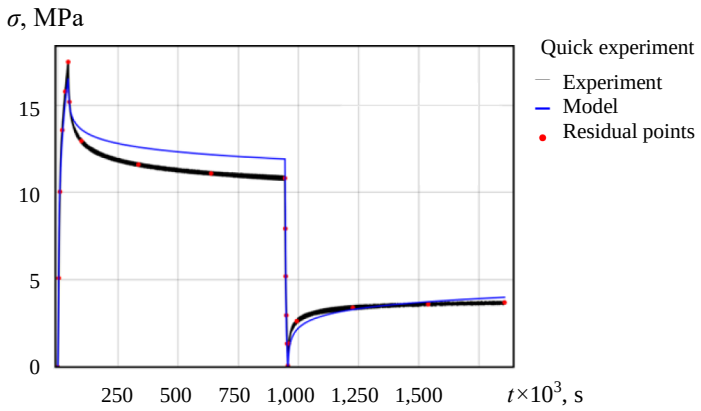

c)

Fig. 6. Comparison of experimental data and predictions of base model 2:
a — $\dot{\varepsilon} = 4.63\times10^{-6}\ \mathrm{s}^{-1}$; *b* — $\dot{\varepsilon} = 2.35\times10^{-5}\ \mathrm{s}^{-1}$; *c* — $\dot{\varepsilon} = 2.27\times10^{-3}\ \mathrm{s}^{-1}$

Discussion and Conclusions. The considered one-dimensional models were generalized to a spatial formulation that assumed isotropy of properties and immutability of the main axes of the strain tensor under loading. To do this, the Cauchy stress tensors and logarithmic deformations were decomposed into spherical and deviatoric parts:

$$\sigma = \sigma_m \mathrm{I} + \mathrm{s},\ \ \varepsilon = \frac{1}{3}\varepsilon_v \mathrm{I} + \mathrm{e}.$$

The relationship between the ball parts σ_m and ε_v is given by expression (3). The relationship between the deviatoric parts s and e is given by the relations generalizing (6)–(9) or (10)–(13) depending on the selection of the base model. These expressions should be rewritten in terms of the histories of the deviatoric parts $\mathrm{s}(\mathrm{t})$ and $\mathrm{e}(\mathrm{t})$, excluding the ball part from uniaxial compression.

As a spatial generalization of the relations (7) for the plastic element of model 1, the plastic flow law associated with von Mises yield criterion, with isotropic linear strain hardening was considered. The connection of deviators will look like this:

$$\mathrm{e}(\mathrm{t}) = \mathrm{e}_1(\mathrm{t}) + \mathrm{e}_2(\mathrm{t}) + \mathrm{e}_3(\mathrm{t});$$

$$\mathrm{e}_1(\mathrm{t}) = \int_0^{\mathrm{t}} \Pi(\mathrm{t}-\tau)\dot{\mathrm{s}}(\tau)\mathrm{d}\tau; \qquad \Pi(\mathrm{t}) = \frac{1}{\mathrm{R}_\infty} + \left(\frac{1}{\mathrm{R}} - \frac{1}{\mathrm{R}_\infty}\right)\exp\left(-\left(\mathrm{t}/\tau_0\right)^{\alpha}\right);$$

$$\mathrm{e}_2 = \frac{9}{4}\mathrm{k}^3\frac{\mathrm{s}:\dot{\mathrm{s}}}{\left(\mathrm{e}_2\right)^2}\mathrm{s}; \quad \mathrm{e}_2(\mathrm{t}) = \int_0^{\mathrm{t}} \dot{\mathrm{e}}_2(\tau)\mathrm{d}\tau; \quad \dot{\mathrm{e}}_2 = \sqrt{\tfrac{2}{3}\dot{\mathrm{e}}_2 : \dot{\mathrm{e}}_2};$$

$$\mathrm{e}_3(\mathrm{t}) = \eta^{-1}\mathrm{s}(\mathrm{t}),$$

where colon means the operation of convolution of tensors $\mathrm{A}:\mathrm{B} = \mathrm{A}_{ij}\mathrm{B}_{ij}$ given by the components in an orthonormal basis.

The relations of the endochronic plasticity theory (10) of model 2 are also generalized in the spirit of von Mises plasticity, which provides the following entry for deviators:

$$\mathrm{s} = \mathrm{s}_1 + \mathrm{s}_2;\ \mathrm{e} = \mathrm{e}_2 + \mathrm{e}_3;$$

$$\dot{\mathrm{e}}_p = \frac{3}{2}\dot{\varepsilon}\frac{\mathrm{s}_1}{\mathrm{Y}}; \quad \dot{\varepsilon} = \sqrt{\tfrac{2}{3}\dot{\mathrm{e}}:\dot{\mathrm{e}}}; \quad \mathrm{s}_1 = \mathrm{dev}\left(\sum_{i=1}^{3}\xi_i \mathrm{n}_i\mathrm{n}_i\right); \quad \xi_i = \mathrm{A}\,\mathrm{sign}\left(\lambda_i\right)\ln\left(1+\mathrm{B}\left|\lambda_i\right|\right);$$

$$\dot{\mathrm{e}}_2 = \frac{3}{2}\frac{1}{\eta}\left|\mathrm{sh}\left(\frac{\sigma_2}{\sigma_0}\right)\right|^{\mathrm{k}}\frac{\mathrm{s}_2}{\sigma_2}; \quad \sigma_2 = \sqrt{\tfrac{3}{2}\mathrm{s}_2 : \mathrm{s}_2};$$

$$\mathrm{e}_3 = \mathrm{c}^{-1}\mathrm{s}_2,$$

where "dev" means a tensor deviator, λ_i, n_i — eigenvalues and eigenvectors of the tensor $\mathrm{e}-\mathrm{e}_p = \lambda_i\ \mathrm{n}_i\ \mathrm{n}_i$.

It should be noted that the authors [1] used a model option with an endochronic parameter [14] equal to one. It seems appropriate to consider this parameter as a material constant, since its influence on the description of transients after changes of loading modes is known.

In the framework of this work, the experiments were carried out on constrained and free compression of a composite based on polytetrafluoroethylene filled with finely dispersed bronze with a mass fraction of 40 %. At the same time, loading, unloading and holding were carried out with different strain rates in the range of 10^{-6}–10^{-3} s^{-1}. The experiments on constrained compression were carried out at pressures corresponding to the peak loads of the antifriction layer in hinges with a spherical segment. The inability of the standard linear viscoelastic model to describe test data for several strain rates was found. Two families of seven-constant models with plastic and nonlinear viscous structural elements that could describe the data of basic experiments were selected and identified. The model with an endochronic element showed great accuracy in describing the data at a high strain rate. The model with a plastic element can be improved if the nonlinearity in the viscous element and nonlinear strain hardening are taken into account, which will require an increase in the number of material constants. The data of these models were generalized to the spatial case for an isotropic material and strain histories with a constant orientation of the trihedron of the main axes.

References

1. Kletschkowski T, Schomburg U, Bertram A. Endochronic Viscoplastic Material Models for Filled PTFE. Mechanics of Materials. 2002;34:795–808. https://doi.org/10.1016/S0167-6636(02)00197-7

2. Bergström JS, Hilbert Jr. LB. A Constitutive Model for Predicting the Large Deformation Thermomechanical Behavior of Fluoropolymers. Mechanics of Materials. 2005;37:899–913. https://doi.org/10.1016/j.mechmat.2004.09.002

3. Stan F, Munteanu AV, Fetecau C. Viscoelastic Characterization of Polytetrafluoroethylene (PTFE) Polymer by Sharp Indentation. AIP Conference Proceedings. 2011;1315:221–226. https://doi.org/10.1063/1.3552445

4. Stan F, Fetecau C. Study of Stress Relaxation in Polytetrafluoroethylene Composites by Cylindrical Macroindentation. Composites Part B: Engineering. 2013;47:298–307. 10.1016/j.compositesb.2012.11.008

5. Menčik J, Li Hong He, Swain MV. Determination of Viscoelastic-Plastic Material Parameters of Biomaterials by Instrumental Indentation. Journal of the Mechanical Behavior of Biomedical Materials. 2009;2:318–325. https://doi.org/10.1016/j.jmbbm.2008.09.002

6. Drozdov AD, J de C Christiansen. Cyclic Elastoplasticity of Solid Polymers. Computational Materials Science. 2008;42:27–35. https://doi.org/10.1016/j.commatsci.2007.06.002

7. Khokhlov AV. Comparative Analysis of Creep Curves Properties Generated by Linear and Nonlinear Heredity Theories under Multi-Step Loadings. Mathematical Physics and Computer Simulation. 2018;21:27–51. https://doi.org/10.15688/mpcm.jvolsu.2018.2.3

8. Khokhlov AV. Applicability Indicators and Identification Techniques for a Nonlinear Maxwell-Type Elasto-Viscoplastic Model using Multi-Step Creep Curves. Herald of the Bauman Moscow State Technical University. Natural Sciences. 2018;6:92–112. http://dx.doi.org/10.18698/1812-3368-2018-6-92-112

9. Khokhlov AV. Identification Techniques for the Nonlinear Maxwell-Type Viscoelastoplastic Model Using Creep Recovery Curves. Problems of Strength and Plasticity. 2018;80:238–254. https://doi.org/10.32326/1814-9146-2018-80-2-238-254

10. Ogorodnikov EN, Radchenko VP, Ungarova LG. Mathematical Models of Nonlinear Viscoelasticity with Operators of Fractional Integro-Differentiation. PNPRU Mechanics Bulletin. 2018;2:147–161. https://doi.org/10.15593/perm.mech/2018.2.13

11. Adamov AA. Experimental Verification and Identification of the Models of Isotropic Body Showing Elastic Volume Compressibility of Disperse-Filled Composites Based on Polytetrafluorethylene and Ultra-High-Molecular-Weight Polyethylene. Konstruktsii iz kompozitsionnykh materialov. 2013;2:28–37.

12. Goldman AYa. Ob"emnoe deformirovanie plastmass. Leningrad: Mashinostroenie; 1984. 232 p. (In Russ.)

13. Adamov AA, Matveenko VP, Trufanov NA, et al. Metody prikladnoi vyazkouprugosti. Ekaterinburg: URO RAN; 2003. 411 p. (In Russ.)

14. Cheng L, Xia X, Yu W, et al. Flat-Punch Indentation of Viscoelastic Material. Journal of Polymer Science. Part B: Polymer Physics. 2000;38:10–22. 10.1002/(SICI)1099-0488(20000101)38:1<10::AID-POLB2>3.0.CO;2-6

15. Lu H, Wang, B, Ma J, et al. Measurement of Creep Compliance of Solid Polymers by Nanoindentation. Mechanics of Time-Dependent Materials. 2003;7:189–207. https://doi.org/10.1023/B:MTDM.0000007217.07156.9b

16. Tóth LF, P De Baets, Szebényi G. Thermal, Viscoelastic, Mechanical and Wear Behaviour of Nanoparticle Filled Polytetrafluoroethylene: A Comparison. Polymers. 2020;12:1940. https://doi.org/10.3390/polym12091940

17. Gavrilenko SL, Shilko SV. Attestatsiya lineinoi vyazkouprugoi modeli antifriktsionnogo polimernogo kompozita po rezul'tatam uskorennykh ispytanii na relaksatsiyu. Teoreticheskaya i prikladnaya mekhanika. 2017;32:155–158. (In Russ.)

18. Konova EM, Ostrer SG, Khatipov SA. Vliyanie prirody napolnitelya na fiziko-mekhanicheskie svoistva radiatsionnykh modifikatsii kompozitov na osnove politetraftorehtilena. Plasticheskie Massy. 2011;5:40–43. (In Russ.)

19. Wenjuan Xu, Hong Gao, LiLan Gao, et al. Tensile Ratcheting Behaviors of Bronze Powder Filled Polytetrafluoroethylene. Frontiers of Chemical Science and Engineering. 2013;7:103–109. https://doi.org/10.1007/s11705-013-1315-8

20. Kadashevich Yu, Pomytkin S. Endochronic Model of Plasticity Generalizing Sanders's Theory. Scientific Letters of Rzeszow University of Technology. Mechanics. 2014;31:539–547. https://doi.org/10.7862/RM.2014.57

Received 08.08.2022

Revised 29.08.2022

Accepted 06.09.2022

About the Authors:

Petukhov, Dmitriy S., lead engineer of the Laboratory of Nonlinear Mechanics of Solids, Institute of Continuous Media Mechanics UrB RAS (1, Academika Koroleva St., Perm, 614018, RF), ResearcherID, ScopusID, ORCID, petuhovds@mail.ru

Adamov, Anatoliy A., leading researcher of the Laboratory of Nonlinear Mechanics of Solids, Institute of Continuous Media Mechanics UrB RAS (1, Academika Koroleva St., Perm, 614018, RF), Dr.Sci. (Phys.-Math.), ScopusID, ORCID, adamov@icmm.ru

Keller, Ilya E., head of the Laboratory of Nonlinear Mechanics of Solids, Institute of Continuous Media Mechanics UrB RAS (1, Academika Koroleva St., Perm, 614018, RF), Dr.Sci. (Phys.-Math.), ResearcherID, ScopusID, ORCID, kie@icmm.ru

Claimed contributorship:

D. S. Petukhov: modification of models and identification of their material constants according to experimental data. A. A. Adamov: development of methodology and conducting experiments. I. E. Keller: literature review and model selection.

Conflict of interest statement

The authors do not have any conflict of interest.

All authors have read and approved the final manuscript.

MECHANICS

UDC 629.7.017.1
https://doi.org/10.23947/2687-1653-2022-22-3-193-203

Original article

Methodology for Determining the Probability of Damage to Unmanned Aerial Vehicles as a Result of Exposure to Atmospheric Environmental Factors

Dmitriy G. Belonozhko[1] ✉, **Igor D. Korolev**[1], **Yury O. Chernyshev**[2], **Nikolay N. Ventsov**[2]

[1] Krasnodar Higher Military School named after army general S. M. Shtemenko, 4, ul. Krasina, Krasnodar, Russian Federation

[2] Don State Technical University, 1, Gagarin sq., Rostov-on-Don, Russian Federation

✉ staeer@rambler.ru

Abstract

Introduction. For the effective use of unmanned aerial vehicles (UAV), it is required to take into account the impact of atmospheric environmental factors. Based on the existing level of development of the research and methodological apparatus, it is impossible to determine the probability of damage to the UAV under the conditions of complex exposure to atmospheric environmental factors and to assess the feasibility of further performance of the flight task. Violation of the UAV operation process is caused by the influence of atmospheric precipitation, wind and temperature conditions of the environment. The work aims at the development of a methodology for determining the probability of damage to UAV as a result of exposure to atmospheric environmental factors, as well as to evaluate the performance of the software package implementing the developed algorithm using triangular, trapezoidal, pentagonal, and Gaussian membership functions.

Materials and Methods. A technique is proposed that makes it possible, using the theory of fuzzy logic, to determine the probability of damage to the UAV with inaccuracies and uncertainties in the description of atmospheric effects of the environment. It takes into account possible atmospheric forcing and enables to determine the probability of damage to the UAV under various atmospheric influences. The computational complexity of the algorithm implementing the technique depends significantly on the number of qualitative assessments of atmospheric impacts on UAV.

Results. A method for determining the probability of damage to UAV as a result of exposure to atmospheric environmental factors based on fuzzy sets (triangular, trapezoidal, pentagonal, Gaussian) was proposed and tested. The use of fuzzy sets for estimating the conditions of the UAV application environment was described. An algorithm was developed to determine the probability of damage to the UAV as a result of exposure to atmospheric environmental factors. A computational experiment was carried out to determine the complexity of calculating the probability of UAV damage as a result of atmospheric forcing under various environmental conditions: “moderate conditions” at a wind speed of 3 m/s, precipitation intensity of 0.8 mm/h, and air temperature of 5 °C; “very heavy conditions” of the external environment at a wind speed of 12 m/s, precipitation intensity 3.5 mm/h, and air temperature of –6 ºC. It was established that the use of triangular membership functions to calculate the probability of damage to the UAV as a result of atmospheric forcing provided higher performance compared to the rest ones (trapezoidal, pentagonal, Gaussian).

Discussion and Conclusions. The values of the UAV damage probabilities obtained during the implementation of the methodology under atmospheric environmental influences can be used at the pre-flight preparation stage and during the flight to assess the feasibility of further performance of the flight task. Based on the analysis of the application of the

considered forms of membership functions, recommendations for their application are given. The use of algorithms with triangular membership functions will provide high performance of UAV control systems (UAV CS).

Keywords: unmanned aerial vehicle, membership function, fuzzy sets, mathematical model, control, atmospheric forcing.

Achnowledgments. The co-authors express their sincere gratitude to Yuri Olegovich Chernyshev for his mentoring, valuable advice, criticism, and lively participation in this work.

For citation. D. G. Belonozhko, I. D. Korolev, Yu. O. Chernyshev, N. N. Ventsov. Methodology for Determining the Probability of Damage to Unmanned Aerial Vehicles as a Result of Exposure to Atmospheric Environmental Factors. Advanced Engineering Research, 2022, vol. 22, no. 3, pp. 193–203. https://doi.org/10.23947/2687-1653-2022-22-3-193-203

Introduction. The analysis of the experience in using UAV has shown that it is critical to increase the effectiveness of UAV under the conditions of environmental influences [1–4]. The equipment of modern unmanned aerial vehicles makes it possible to measure and assess the condition of technical systems, flight parameters, and the external environment [2].

With the rapid updating of current flight information and its large volume, the implementation of management faces the problem of providing the stable functioning of the UAV under the influence of the external environment. It is worth noting that human abilities are limited, and in a rapidly changing environment, a number of parameters of the UAV and the external environment, such as temperature and engine speed, wind speed and precipitation intensity, due to limited human capabilities, may not be taken into account or overlooked. Such control inaccuracies can cause the failure of the UAV equipment or its damage [3]. The influence of environmental factors on the UAV can significantly reduce the quality of the task, and for certain values of the parameters of external influences, completely exclude the possibility of using the UAV [4].

In this regard, solving problems related to maintaining the effective functioning of UAV under various atmospheric conditions is an important step in drawing up requirements for on-board UAV equipment that ensures flight safety in emergency situations arising under the influence of various weather phenomena [4].

Materials and Methods. The authors see a solution to the problem in automating the process of assessing the parameters of the external environment to determine the probability of damage to the UAV and in developing control corresponding to the current situation. In papers [1–5], meteorological conditions, specifically, precipitation, wind loads, temperature, air pressure and humidity, are considered as destabilizing effects of the external environment. To describe the atmospheric effects of the external environment[1], a probabilistic model is used in combination with the theory of random processes. A method is also known for estimating the intensity of precipitation and the water content of clouds based on remote measurement data[2]. The authors also note that the natural variability and stochastic nature of atmospheric conditions do not enable to establish strict mathematical dependences for describing atmospheric conditions of the environment.

With the uncertainty of parameters and incomplete information about the state of the external environment, it is not always possible to present its unintended impact in the form of clear values. This problem can be solved using fuzzy set theory. In the case of its application, there is no need to know the exact mathematical model of atmospheric effects of the external environment to assess its impact on the UAV[3]. Assessment of the operating conditions of complex systems is one of the areas where fuzzy sets are widely used to eliminate the inaccurate nature of environmental influences [6].

[1] Kuznetcov IE, KuznetcovAA, Baklanov IO, et al. The Stochastic Model of Search and Detection of Ground Objects Using Unmanned Aerial Vehicles under Conditions of Irregular Influence of the Environment. In: Proc. VI Int. Conf. and Youth School “Information Technologies and Nanotechnologies (ITNT-2020)”. In 4 vol. VA Sobolev, ed. Samara: Samara National Research University; 2020. P. 152–156.

[2] Kuznetsov DV, Bulgin DV. Metodika otsenki intensivnosti osadkov i vodnosti oblakov na osnove dannykh distantsionnykh izmerenii. In: Proc. XXI Int. Research-Methods.Conf. “Informatics: Problems, Methods, Technologies”, 11-12 Feb., 2021. Voronezh: Obshchestvo s ogranichennoi otvetstvennost'yu “Vehlborn”; 2021. P. 420–426. (In Russ.).

[3] Cherepanov IE, Kuznetsov DV. Model' prognozirovaniya stepeni slozhnosti meteouslovii s uchetom teorii nechetkoi logiki. In: Proc. XXI Int. Research-Methods.Conf. “Informatics: Problems, Methods, Technologies”, 11-12 Feb., 2021. Voronezh: Obshchestvo s ogranichennoi otvetstvennost'yu “Vehlborn”; 2021. P. 659–663. (In Russ.)

Thus, the analysis of well-known research in this area[3]. shows that in automated forecasting and decision support systems under conditions of lack and uncertainty of the initial information for its processing, fuzzy logic methods have proven themselves well.

Research Results

Development of methodology for determining the probability of damage to UAV as a result of exposure to atmospheric environmental factors

In [6], a feature is noted that distinguishes the intelligent automatic control system from the one built according to the "customary" scheme. It is associated with the use of knowledge processing mechanisms to perform the required functions under uncertain (or incompletely specified) conditions with the random nature of external disturbances. Intellectualization of the UAV operation process to account for uncertainty factors can be achieved through the use of a knowledge base and an inference engine [6].

To determine the value of the probability of damage to UAV as a result of environmental factors, it is required:

1. To formulate fuzzy estimates of atmospheric effects:

– wind speed;

– precipitation intensity;

– temperature conditions of the environment;

2. To develop a fuzzy model for calculating the probability of UAV damage as a result of atmospheric environmental impacts.

3. To create a base of rules for fuzzy inference of the influence of atmospheric effects on UAV;

4. To implement fuzzy inference.

5. To defuzzify the fuzzy value of the probability of damage to UAV as a result of atmospheric influences of the environment P_{AB}.

The functional diagram of the technique is shown in Figure 1.

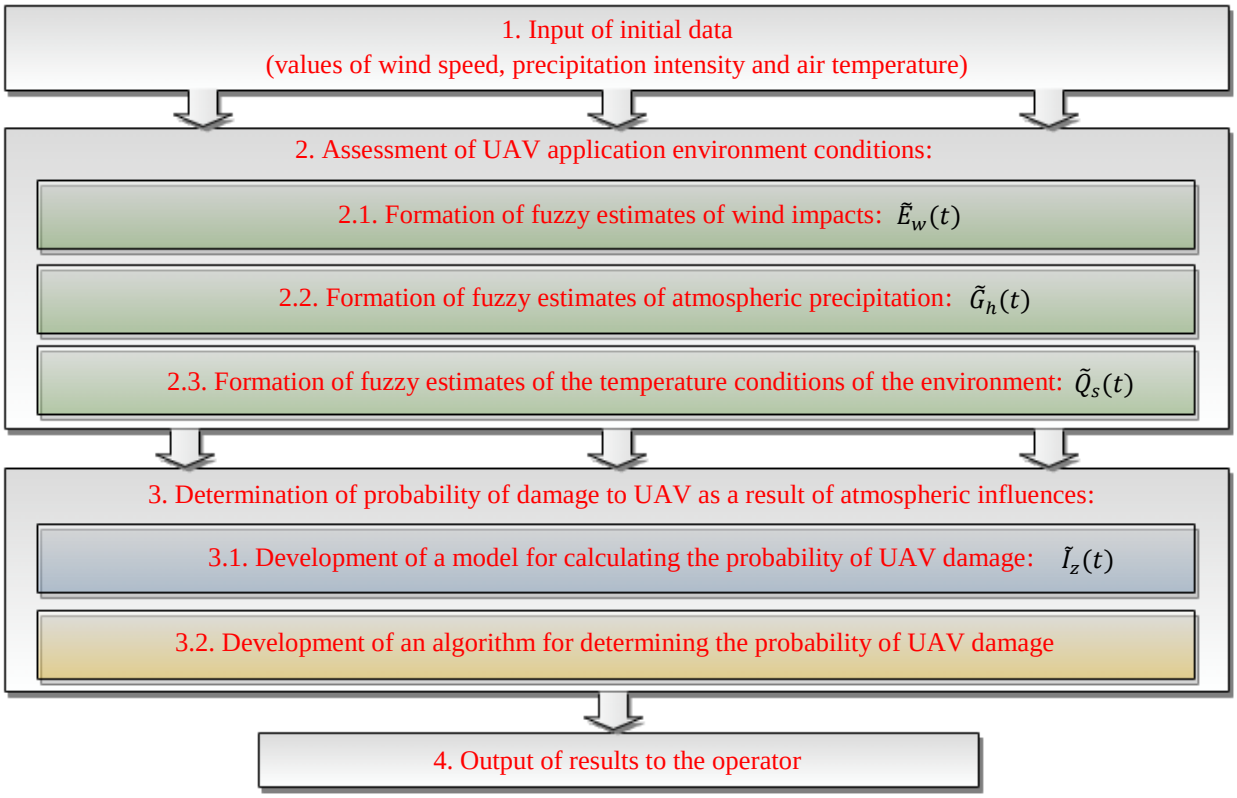

Fig. 1. Functional diagram of the methodology for determining the probability of damage to UAV as a result of exposure to atmospheric environmental factors

[3]Ibid.

It is required to determine the probability of damage to UAV based on the analysis of the input fuzzy situation. Let us consider in detail the stages of the proposed methodology.

Assessment of UAV application environment conditions

Atmospheric environmental factors (wind, precipitation, and air temperature) may change during the flight. The dynamic change of the environment parameters has a significant impact on the stability of the UAV operation [7]. A short-range UAV made according to the aerodynamic scheme of an airplane type with flight speeds in the range from 20 to 60 m/s is considered as a typical one. Icing of the surfaces of such UAV can cause a change in its mass, as well as aerodynamic characteristics. The wind speed can vary depending on altitude and flight time. It has a significant impact on the UAV of the class under consideration [8]. For this reason, it is reasonable to assess atmospheric impacts on the basis of dynamic fuzzy approaches. The initial data for the functional model are the environmental conditions: wind speed e, precipitation intensity g, and air temperature t.

To estimate the effect of the wind acting on the UAV at time *t*, we introduce a set of triangular fuzzy numbers:

$$E(t) = \left\{\tilde{E}_1(t), \tilde{E}_2(t), \dots, \tilde{E}_w(t), \dots, \tilde{E}_{N_{E(t)}}(t)\right\}, \quad (1)$$

where $E(t)$ — a set of triangular fuzzy numbers describing the correspondence of the current wind speed e to fuzzy estimates of wind effects on UAV at time *t*; $\tilde{E}_w(t)$ — a triangular fuzzy number describing the correspondence of the current wind speed e to a fuzzy estimate of wind impacts on UAV at time *t*; $w = \overline{1, N_{E(t)}}$.

In accordance with the concept of a fuzzy set, triangular fuzzy number $\tilde{E}_w(t)$ can be understood as [9, 10]:

$$\tilde{E}_w(t) = \left\{\left(e, \mu_{\tilde{E}_w(t)}(e)\right)\right\}, \quad (2)$$

where $\mu_{\tilde{E}_w(t)}(e)$ — membership function of the wind speed e to the assessment of the wind influence $\tilde{E}_w(t)$ on the UAV.

Within the framework of the developed model, the qualitative assessment of the wind effect on the UAV depends only on its speed, i.e., possible inhomogeneities of the wind flow and its direction are not taken into account.

The membership function of triangular fuzzy number $\mu_{\tilde{E}_w(t)}(e)$ can be represented by a tuple of three elements:

$$\mu_{\tilde{E}_w(t)}(e) = \langle l_{\tilde{E}_w}(t); c_{\tilde{E}_w}(t), r_{\tilde{E}_w}(t)\rangle, \quad (3)$$

where $c_{\tilde{E}_w}(t)$ — clear value of wind speed that most accurately corresponds to the qualitative assessment $\tilde{E}_w(t)$ of the wind influence on the UAV at time *t*; $l_{\tilde{E}_w}(t)$ and $r_{\tilde{E}_w}(t)$ — clear values of wind speed in the least nonzero degree corresponding to the qualitative assessment $\tilde{E}_w(t)$ of the wind influence on the UAV at time *t*. Values $l_{\tilde{E}_w}(t)$ and $r_{\tilde{E}_w}(t)$ determine the fuzziness of estimate $\tilde{E}_w(t)$. If $l_{\tilde{E}_w}(t) = r_{\tilde{E}_w}(t) = c_{\tilde{E}_w}(t)$, then the estimate becomes clear.

Specifically, $\tilde{E}_1(t)$ may mean an insignificant assessment of the wind impact on the UAV. If experts decide that the maximum wind speed at which its impact on the UAV under the current flight conditions at time *t* can be interpreted as insignificant 0.8 m/s, then the fuzzy number membership function will take the form $\mu_{\tilde{E}_1(t)}(e) = (0; 0; 0.8)$. Since the first and second elements of the tuple are equal to zero, the region of nonzero membership is located on a closed interval [0, 0.8]. To determine the degree of membership $\mu_{\tilde{E}_1(t)}(e)$ of the wind effect at a speed of e to the fuzzy assessment of the impact $\tilde{E}_1(t)$, it is required to substitute e into the equation of a straight line passing through the points (0;1) and (0.8;0).

During the flight, UAV can determine the actual wind speed offline. Based on the values of tuples of three elements set by experts, by analogy with the above example, we formulate possible estimates of the influence of wind on the UAV. For this, the values of the triangular membership functions of the fuzzy sets $\tilde{E}_w(t)$ from the values of the wind speed e are represented by graphs (Fig. 2):

– $\tilde{E}_1(t)$ — "insignificant influence", $\mu_{\tilde{E}_1(t)}(e) = (0; 0; 0.8)$;

– $\tilde{E}_2(t)$ — "very weak influence", $\mu_{\tilde{E}_2(t)}(e) = (0; 1; 3)$;

– $\tilde{E}_3(t)$ — "weak influence", $\mu_{\tilde{E}_3(t)}(e) = (0.2; 2.5; 4.8)$;

– $\tilde{E}_4(t)$ — "strong influence", $\mu_{\tilde{E}_4(t)}(e) = (1.5; 4.2; 6.9)$;

– $\tilde{E}_5(t)$ — "very strong influence", $\mu_{\tilde{E}_5(t)}(e) = (1.5; 7; 12.5)$;

– $\tilde{E}_6(t)$ — "dangerous influence", $\mu_{\tilde{E}_6(t)}(e) = (5; 11; 18)$;

– $\tilde{E}_7(t)$ — "very dangerous influence", $\mu_{\tilde{E}_7(t)}(e) = (10; 15; \infty)$.

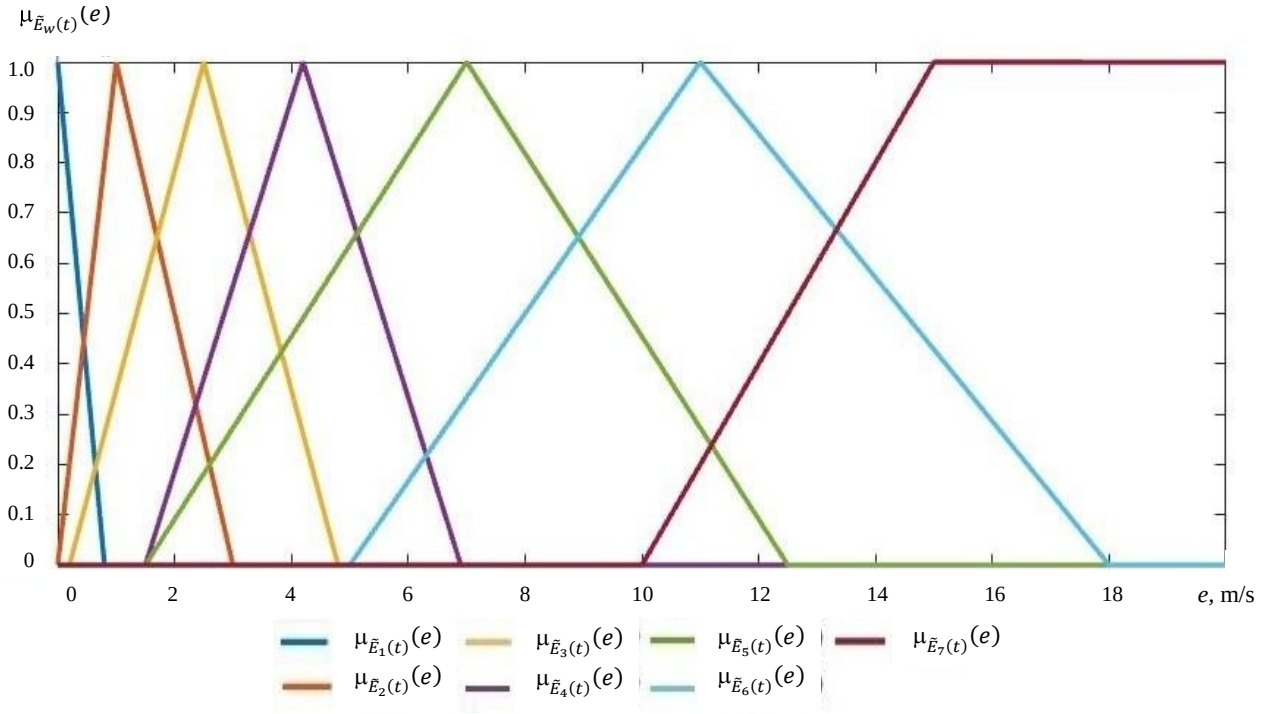

Fig. 2. Graphs of dependences of triangular membership functions of fuzzy sets $\tilde{E}_w(t)$ on the values of wind speed *e*

By analogy with the assessment of the influence of wind, we consider estimates of the influence of precipitation and temperature affecting the UAV at time *t*.

To assess the influence of precipitation, we introduce a set of triangular fuzzy numbers:

$$G(t) = \left\{\tilde{G}_1(t), \tilde{G}_2(t), \dots, \tilde{G}_h(t), \dots, \tilde{G}_{N_{G(t)}}(t)\right\}, \quad (4)$$

where $G(t)$ — a set of triangular fuzzy numbers describing the correspondence of the current precipitation intensity g to fuzzy estimates of the effects of precipitation on UAVs at time *t*; $\tilde{G}_h(t)$ — triangular fuzzy number describing the correspondence of the current precipitation intensity g to a fuzzy estimate of the effects of precipitation on UAV at time *t*; $h = \overline{1, N_{G(t)}}$.

To assess the effect of temperature, we introduce a set of triangular fuzzy numbers:

$$Q(t) = \left\{\tilde{Q}_1(t), \tilde{Q}_2(t), \dots, \tilde{Q}_s(t), \dots, \tilde{Q}_{N_{Q(t)}}(t)\right\}, \quad (5)$$

where $Q(t)$ — a set of triangular fuzzy numbers describing the correspondence of the current temperature q to fuzzy estimates of the effects of temperature on the UAV at time *t;* $\tilde{Q}_s(t)$ — triangular fuzzy number describing the

correspondence of the current temperature q to a fuzzy estimate of the temperature effects on the UAV at time t; $s = \overline{1, N_{Q(t)}}$.

In the developed model, the influence of weather conditions is estimated based on three sets (t), $G(t)$, and $Q(t)$. The elements of these sets correspond to triangular membership functions, which simplifies the adaptation of the model. To adjust the membership function, it is only required to change the values of atmospheric exposure that correspond to the greatest and/or least extent to the adaptable fuzzy estimate.

Algorithm for determining the probability of UAV damage as a result of exposure to atmospheric environmental factors

To implement the methodology, an algorithm has been developed to determine the probability of damage to UAV as a result of exposure to atmospheric environmental factors. The algorithm enables, under conditions of uncertainty, to take into account the influence of atmospheric environmental factors to calculate the probability of damage to UAV according to the current situation. The initial data for the algorithm are fuzzy sets $\tilde{E}_w(t)$, $\tilde{G}_h(t)$ and $\tilde{Q}_s(t)$.

Figure 3 shows its block diagram.

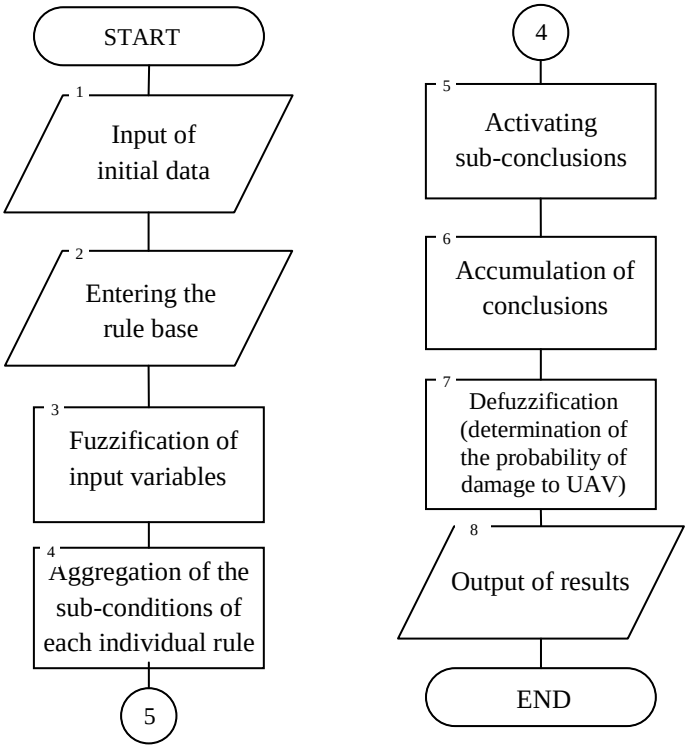

Fig. 3. Block diagram of the algorithm for determining the probability of damage to UAV as a result of exposure to atmospheric environmental factors

Determination of the probability of UAV damage as a result of atmospheric environmental influences

Papers [4, 5] note the natural variability and stochastic nature of atmospheric conditions. Due to the fact that the atmospheric effects of the external environment are dynamic, it is reasonable to take this circumstance into account when constructing a model for determining the probability of damage (equipment failure) of UAV. We introduce a set of triangular fuzzy numbers:

$$I(t) = \left\{\tilde{I}_1(t), \tilde{I}_2(t), \dots, \tilde{I}_z(t), \dots, \tilde{I}_{N_{I(t)}}(t)\right\}, \quad (6)$$

where $I(t)$ — a set of triangular fuzzy numbers describing the correspondence of the current value of the probability of damage to UAV P_{AB} at time t; $\tilde{I}_z(t)$ — triangular fuzzy number describing the correspondence of the current value of

the probability of damage to the UAV P_{AB} to a fuzzy assessment of the level of exposure to atmospheric environmental factors on UAV at time *t;* $z = \overline{1, N_{I(t)}}$.

With regard to the UAV performance levels [11] (operable, limited operable, and inoperable condition), consider the following UAV damage probabilities: $\tilde{I}_1(t)$ — "low" (approximately 0.2), $\tilde{I}_2(t)$ — "medium" (approximately 0.5) and $\tilde{I}_3(t)$ — "high" (approximately 0.8). Triangular fuzzy number $\tilde{I}_z(t)$ is represented as [9, 10]:

$$\tilde{I}_z(t) = \left\{\left(P_{\text{AB}}, \mu_{\tilde{I}_z(t)}(P_{\text{AB}})\right)\right\}, z = \overline{1,3}, \tag{7}$$

where $\mu_{\tilde{I}_z(t)}(P_{\text{AB}})$ — the membership function of the probability of damage to UAV P_{AB} to the assessment of impact $\tilde{I}_z(t)$ of the wind on the UAV.

Given that the model under consideration has a dynamic character, the compilation of the fuzzy inference rule base should be preceded by a study of the influence of atmospheric conditions on the probability of damage to UAV. To that end, a series of experiments were conducted under various environmental conditions. Based on expert assessments of statistical data, a database of fuzzy inference rules was formed [10]. The rules for determining qualitative estimates of the probability of damage to UAV as a result of atmospheric influences of the external environment were formalized using fuzzy sets as follows:

$$\text{If } q \text{ is } \tilde{Q}_s(t) \text{ and } e \text{ is } \tilde{E}_w(t) \text{ and } g \text{ is } \tilde{G}_h(t) \text{ then is } \tilde{I}_z(t). \tag{8}$$

That is, under simultaneous conditions of minimally sufficient membership:

– of temperature *q* to the fuzzy assessment of the impact of temperature $\tilde{Q}_s(t)$;

– of wind speed *e* to the fuzzy assessment of the wind impact $\tilde{E}_w(t)$;

– of precipitation intensity *g* to the fuzzy assessment of the impact of precipitation $\tilde{G}_h(t)$, the fuzzy assessment of probability $\tilde{I}_z(t)$ becomes relevant.

To obtain clear value $P^*_{\text{AB}}(t)$ of the probability of damage to UAV as a result of atmospheric influences of the external environment at time *t*, it is required to defuzzify the corresponding fuzzy result according to formula [10]:

$$P^*_{\text{AB}}(t) = \frac{\int_0^1 \tilde{P}_{\text{AB}} \cdot \mu^{\text{рез}}_{\tilde{I}_z(t)}(\tilde{P}_{\text{AB}}) d\tilde{P}_{\text{AB}}}{\int_0^1 \mu^{\text{рез}}_{\tilde{I}_z(t)}(\tilde{P}_{\text{AB}}) d\tilde{P}_{\text{AB}}}, \tag{9}$$

where $\mu^{\text{рез}}_{\tilde{I}_z(t)}(\tilde{P}_{\text{AB}})$ — the resulting membership function of fuzzy set $\tilde{I}_z$, representing the general conclusion (conclusion) from all the rules (8); $\tilde{P}_{\text{AB}}$ — the output variable of the fuzzy inference, characterizing the fuzzy value of the probability of damage to the UAV as a result of atmospheric environmental influences.

Thus, the intellectualization of the functioning process is achieved through the use of a knowledge base and an inference engine, and provides that uncertainties are taken into account [6].

Scheme of the UAV operation process under environmental conditions

To calculate the probability of damage to UAV as a result of atmospheric environmental influences, it is required to implement fuzzy inference. It consists in the sequential execution of aggregation, activation and accumulation operations [10]. The scheme of the UAV operation process under environmental conditions is shown in Figure 4.

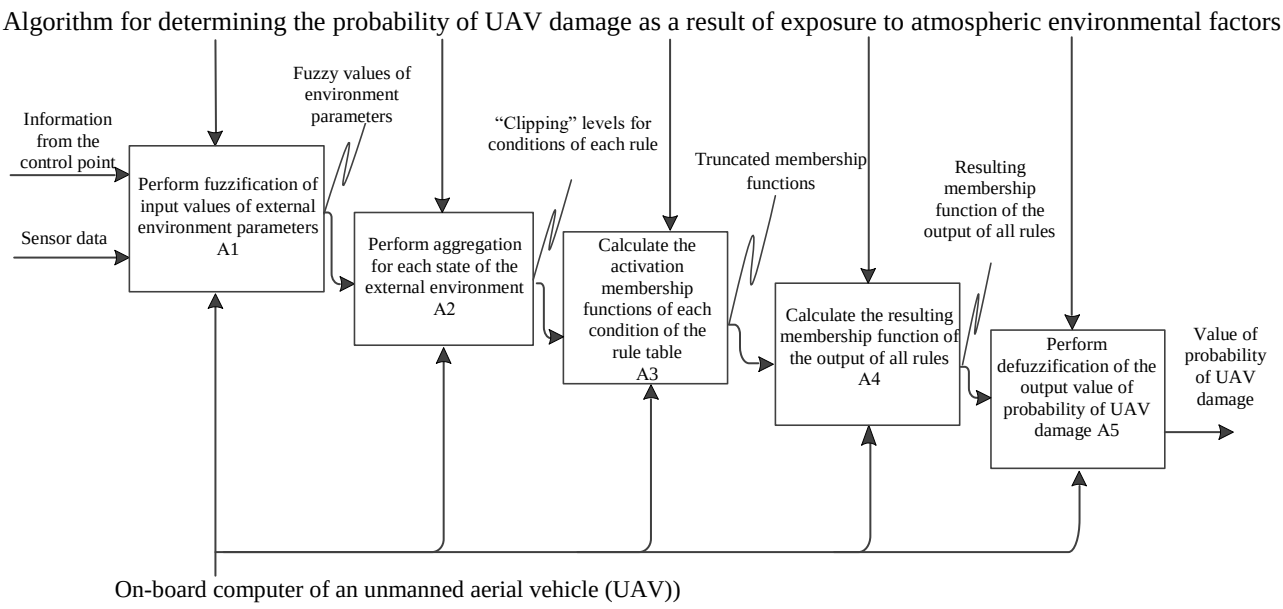

Fig. 4. Scheme of the UAV operation process under the influence of atmospheric environmental factors

Computational experiment

In [12], an analysis of foreign periodical literature in recent years has been carried out to identify formal approaches to dealing with uncertainties. The conclusion was made about the expediency of using *n*-angle numbers to determine the accuracy of the uncertainty formalization. Thus, when using the triangular representation of fuzzy numbers [10], each initial fuzzy number is described by three scalar values, which greatly simplifies the computational process.

In many cases, triangular and trapezoidal representations of fuzzy numbers are insufficient. If it is required to consider more complex influence of uncertainties, specifically, due to the greater exposure of the equipment installed on UAV to precipitation, it is reasonable to use more complex forms of membership functions [12, 13]. Therefore, in [13], pentagonal fuzzy numbers, which reflect uncertainties much more accurately, were studied as an alternative.

Let us consider the basic, most used membership functions for the representation of fuzzy linguistic terms: Gaussian, triangular, trapezoidal [10], and pentagonal fuzzy numbers [13, 14].

Based on the analysis of papers [13, 14], we present the pentagonal membership function of elements to fuzzy sets of wind load effects $\tilde{E}_w(t)$ in the form of a tuple:

$$\mu_{\tilde{E}_w(t)}(e) = \langle l_{\tilde{E}_w}(t); k_{\tilde{E}_w}(t); c_{\tilde{E}_w}(t); p_{\tilde{E}_w}(t); r_{\tilde{E}_w}(t), \alpha \rangle, \quad (10)$$

where $c_{\tilde{E}_w}(t)$ — clear value of the wind speed most accurately corresponding to the qualitative assessment $\tilde{E}_w(t)$ of the wind impact on UAV at time *t*; $l_{\tilde{E}_w}(t)$ and $r_{\tilde{E}_w}(t)$ — clear values of wind speed in the smallest (nonzero) degree corresponding to qualitative assessment $\tilde{E}_w(t)$ of the wind impact on UAV at time *t*; $k_{\tilde{E}_w}(t)$ and $p_{\tilde{E}_w}(t)$ — clear wind speed values with α degree (nonzero), corresponding to qualitative assessment $\tilde{E}_w(t)$ of the wind impact on UAV at time *t*. Values $k_{\tilde{E}_w}(t)$ and $p_{\tilde{E}_w}(t)$ determine the fuzziness of assessment $\tilde{E}_w(t)$. In case, if $l_{\tilde{E}_w}(t) = r_{\tilde{E}_w}(t) = k_{\tilde{E}_w}(t) = p_{\tilde{E}_w}(t)$, we get a triangular fuzzy number. By changing the values of α level, we obtain a different form of the pentagonal membership function (Fig. 5).

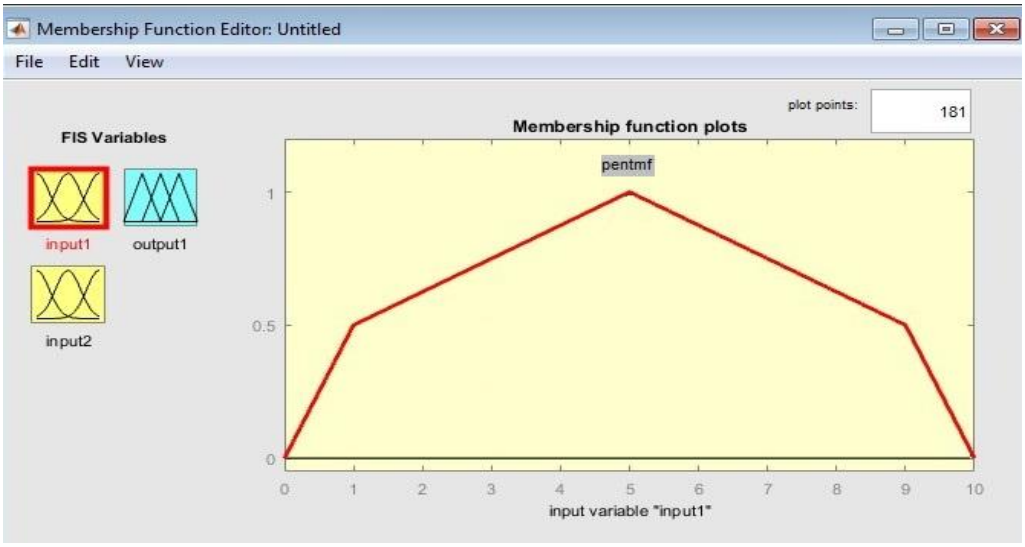

Fig. 5. Pentagonal membership function in *MATLAB* software environment

To study the pentagonal membership function in a software environment, it is required to describe it in the form of a program code. When implementing the algorithms[4,5], a custom pentagonal membership function was developed in the *Fuzzy Logic Toolbox* application package of the *MATLAB* software environment. This tool provides exploring mathematical models and algorithms based on the application of fuzzy logic theory.

To assess the accuracy of uncertainty when working with the described membership functions, it is required to conduct a computational experiment. It is reasonable to carry out the comparison on the same set of source data. The values of the probability of UAV damage as a result of atmospheric influences are calculated under "moderate conditions" (actual values: wind speed 3 m/s, precipitation intensity 0.8 mm/h, air temperature 5 °C) and "very difficult conditions" (actual values: wind speed 12 m/s, precipitation intensity 3.5 mm/h, air temperature – 6 °C) of the external environment.

Using *MATLAB* tools, the performance of the software package implementing the developed algorithm[4] was evaluated depending on the form of the membership function used. An *IBM*-compatible PC with minimal system requirements (P4 – 2.500 MHz, 2.048 Mb RAM, *Windows* operating system) was used to conduct the computational experiment. Triangular, trapezoidal, pentagonal and Gaussian membership functions were evaluated. The results are presented in Table 1.

Table 1

Average operating time of the software package

Type of membership function used	Time, s	
	"Moderate conditions": wind speed 3 m/s, precipitation intensity 0.8 mm/h, air temperature 5 °C	"Very difficult conditions": wind speed 12 m/s, precipitation intensity 3.5 mm/h, air temperature – 6 °C
Triangular	0.028	0.028
Trapezoidal	0.031	0.03
Pentagonal	0.034	0.035
Gaussian	0.031	0.03

From Table 1, it can be concluded that a computer program based on the use of triangular membership functions has a higher speed in comparison to the others.

A promising area of research is studying the influence of the form of the membership function on the accuracy of calculations of the probability of damage to UAV under the uncertainty of the impact of atmospheric factors of the environment on the functioning of UAV.

[4] Belonozhko DG, Korolev ID, Chernyshev Yu.O. Certificate of State Registration of Computer Program No. 2022613419, Russian Federation. Software Package for Evaluating the Accuracy of Uncertainty and Performance of Fuzzy Algorithms for Controlling an Unmanned Aerial Vehicle, no. 2022613002; 2022. (In Russ.)

[5] Belonozhko DG, Korolev ID, Chernyshev Yu.O. Certificate of State Registration of Computer Program No. 2022613691, Russian Federation. Software Package for Intelligent Control of an Unmanned Aerial Vehicle under Conditions of Destructive Impacts Based on Pentagonal Accessory Functions, no. 2022613009; 2022. (In Russ.)

Discussion and Conclusions. A method has been developed for determining the probability of damage to UAV as a result of exposure to atmospheric environmental factors, based on the mathematical apparatus of fuzzy sets. Fuzzy qualitative estimates made it possible to significantly expand traditional mathematical modeling techniques that require accurate information about input quantities. The use of this technique provided assessing the probability of UAV damage when the outcomes of alternatives were not known accurately and the probabilities of their occurrence were estimated using membership functions. The obtained values of the probabilities of UAV damage as a result of atmospheric influences of the external environment can be used at the stage of pre-flight preparation and during the flight to assess the feasibility of further performance of the flight task.

With the help of a software package implementing this technique, the values of the probability of damage to UAV under "moderate conditions" and "very difficult conditions" of the external environment were obtained. According to the results of the analysis of the application of these forms of membership functions and the computational experiment, the high performance of the software package using the triangular method of formalization of fuzzy sets was validated. A significant advantage of triangular membership functions is that their definition requires the least amount of information compared to other functions.

Thus, it is reasonable to apply algorithms using triangular membership functions in the onboard computers of the UAV CS to assess the atmospheric parameters of the environment. This will provide high performance of the UAV CS under conditions of using computers with low performance.

References

1. Ziquan Yu, Youmin Zhang, Bin Jiang, et al. Fractional Order PID-Based Adaptive Fault-Tolerant Cooperative Control of Networked Unmanned Aerial Vehicles against Actuator Faults and Wind Effects with Hardware-in-the-Loop Experimental Validation. Control Engineering Practice. 2021;114:104861. http://dx.doi.org/10.1016/j.conengprac.2021.104861

2. Veselov GE, Ingabire Alin Ingabire Alin. Synergetic Synthesis of control law for UAV in the presence of wind disturbances with input constraints. Izvestiya SFedU. Engineering Sciences. 2020;2:101–112. https://doi.org/10.18522/2311-3103-2020-2-101-112

3. Lei Cui, Ruizhi Zhang, Hongjiu Yang, et al. Adaptive Super-Twisting Trajectory Tracking Control for an Unmanned Aerial Vehicle under Gust Winds. Aerospace Science and Technology. 2021;115:106833. http://dx.doi.org/10.1016/j.ast.2021.106833

4. Kuznetsov IE, Melnikov AV, Rogozin EA, et al. Methodology for accounting the influence of meteorological factors on the efficiency of application of unmanned aerial vehicles on the basis of system analysis. Herald of Dagestan State Technical University. Technical Sciences. 2018;45:125–139. https://doi.org/10.21822/2073-6185-2018-45-2-125-139

5. Kuznetsov IE, Strashko OV, Dorofeev VV, et al. The Mathematical Model of Characteristics of the Convective Unstable Atmosphere Taking into Account Microphysical Processes in Clouds. Journal of Physics: Conference Series. 2018. P. 012170. https://doi.org/10.1088/1742-6596/1096/1/012170

6. Lokhin VM, Manko SV, Romanov MP. The improving of the adaptive properties of autonomous robots based on intelligent technologies. Extreme Robotics. 2015;1:59–67.

7. Belonozhko DG. An Algorithm for Ensuring the Required Level of Stability of Control of an Unmanned Aerial Vehicle in the Conditions of Counteraction. Software & Systems. 2022;35:197–206.

8. San'ko AA, Rozhkov IV, Shejnikov AA. Wind Influence on the Angular Stabilization System of the Unmanned Aerial Vehicle. Crede Experto: Transport, Society, Education, Language. 2019;1:41–51.

9. Zadeh LA. Fuzzy sets. Information and Control. 1965;8:338–353. https://doi.org/10.1016/S0019-9958(65)90241-X

10. Piegat A. Fuzzy Modeling and Control. Springer; 2001. 728 p. https://doi.org/10.1007/978-3-7908-1824-6

11. Selivanov VV, Ilyin YuD. The Effect of Survivability on the Combat and Military-Economic Efficiency of Military Technical Systems. Military Thought. 2021;9:99–112. URL: https://cyberleninka.ru/article/n/vliyanie-zhivuchesti-na-boevuyu-i-voenno-ekonomicheskuyu-effektivnost-voenno-tehnicheskih-sistem (accessed: 15.07.2022).

12. Chernyshev YuO, Trebukhin AV, Panasenko PA, et al. Existing Ways to Formalize Fuzzies in Transport Processes. Engineering Journal of Don. 2021;7:57–79.

13. Pathinathan T, Ponnivalavan K. Reverse Order Triangular, Trapezoidal and Pentagonal Fuzzy Numbers. Annals of Pure and Applied Mathematics. 2015;9:107–117.

14. Avishek Chakraborty, Sankar Prasad Mondal, Shariful Alam, et al. The Pentagonal Fuzzy Number: Its Different Representations, Properties, Ranking, Defuzzification and Application in Game Problems . Symmetry. 2019;11:1–31. http://dx.doi.org/10.3390/sym11020248

Received 08.07.2022
Revised 23.07.2022
Accepted 08.08.2022

About the Authors:

Belonozhko, Dmitriy G., deputy head of the Department, Head of the Research Laboratory, Krasnodar Higher Military School named after army general S. M. Shtemenko (18, ul. Griboedova, Krasnodar, 350009, RF), ORCID, staeer@rambler.ru

Korolev, Igor D., professor of the Department of Information Protection by Special Methods and Means, Krasnodar Higher Military School named after army general S. M. Shtemenko (18, ul. Griboedova, Krasnodar, 350009, RF), Dr.Sci. (Eng.), professor, ORCID, pi_korolev@mail.ru

Chernyshev, Yury O., professor of the Automation of Industrial Processes Department, Don State Technical University (1, Gagarin sq., Rostov-on-Don, 344003, RF), Dr.Sci. (Eng.), professor, ORCID, myvnn@list.ru

Ventsov, Nikolay N., associate professor of the Information Technologies Department, Don State Technical University (1, Gagarin sq., Rostov-on-Don, 344003, RF), Cand.Sci. (Eng.), ORCID, vencov@list.ru

Claimed contributorship:

D. G. Belonozhko: analysis of literary sources; problem statement; conducting of research; development of a mathematical model and algorithm; calculations and description of the results obtained. I. D. Korolev: academic advising; research concept formulation; formulation of conclusions. Yu. O. Chernyshev: formation of the structure of the article; description of the results; critical analysis; text editing. N. N. Ventsov: analysis of literary sources; participation in research; text editing.

Conflict of interest statement

The authors do not have any conflict of interest.

All authors have read and approved the final manuscript.

MECHANICS

UDC 531.132.1
https://doi.org/10.23947/2687-1653-2022-22-3-204-213

Original article

Application of an Inertial Sensor Unit for Position Estimation and Motion Control of the Lower-Extremity Powered Exoskeleton

Gasan R. Saypulaev ✉, Musa R. Saypulaev, Igor V. Merkuryev, Boris I. Adamov, Roilan B. Garcia
National Research University (MPEI), 14, Krasnokazarmennaya St., Moscow, Russian Federation
✉ saypulaevgr@mail.ru

Abstract

Introduction. The problem of controlling the lower-extremity powered exoskeleton motion was investigated. To solve it, it was proposed to use a program control and feedback control. The formation of control in the form of feedback required an assessment of the state of the exoskeleton (rotation angles, angular velocities, and accelerations of the links). The possibility of using an inertial measuring unit to estimate angular velocities and accelerations of exoskeleton links was considered. The work objective was to develop laws for the formation of the exoskeleton motion control, which could provide the stability of the program motion and use the measurements of encoders, micromechanical gyroscopes and accelerometers.

Materials and Methods. Previously performed mathematical modeling of the exoskeleton dynamics was used to form a program control. It was proposed to equip the exoskeleton with inertial sensor units. This solution made it possible to evaluate the state vector of the exoskeleton and to use these estimates in a feedback loop. A mathematical model of measurements of these sensors was described. The proposed version is suitable for control systems of three-link exoskeletons of the lower extremities and can be expanded to the case of multi-link exoskeleton designs.

Results. New laws of exoskeleton motion control based on a mathematical model of the system dynamics and using measurement information from encoders and inertial information sensors were proposed. Numerical simulation of exoskeleton motion was performed in the Wolfram Mathematica mathematical package. Its results confirmed the operability of the proposed control and the possibility of using an inertial sensor unit to assess the exoskeleton state. The numerical simulation results for the following program movements were presented: lifting the exoskeleton from a sitting position to a vertical position, and stabilization of the vertical equilibrium position.

Discussion and Conclusions. The proposed control can be applied in exoskeletons for medical purposes, e.g., in the task of verticalization of patients with dysfunctions of the musculoskeletal system. The possibility of using measurement information obtained from inertial measurements units in the problem of estimating the state of exoskeleton links was demonstrated. The use of inertial sensors will make it possible to determine the angular acceleration of the exoskeleton links, avoiding numerical differentiation of the measurement information received from the encoders. The obtained estimates of angular acceleration allow us to introduce feedback on angular accelerations into the control system, which opens up the possibility of improving transients in controlling the exoskeleton motion.

Keywords: exoskeleton, mathematical model, inertial sensors, control, state estimation.

Funding information. The research was carried out within the framework of the project "Development of a prototype of an active exoskeleton based on an electrohydropneumatic actuator that increases human physical abilities and the quality of motion control processes". It was supported by the grant from the National Research University (MPEI) for the implementation of research programs "Power Engineering", "Electronics, Radio Engineering, and IT", and "Industry 4.0 Technologies for Manufacturing and Robotics" in 2020–2022.

Acknowledgements. The authors express their gratitude to reviewers, whose critical assessment of the submitted materials and suggestions for their improvement contributed significantly to the quality of this article.

For citation. G. R. Saypulaev, M. R. Saypulaev, I. V. Merkuryev, B. I. Adamov, R. B. Garcia. Application of an Inertial Sensor Unit for Position Estimation and Motion Control of the Lower-Extremity Powered Exoskeleton. Advanced Engineering Research, 2022, vol. 22, no. 3, pp. 204–213. https://doi.org/10.23947/2687-1653-2022-22-3-204-213

Introduction. The development of devices designed to facilitate motion and increase motor efficiency (of exoskeletons) is perspectives for development robotics.

Exoskeletons are increasingly used in industry [1], military [2], medicine [3], and other fields. This specifies topicality of the research on their circuit and structural design, energy consumption optimization, motion trajectory, dynamics, control.

The present paper considers an active lower-extremity powered exoskeleton of a human with a rigid structure of the load-bearing frame. It is used for the rehabilitation of the musculoskeletal patients.

The development of such exoskeletons requires solving interrelated scientific and technical problems. They include:

– formation of a skeletal scheme;

– mathematical modeling of exoskeleton motion [4–6];

– optimization of the links motion based on a mathematical model of kinematics and dynamics[1];

– reasonable construction of the motor system [7, 8];

– reasonable construction of the motor system [9–11] and estimation [13, 14].

All of the above tasks are connected by the problem of finding control actions for program motion. Firstly, their source may be the dynamic model of the system. Secondly, they are developed in the form of a proportional integral-differential (PID) controller used to stabilize the program motion. A combination of two methods is also possible. At that, for the formation of feedback control (in particular, in the form of a PID controller), algorithms for assessing the state of a dynamic system and a set of sensors whose indicators are used in algorithms, play an important role.

To obtain information about the position of the exoskeleton links, they are equipped with an encoder or gyroscope [9–14]. Other possible options include accelerometer, magnetometer, potentiometer, sensors of torque, force, biosignals, etc.

In [13], it is proposed to use one block of inertial sensors consisting of gyroscopes and accelerometers on each link of the exoskeleton. This solution will provide estimating the angles of rotation, angular rates and accelerations. At the same time, the measurement model turns out to be nonlinear, which complicates the structure of control and monitoring systems.

The study aimed at improving the control of the exoskeleton by using two inertial blocks attached to each link of the exoskeleton. This approach enables to estimate the rotation angles, angular rates, and accelerations of the exoskeleton. With the help of the proposed arrangement of gyroscopes and accelerometers, a linear measurement model can be obtained, which will open up ways to simplify the control system and apply the theory of optimal evaluation of linear

[1] Yatsun SF, Savin SI, Yatsun AS, et al. Optimization of Time of Verticalization of the Exoskeleton by Criterion of Energy Efficiency. In: Vibratsionnye tekhnologii, mekhatronika i upravlyaemye mashiny. Pt. 2. Kursk: Izd-vo Yugo-Zap. gos. un-ta; 2016. P. 151–160. (In Russ.)

systems [15]. This, in turn, will be the basis for improving the motion control of the exoskeleton. The criterion for improving the control quality is reducing the deviations of the angular rates of the links from the program movement.

Materials and Methods. Consider the kinematic scheme of an exoskeleton with a rigid structure of the power frame with symmetrical movement of the legs in the sagittal plane (Fig. 1).

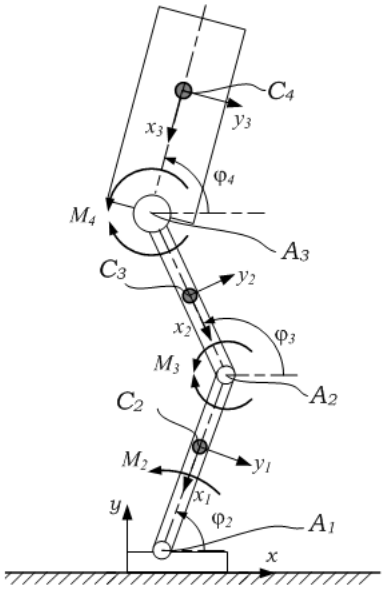

Fig. 1. Kinematic diagram of the lower-extremity powered exoskeleton in the sagittal plane

C_2, C_3, C_4 — centers of mass of the lower legs, thighs and body, respectively; A_1, A_2, A_3 — joints connecting the links of the exoskeleton; φ_2, φ_3, φ_4 — rotation angles of the exoskeleton links; M_2, M_3, M_4 — control moments created by the actuators located in the joints A_1, A_2, A_3, respectively. Coordinate system *xyz* is introduced to describe the motion. *x*-axis is directed along the reference surface, *y*-axis is directed along the local vertical to the reference surface. *z*-axis complements the coordinate axes to the right Cartesian coordinate system.

As a basis for building an exoskeleton motion control system, we use a dynamic model from [6].

$$\mathrm{A}(\mathrm{q})\ddot{\mathrm{q}} + \mathrm{F}(\mathrm{q})\dot{\mathrm{q}}^2 + \mathrm{D}\dot{\mathrm{q}} + \mathrm{P}(\mathrm{q}) = \mathrm{M}. \quad (1)$$

Here:

$$\mathrm{A}(\mathrm{q}) = \begin{pmatrix} \mathrm{J}_{22} & \mathrm{J}_{23}\cos(\varphi_2-\varphi_3) & \mathrm{J}_{24}\cos(\varphi_2-\varphi_4) \\ \mathrm{J}_{23}\cos(\varphi_2-\varphi_3) & \mathrm{J}_{33} & \mathrm{J}_{34}\cos(\varphi_3-\varphi_4) \\ \mathrm{J}_{24}\cos(\varphi_2-\varphi_4) & \mathrm{J}_{34}\cos(\varphi_3-\varphi_4) & \mathrm{J}_{44} \end{pmatrix}$$ — inertial force matrix;

$$\mathrm{F}(\mathrm{q}) = \begin{pmatrix} 0 & \mathrm{J}_{23}\sin(\varphi_2-\varphi_3) & \mathrm{J}_{24}\sin(\varphi_2-\varphi_4) \\ -\mathrm{J}_{23}\sin(\varphi_2-\varphi_3) & 0 & \mathrm{J}_{34}\sin(\varphi_3-\varphi_4) \\ -\mathrm{J}_{24}\sin(\varphi_2-\varphi_4) & -\mathrm{J}_{34}\sin(\varphi_3-\varphi_4) & 0 \end{pmatrix}$$ — speed force matrix;

$\mathrm{D} = \mathrm{diag}(\mu_2, \mu_3, \mu_4)$ — diagonal matrix of dissipative forces characterizing linear friction in joints;

$\mathrm{P}(\mathrm{q}) = \begin{pmatrix} \mathrm{M}_{G2}\cos\varphi_2 & \mathrm{M}_{G3}\cos\varphi_3 & \mathrm{M}_{G4}\cos\varphi_4 \end{pmatrix}^{\mathrm{T}}$ — column vector of moments arising from the action of gravity;

$\mathrm{M} = \begin{pmatrix} \mathrm{M}_2 - \mathrm{M}_3 & \mathrm{M}_3 - \mathrm{M}_4 & \mathrm{M}_4 \end{pmatrix}^{\mathrm{T}}$ — column vector of control torques generated by actuators located in the joints of

the exoskeleton links; $q=(\varphi_2 \quad \varphi_3 \quad \varphi_4)^T$ — column vector of generalized coordinates, consisting of rotation angles of exoskeleton links; $J_{jk}\ (j,k=2,3,4)$ — moments of inertia of exoskeleton links; $\mu_k\ (k=2,3,4)$ — coefficients of linear friction in the joints of the exoskeleton links; $M_{Gk}\ (k=2,3,4)$ — maximum values of the moments of gravitational forces perceived by the output links of the drives.

Let the laws of change of angles and their derivatives be given for program motion:

$$\varphi_i^P=\varphi_i^P(t),\quad \dot\varphi_i^P=\dot\varphi_i^P(t),\quad \ddot\varphi_i^P=\ddot\varphi_i^P(t).\quad (i=2,3,4). \tag{2}$$

To control the exoskeleton motion, it is proposed to create control actions in the form of a sum of control moments:

– with software management $M_i^P=M_i\left(\varphi_i^P,\dot\varphi_i^P,\ddot\varphi_i^P\right)\quad (i=2,3,4)$;

– PID controller $M_i^{PID}=M_i\left(\varphi_i^P-\varphi_i,\dot\varphi_i^P-\dot\varphi_i,\ddot\varphi_i^P-\ddot\varphi_i\right),(i=2,3,4)$.

$$M_2=M_2^P+M_2^{PID},\quad M_3=M_3^P+M_3^{PID},\quad M_4=M_4^P+M_4^{PID}. \tag{3}$$

For program control, the values of control actions M_i^P can be calculated using the formulas [7]:

$$\begin{aligned}
M_4^P &= M_{G4}\cos\varphi_4^P+\mu_4\dot\varphi_4^P+J_4\ddot\varphi_4^P+J_{24}\left[\ddot\varphi_2^P\cos\left(\varphi_2^P-\varphi_4^P\right)-\left(\dot\varphi_2^P\right)^2\sin\left(\varphi_2^P-\varphi_4^P\right)\right]+\\
&+J_{34}\left[\ddot\varphi_3^P\cos\left(\varphi_3^P-\varphi_4^P\right)-\left(\dot\varphi_3^P\right)^2\sin\left(\varphi_3^P-\varphi_4^P\right)\right],\\
M_3^P &= M_{G3}\cos\varphi_3^P+\mu_3\dot\varphi_3^P+J_3\ddot\varphi_3^P+J_{23}\left[\ddot\varphi_2^P\cos\left(\varphi_2^P-\varphi_3^P\right)-\left(\dot\varphi_2^P\right)^2\sin\left(\varphi_2^P-\varphi_3^P\right)\right]+\\
&+J_{34}\left[\ddot\varphi_4^P\cos\left(\varphi_3^P-\varphi_4^P\right)+\left(\dot\varphi_4^P\right)^2\sin\left(\varphi_3^P-\varphi_4^P\right)\right]+M_4^P,\\
M_2^P &= M_{G2}\cos\varphi_2^P+\mu_2\dot\varphi_2^P+J_2\ddot\varphi_2^P+J_{23}\left[\ddot\varphi_3^P\cos\left(\varphi_2^P-\varphi_3^P\right)+\left(\dot\varphi_3^P\right)^2\sin\left(\varphi_2^P-\varphi_3^P\right)\right]+\\
&+J_{24}\left[\ddot\varphi_4^P\cos\left(\varphi_2^P-\varphi_4^P\right)+\left(\dot\varphi_4^P\right)^2\sin\left(\varphi_2^P-\varphi_4^P\right)\right]+M_3^P.
\end{aligned} \tag{4}$$

Values M_i^{PID} are calculated according to the feedback principle (in the form of a PID controller):

$$\begin{aligned}
M_4^{PID} &= K_{D4}\frac{d}{dt}\left(\dot\varphi_4^P-\dot\varphi_4\right)+K_{P4}\left(\dot\varphi_4^P-\dot\varphi_4\right)+K_{I4}\int_0^t\left(\dot\varphi_4^P(t_1)-\dot\varphi_4(t_1)\right)dt_1,\\
M_3^{PID} &= K_{D3}\frac{d}{dt}\left(\dot\varphi_3^P-\dot\varphi_3\right)+K_{P3}\left(\dot\varphi_3^P-\dot\varphi_3\right)+K_{I3}\int_0^t\left(\dot\varphi_3^P(t_1)-\dot\varphi_3(t_1)\right)dt_1+M_4^{PID},\\
M_2^{PID} &= K_{D2}\frac{d}{dt}\left(\dot\varphi_2^P-\dot\varphi_2\right)+K_{P2}\left(\dot\varphi_2^P-\dot\varphi_2\right)+K_{I2}\int_0^t\left(\dot\varphi_2^P(t_1)-\dot\varphi_2(t_1)\right)dt_1+M_3^{PID},
\end{aligned} \tag{5}$$

or

$$\begin{aligned}
M_4^{PID} &= K_{D4}\left(\ddot\varphi_4^P-\ddot\varphi_4\right)+K_{P4}\left(\dot\varphi_4^P-\dot\varphi_4\right)+K_{I4}\left(\varphi_4^P-\varphi_4\right),\\
M_3^{PID} &= K_{D3}\left(\ddot\varphi_3^P-\ddot\varphi_3\right)+K_{P3}\left(\dot\varphi_3^P-\dot\varphi_3\right)+K_{I3}\left(\varphi_3^P-\varphi_3\right)+M_4^{PID},\\
M_2^{PID} &= K_{D2}\left(\ddot\varphi_2^P-\ddot\varphi_2\right)+K_{P2}\left(\dot\varphi_2^P-\dot\varphi_2\right)+K_{I2}\left(\varphi_2^P-\varphi_2\right)+M_3^{PID}.
\end{aligned} \tag{6}$$

Here, the coefficients of the PID controller K_{Pi}, K_{it}, K_{Di} (i = 2, 3, 4) can be:

– constant (they are found from the stability conditions);

– time functions (found from solving optimal control problems [9, 13].

One of the problems of creation of control actions in the form of a PID controller is possible errors in the differentiation of measurement information. To avoid them, we use:

– encoders (for measuring the current rotation angles φ_i of the exoskeleton links);

– inertial sensor blocks of micromechanical gyroscopes (for measuring angular rates $\dot{\varphi}_i$) and accelerometers (for estimating angular rates $\dot{\varphi}_i$ and accelerations $\ddot{\varphi}_i$).

The model for measuring rotation angles using encoders can be presented as:

$$\varphi_{E2} = \varphi_2, \quad \varphi_{E3} + \varphi_{E2} = \varphi_3, \quad \varphi_{E4} + \varphi_{E3} + \varphi_{E2} = \varphi_4, \tag{7}$$

where $\varphi_{E2}, \varphi_{E3}, \varphi_{E4}$ — indications of encoders located in joints A_1, A_2, A_3 (Fig. 1).

The model of angular rate measurements using micromechanical gyroscopes can be written as:

$$\Omega_{G2} = \dot{\varphi}_2, \quad \Omega_{G3} = \dot{\varphi}_3, \quad \Omega_{G4} = \dot{\varphi}_4, \tag{8}$$

where Ω_{G2}, Ω_{G3}, Ω_{G4} — indications of gyroscopes attached to the links of the exoskeleton.

To estimate angular rate and accelerations using accelerometers, a pair of two-axis accelerometers can be used, which are located at opposite ends of each of the links. They measure the apparent accelerations associated with the corresponding links in projections on $x_i y_i$-axis (i = 1, 2, 3).

$$\begin{aligned}
&\mathrm{f}^{A_2}_{A_1A_2} - \mathrm{f}^{A_1}_{A_1A_2} = \left(\left(\mathrm{f}^{A_2}_{A_1A_2} - \mathrm{f}^{A_1}_{A_1A_2}\right)_{x_1} \quad \left(\mathrm{f}^{A_2}_{A_1A_2} - \mathrm{f}^{A_1}_{A_1A_2}\right)_{y_1}\right)^{\mathrm{T}} = \left(\mathrm{l}_1\dot{\varphi}_2^2 \quad -\mathrm{l}_1\ddot{\varphi}_2\right)^{\mathrm{T}},\\
&\mathrm{f}^{A_3}_{A_2A_3} - \mathrm{f}^{A_2}_{A_2A_3} = \left(\left(\mathrm{f}^{A_3}_{A_2A_3} - \mathrm{f}^{A_2}_{A_2A_3}\right)_{x_2} \quad \left(\mathrm{f}^{A_3}_{A_2A_3} - \mathrm{f}^{A_2}_{A_2A_3}\right)_{y_2}\right)^{\mathrm{T}} = \left(\mathrm{l}_2\dot{\varphi}_3^2 \quad -\mathrm{l}_2\ddot{\varphi}_3\right)^{\mathrm{T}},\\
&\mathrm{f}^{C}_{A_3C} - \mathrm{f}^{A_3}_{A_3C} = \left(\left(\mathrm{f}^{C}_{A_3C} - \mathrm{f}^{A_3}_{A_3C}\right)_{x_3} \quad \left(\mathrm{f}^{C}_{A_3C} - \mathrm{f}^{A_3}_{A_3C}\right)_{y_3}\right)^{\mathrm{T}} = \left(\mathrm{l}_3\dot{\varphi}_4^2 \quad -\mathrm{l}_3\ddot{\varphi}_4\right)^{\mathrm{T}}.
\end{aligned} \tag{9}$$

Here, $\mathrm{f}^{A_1}_{A_1A_2}, \mathrm{f}^{A_2}_{A_1A_2}$ — vectors of readings of two-axis accelerometers mounted on link A_1A_2 and located at points A_1 and A_2, respectively; $\mathrm{f}^{A_2}_{A_2A_3}, \mathrm{f}^{A_3}_{A_2A_3}$ — vectors of readings of two-axis accelerometers mounted on link A_2A_3 and located at points A_2 and A_3, respectively; $\mathrm{f}^{A_3}_{A_3C}, \mathrm{f}^{C}_{A_3C}$ — vectors of readings of two-axis accelerometers mounted on link A_3C and located at points A_3 and C, respectively; $l_1 = |A_1A_2|, l_2 = |A_2A_3|, l_3 = |A_3C|$ — distances between pairs of accelerometers attached to links A_1A_2, A_2A_3 and A_3C, respectively.

We combine equations (7)–(9) and write formulas for estimating the angles of rotation, angular rates, and accelerations:

$$\begin{aligned}
&\varphi_2 = \varphi_{E2}, \quad \varphi_3 = \varphi_{E3} + \varphi_{E2}, \quad \varphi_4 = \varphi_{E4} + \varphi_{E3} + \varphi_{E2}, \quad \dot{\varphi}_2 = \Omega_{G2}, \quad \dot{\varphi}_3 = \Omega_{G3}, \quad \dot{\varphi}_4 = \Omega_{G4},\\
&\ddot{\varphi}_2 = -\frac{\left(\mathrm{f}^{A_2}_{A_1A_2} - \mathrm{f}^{A_1}_{A_1A_2}\right)_{y_1}}{\mathrm{l}_1}, \quad \ddot{\varphi}_3 = -\frac{\left(\mathrm{f}^{A_3}_{A_2A_3} - \mathrm{f}^{A_2}_{A_2A_3}\right)_{y_2}}{\mathrm{l}_2}, \quad \ddot{\varphi}_4 = -\frac{\left(\mathrm{f}^{C}_{A_3C} - \mathrm{f}^{A_3}_{A_3C}\right)_{y_3}}{\mathrm{l}_3}.
\end{aligned} \tag{10}$$

To correct estimates of angular speed modules, the equations can be used:

$$\left(\mathrm{f}^{A_2}_{A_1A_2} - \mathrm{f}^{A_1}_{A_1A_2}\right)_{x_1} = \mathrm{l}_1\dot{\varphi}_2^2, \quad \left(\mathrm{f}^{A_3}_{A_2A_3} - \mathrm{f}^{A_2}_{A_2A_3}\right)_{x_2} = \mathrm{l}_2\dot{\varphi}_3^2, \quad \left(\mathrm{f}^{C}_{A_3C} - \mathrm{f}^{A_3}_{A_3C}\right)_{x_3} = \mathrm{l}_3\dot{\varphi}_4^2. \tag{11}$$

Thus, to estimate the rotation angles, angular rates and angular accelerations of the exoskeleton links, measurements can be processed with a moving average filter, Kalman filter algorithm, etc. [10, 13, 15].

In the simplest version of closing the feedback circuit when forming the control, we obtain expressions for the control moments:

$$M_4 = M_4^P + K_{D4}\left(\ddot{\varphi}_4^P + \frac{\left(f_{A_3C}^C - f_{A_3C}^{A_3}\right)_{y_3}}{l_3}\right) + K_{P4}\left(\dot{\varphi}_4^P - \Omega_{G4}\right) + K_{I4}\left(\varphi_4^P - \varphi_{E4} - \varphi_{E3} - \varphi_{E2}\right),$$

$$M_3 = M_3^P + K_{D3}\left(\ddot{\varphi}_3^P + \frac{\left(f_{A_2A_3}^{A_3} - f_{A_2A_3}^{A_2}\right)_{y_2}}{l_2}\right) + K_{P3}\left(\dot{\varphi}_3^P - \Omega_{G3}\right) + K_{I3}\left(\varphi_3^P - \varphi_{E3} - \varphi_{E2}\right) + M_4^{PID}, \quad (12)$$

$$M_2 = M_2^P + K_{D2}\left(\ddot{\varphi}_2^P + \frac{\left(f_{A_1A_2}^{A_2} - f_{A_1A_2}^{A_1}\right)_{y_1}}{l_1}\right) + K_{P2}\left(\dot{\varphi}_2^P - \Omega_{G2}\right) + K_{I2}\left(\varphi_2^P - \varphi_{E2}\right) + M_3^{PID}.$$

The introduction of angular acceleration feedback into the control system provides the diagonalization of the inertial forces matrix to reduce the cross-influence between generalized coordinates.

We simulate the exoskeleton motions to test the operability of the proposed control law. As a program motion, consider:

– change of position from sitting to standing [7];

– stabilization of the vertical position of the exoskeleton with initial deviations of the links from the vertical.

Research Results. For numerical simulation of the system, we took the parameters of the mathematical model of the exoskeleton from [6, 7]. We considered a special case by choosing the same coefficients of the PID controller for each drive: $K_{Pi} = 1{,}000\ N \cdot m \cdot s$, $K_{Ii} = 1{,}000\ N \cdot m$, $K_{Di} = 0\ N \cdot m/s\ (i = 2,3,4)$. Figure 2 shows the time dependences for the rotation angles and angular rates of the exoskeleton links. They were obtained at control moments corresponding to rising from a sitting position. As can be seen from Figure 2 *a*, at the end of the motion, the rotation angles of each link are equal $\varphi_2 = \varphi_3 = \varphi_4 = 90°$, which corresponds to standing.

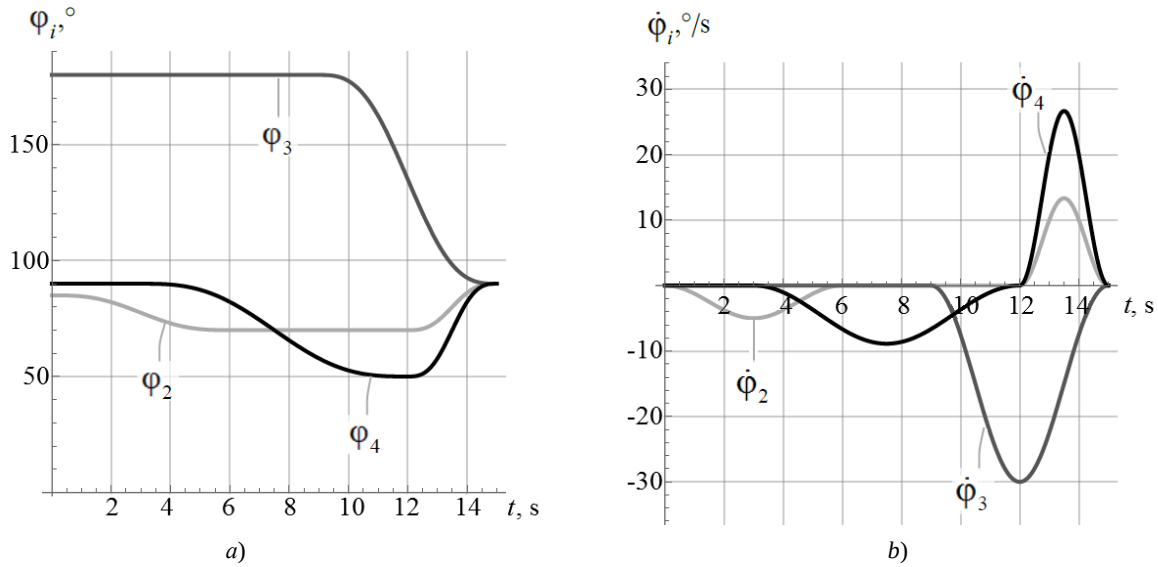

a) *b*)

Fig. 2. Simulation results of rising from a sitting position without initial deviations from the program motion in the angles of rotation of the exoskeleton links: *a* — rotation angles of the links; *b* — angular rates of the links

Now let us consider the case with deviations of about 20° in the rotation angles of the links compared to the initial position set in the program motion. The simulation results of rising from a sitting position are shown in Figure 3. As in Figure 2, at the end of the motion time, the values of the rotation angles were equal to $\varphi_2 = \varphi_3 = \varphi_4 = 90°$. Consequently, the use of a combination of software control and control in the form of a PID controller accurately brought the exoskeleton to the desired position.

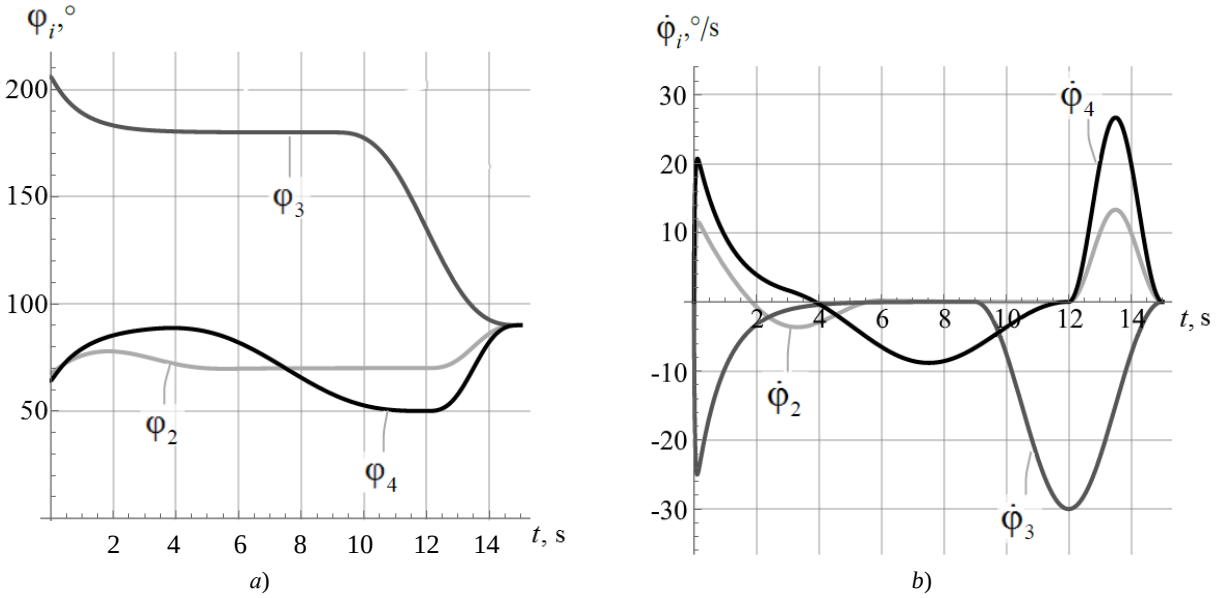

Fig. 3. Simulation results of rising from a sitting position with initial deviations from the program motion in the rotation angles of the exoskeleton links: *a* — rotation angles of the links; *b* — angular rates of the links

Thus, when modeling program motion, the operability of the proposed law of formation of control actions described in (4) and (12) was shown.

The vertical position of the exoskeleton is unstable without control; therefore, disturbing factors can cause deviations from equilibrium up to the falling of the exoskeleton.

We checked the operability of the proposed control in the task of stabilizing the vertical position of the exoskeleton. Values for the program motion were: $\varphi_2^d(t) = \varphi_3^d(t) = \varphi_4^d(t) = 90°$. We considered the case when there were deviations of about 20° from the vertical position in the rotation angles of the links (Fig. 4).

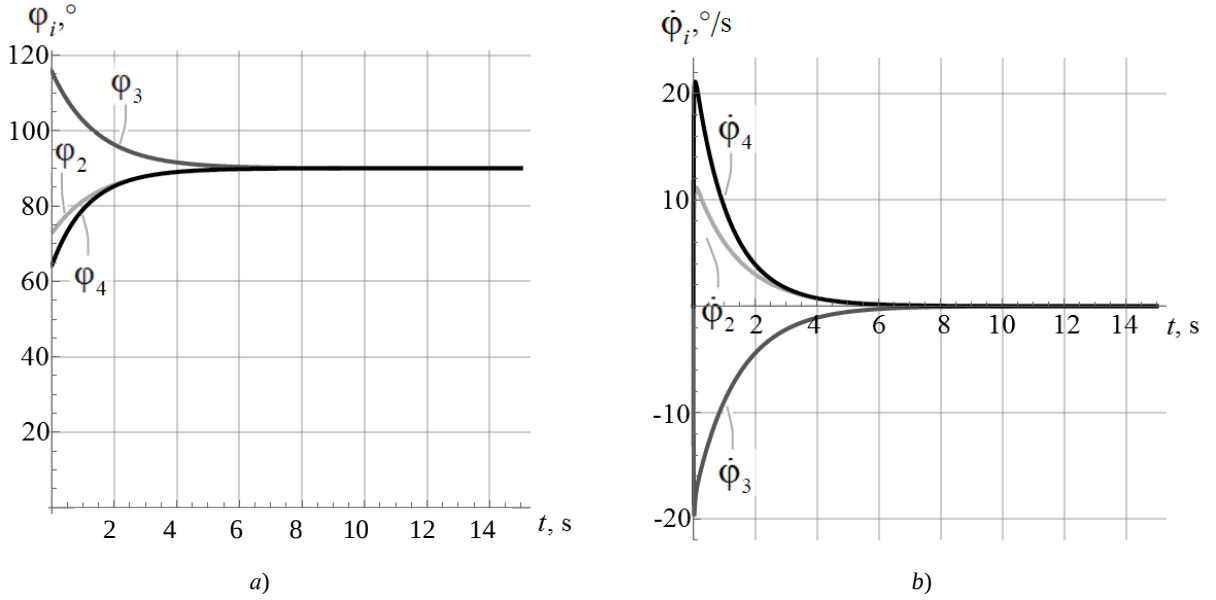

Fig. 4. Simulation results of stabilization of the vertical position with initial deviations from the program motion in the rotation angles of the exoskeleton links: *a* — angles of rotation of the links; *b* — angular rates of the links

Figure 4 shows that the proposed control provides stabilization of the vertical position of the exoskeleton links.

For comparison, we present the results of modeling the stabilization of the vertical position using the following values of the coefficients of the PID controller: $K_{Pi} = 1{,}000\ N \cdot m \cdot s$, $K_{Ii} = 1{,}000\ N \cdot m$, $K_{Di} = 100\ N \cdot m/\text{s}\ (i = 2,3,4)$ (Fig. 5).

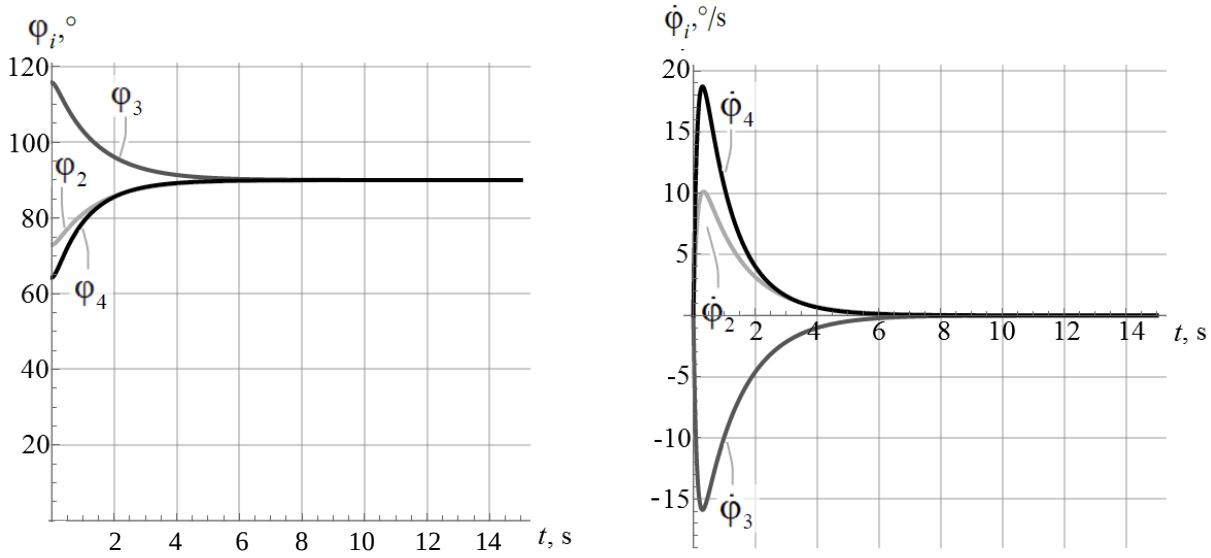

a) *b*)

Fig. 5. Simulation results of stabilization of the vertical position with initial deviations from the program motion in the rotation angles of the exoskeleton links: *a* — angles of rotation of the links; *b* — angular rates of the links

It can be seen from Figure 5 that when using the differential link ($K_{Di} \neq 0$) of the regulator, it was possible to reduce emissions in the dependences of the angular rates of the exoskeleton links compared to the case $K_{Di} = 0$ (Fig. 4 *b*).

Thus, the possibility of controlling the lower-extremity powered exoskeleton links using the readings of encoders and blocks of inertial sensors (micromechanical gyroscopes and accelerometers) was considered. The simulation results have validated this approach.

Discussion and Conclusions. The proposed solution to the problem of controlling the motion of the exoskeleton can be used in medical applications, including for the verticalization of musculoskeletal patients.

Thus, the data of the inertial sensor blocks can be used in the task of assessing the state of the exoskeleton links — their angular rates and accelerations. At the same time, there is no need for numerical differentiation of the measuring information of the encoders. Therefore, feedback on angular accelerations can be introduced into the control system, which makes it possible to improve transients when controlling the exoskeleton motion.

References

1. De Looze MP, Bosch T, Krause F, et al. Exoskeletons for Industrial Application and Their Potential Effects on Physical Work Load. Ergonomics. 2015;59:671–681. https://doi.org/10.1080/00140139.2015.1081988

2. Gevorkyan AA, Kotov SV, Lizhdvoy VYu. Robotic Mechanotherapy: The Possibility to Use an Exoskeleton for Lower Limb Rehabilitation in Patients with Multiple Sclerosis and Impaired Walking Function. Almanac of Clinical Medicine. 2020;48:7–12.

3. Vorobiev AA, Zasypkina OA, Krivonozhkina PS, et al. Current Use of Exoskeleton and Prospects of its Implementation in Habilitation and Rehabilitation of Disabled People (Analytical Review). Journal of VolgSMU. 2015;54:9–17.

4. Novozhilov IV, Terekhov AV, Zabelin AV, et al. Trekhzvennaya matematicheskaya model' dlya zadachi stabilizatsii vertikal'noi pozy cheloveka. In book: Matematicheskoe modelirovanie dvizhenii cheloveka v norme i pri nekotorykh vidakh patologii. Moscow: Publ. House of the Faculty of Mechanics and Mathematics, Moscow State University; 2005. P. 7–20. (In Russ.)

5. Panovko GY, Savin SI, Yatsun SF, et al. Simulation of Exoskeleton Sit-to-Stand Movement. Journal of Machinery Manufacture and Reliability. 2016;3:19–24.

6. Saypulaev MR, Zuev YuYu, Saypulaev GR, et al. Development of the Lower Extremity Exoskeleton Dynamics Model Using in the Task of the Patient Verticalization. Journal of Physics: Conference Series. 2021;2096:0120421. https://doi.org/10.1088/1742-6596/2096/1/012042

7. Zuev YuYu, Saypulaev MR, Doni V. Laws of Motion of the Lower Extremities and Structural-parametric Synthesis of Electro-Hydraulic Executive Modules of the Active Exoskeleton According to the Criterion of Energy Sufficiency. Journal of Physics: Conference Series. 2021;2096:012044. 10.1088/1742-6596/2096/1/012044

8. Yatsun SF, Rukavitsy AN. Determination of Parameters of Drives Bioengineered Mechatronic Modules for Exoskeletal Human Lower Extremity. Proceedings of Southwest State University. 2012; 2-1:196–200.

9. Savin SI, Yatsun AS, Yatsun SF. Energy-Efficient Algorithm of Control of Exoskeleton Verticalization. Journal of Machinery Manufacture and Reliability. 2017;46:512–517.

10. Aliman N, Ramli R, Haris SM, et al. A Robust Adaptive-Fuzzy-Proportional-Derivative Controller for a Rehabilitation Lower Limb Exoskeleton. International Journal of Engineering Science and Technology. 2022;35:101097. 10.1016/j.jestch.2022.101097

11. Amiri MS, Ramli R, Ibrahim MF, et al. Adaptive Particle Swarm Optimization of PID Gain Tuning for Lower-Limb Human Exoskeleton in Virtual Environment. Mathematics. 2020;8:2040. 10.3390/math8112040

12. Dongyoung Lee, Buchun Song, Sang Yong Park, et al. Development and Control of an Electro-Hydraulic Actuator System for an Exoskeleton Robot. Applied Sciences. 2019;9:4295. 10.3390/app9204295

13. Lora-Millan JS, Hidalgo AF, Rocon E. An IMUs-Based Extended Kalman Filter to Estimate Gait Lower Limb Sagittal Kinematics for the Control of Wearable Robotic Devices. IEEE Access. 2021;9:144540–144554. 10.1109/ACCESS.2021.3122160

14. Duong Mien Ka, Cheng Hong, Tran Huu Toan, et al. Minimizing Human-Exoskeleton Interaction Force by Using Global Fast Sliding Mode Control. International Journal of Control, Automation and Systems. 2016;14:1064–1073. 10.1007/s12555-014-0395-7

15. Balakrishnan AV. Teoriya fil'tratsii Kalmana. Moscow: Kniga po trebovaniyu; 2021. 164 p. (In Russ.)

Received 11.07.2022
Revised 01.08.2022
Accepted 10.08.2022

About the Authors:

Saypulaev, Gasan R., postgraduate student and assistant of the Department of Robotics, Mechatronics, Dynamics and Machine Strength, National Research University (MPEI) (14, Krasnokazarmennaya St., Moscow, 111250, RF), ScopusID, ORCID, saypulaevgr@mail.ru

Saypulaev, Musa R., postgraduate student of the Department of Robotics, Mechatronics, Dynamics and Machine Strength, National Research University (MPEI) (14, Krasnokazarmennaya St., Moscow, 111250, RF), ScopusID, ORCID, saypulaevmr@mail.ru

Merkuryev, Igor V., Head of the Department of Robotics, Mechatronics, Dynamics and Machine Strength, National Research University (MPEI) (14, Krasnokazarmennaya St., Moscow, 111250, RF), Dr.Sci. (Eng), associate professor, ScopusID, ORCID, nir4s@ya.ru

Adamov, Boris I., associate professor of the Department of Robotics, Mechatronics, Dynamics and Machine Strength, National Research University (MPEI) (14, Krasnokazarmennaya St., Moscow, 111250, RF), Cand.Sci. (Phys.-Math.), associate professor, ScopusID, ORCID, adamoff.b@yandex.ru

Garcia, Roilan B., postgraduate student of the Department of Robotics, Mechatronics, Dynamics and Machine Strength, National Research University (MPEI) (14, Krasnokazarmennaya St., Moscow, 111250, RF), ORCID, roilangarcia76@gmail.com

Claimed contributorship:

G. R. Saypulaev: basic concept formulation; research objectives and tasks setting; computational analysis; text preparation; formulation of conclusions. M. R. Saypulaev: development of a mathematical model; computational analysis; text preparation. I. V. Merkuryev: academic advising; analysis of the research results; the text revision; correction of the conclusions. B. I. Adamov: formulation of the basic concept of the study; academic advising; analysis of the research results; correction of the conclusions. R. B. Garcia: computational analysis; text preparation.

Conflict of interest statement

The authors do not have any conflict of interest.

All authors have read and approved the final manuscript.

MECHANICS

UDC 539.3
https://doi.org/10.23947/2687-1653-2022-22-3-214-223

Original article

Critical Loads of Uniformly Compressed Orthotropic Rectangular Plate on an Elastic Base

Isa M. Peshkhoev ✉, **Boris V. Sobol**
Don State Technical University, 1, Gagarin sq., Rostov-on-Don, Russian Federation
✉ peshkhoev@rambler.ru

Abstract

Introduction. The problem of critical loads of a compressed orthotropic rectangular plate on an elastic base was considered. The following orthotropy parameters were set for the plate: Poisson coefficients, Young's modules for the main directions, and the shear modulus of the plate material. The components of the compressive load were uniformly distributed along two opposite edges of the plate and acted parallel to the coordinate axes. The edges of the plate were loosely pinched or pivotally supported. Cases were also considered when two parallel edges of the plate were free from loads, and the other two were freely pinched or pivotally supported.

Materials and Methods. The problem was studied on the basis of a system of nonlinear Kármán-type equilibrium equations. The critical values of the load parameter were determined from a linearized problem based on a trivial solution. At the same time, the variational method in combination with the finite difference method was used to solve the boundary eigenvalue problem.

Results. The problem was reduced to solving a parametric linear boundary eigenvalue problem. In case of boundary conditions of a movable hinge support, exact formulas of eigenvalues and eigenfunctions were given. While in case of free edge pinching, a variational method was used in combination with a finite-difference method, and a computer program for solving the problem was built. It was established that one or two eigenfunctions expressing the deflection of the plate could correspond to the critical value of the compressive load parameter at which the stability of the compressed plate was lost. The results of numerical calculations of the critical values of the compressive load at different values of the orthotropy parameters were presented, and graphs of the corresponding equilibrium forms were constructed. For the case of a long orthotropic plate on an elastic base, it was established that the main term of the asymptotic expansion of the solution to the linear eigenvalue problem was determined from the problem of critical loads of a compressed beam on an elastic base with an elastic modulus that coincides with the elastic modulus of the plate in the longitudinal direction.

Discussion and Conclusions. The problem of critical loads of an orthotropic plate compressed in two directions lying on an elastic base was investigated. As the compressive load component increased along one direction, the critical value of the load compressing the plate along the other direction decreased. If an orthotropic plate was compressed by a load along a direction that corresponded to a greater bending stiffness, then the critical value of the loss of stability was greater than the critical value of the compressive load acting along the direction of a lesser bending stiffness. The presence of an elastic foundation increased the bearing capacity of the compressed plate.

Keywords: critical load, elastic orthotropic plate, equilibrium stability, elastic base, parametric eigenvalue boundary problem.

Acknowledgments. The authors would like to thank the reviewers, and express their gratitude to the editorial board of the journal "Advanced Engineering Research" for the assistance provided in the process of preparing the article.

For citation. I. M. Peshkhoev, B. V. Sobol. Critical Loads of Uniformly Compressed Orthotropic Rectangular Plate on an Elastic Base. Advanced Engineering Research, 2022, vol. 22, no. 3, pp. 214–223. https://doi.org/10.23947/2687-1653-2022-22-3-214-223

Introduction. L. M. Zubov in [1] derives the equilibrium equations of an elastic plate containing sources of internal stresses in the form of dislocations and disclinations, which are a modification of the Karman equations. In this work, the problem of bending a thin plate (membrane) under the action of internal stresses caused by defects is also solved. In [2–5], the theory of dislocations and disclinations is used in the study of the behavior of plates and shells. In article [6], a general solution of the oscillation equation of a rectangular orthotropic plate with free edges is constructed. In [7, 8], asymptotic solutions of problems of statics and dynamics of narrow plates are constructed.

In [9], the problem of equilibria branching under the influence of a small normal pressure of a rectangular plate compressed in one direction with dislocations and disclinations is considered. The case is considered when the longitudinal edges of the plate are free from loads, and the other two edges are fixed. In [10], an asymptotic solution is provided for the problem of critical loads of a compressed narrow plate using a small parameter expansion of the relative width of the plate. In [11], the branching problem of the equilibria of an elastic rectangular plate with internal stress sources is investigated for the case when compressive loads are unevenly distributed along the edges. It is established that with even forms of the incompatibility function and even forms of distribution along the edges of compressive forces, the presence of a small normal load does not reduce the bearing capacity of the plate.

In work of Morozov N. F., Belyaev A. K., Tovstik P. E., Tovstik T. P. [12], an asymptotic derivation of two-dimensional equilibrium equations of a thin elastic inhomogeneous plate made of a general anisotropic material is presented. Conclusions about the forms of loss of stability of a compressed plate on an elastic soft base are formulated in [13]. In [14], the bending stiffness of a thin elastic multilayer plate with transversely isotropic layers is investigated. Two models of accounting for the effect of transverse shear are compared.

In [15], a model of thermoelastic viscoplastic deformation of a composite that is cross-reinforced with continuous fibers in arbitrary directions is constructed.

In [16], within the framework of a direct approach to plate theory, the problem of a hyperelastic plate with inhomogeneously distributed initial stresses is considered. The plate is considered as a material surface with five degrees of freedom (three displacements and two rotations). In [17], the stability of a uniformly compressed circular two-layer plate with an initially compressed or stretched layer is analyzed within the framework of nonlinear elasticity. A model of incompressible neo-Hookean material is used for determining the material ratio. The analysis of the dependence of the resulting critical stresses on the initial deformations and stiffness parameters is presented. In [18], the bending of a three-layer plate with surface and interfacial stresses is investigated, the theory of plates with first-order shear deformations and the Gurtin-Murdoch model of surface stresses are considered. The dependence of the plate stiffness parameters on the surface elasticity modules is analyzed. In [19], the problem of instability of a three-layer nonlinear elastic rectangular plate with a prestressed middle layer is considered.

In this paper, the influence of the parameters of the plate material and the elastic base parameter on the critical loads of the loss of stability of a compressed elastic rectangular orthotropic plate on an elastic base is investigated.

Materials and Methods. Let us consider an orthotropic rectangular plate lying on a linearly elastic base, which is compressed by forces *P* and *Q* along the *X* and *Y* axes. The equilibrium equations can be written as [7]:

$$\begin{cases} D_1\partial_X^4 W + 2D_3\partial_X^2\partial_Y^2 W + D_2\partial_Y^4 W + KW = [W,F], \\ \dfrac{1}{E_2}\partial_X^4 F + \left(\dfrac{1}{G} - \dfrac{2\nu_1}{E_1}\right)\partial_X^2\partial_Y^2 F + \dfrac{1}{E_1}\partial_Y^4 F = -\dfrac{1}{2}[W,W]. \end{cases} \quad (1)$$

Let us write the boundary conditions in the form:

$$\begin{cases} W = \partial_X W = 0, \quad \partial_Y\partial_X F = 0, \quad \partial_Y^2 F = -P \text{ at } |X| = a/2, \\ W = \partial_Y W = 0, \quad \partial_Y\partial_X F = 0, \quad \partial_X^2 F = -Q \text{ at } |Y| = b/2. \end{cases} \quad (2)$$

$$\begin{cases} W = \partial_X^2 W = 0, \quad \partial_Y\partial_X F = 0, \quad \partial_Y^2 F = -P \text{ at } |X| = a/2, \\ W = \partial_Y^2 W = 0, \quad \partial_Y\partial_X F = 0, \quad \partial_X^2 F = -Q \text{ at } |Y| = b/2. \end{cases} \quad (3)$$

$$\begin{cases} W = \partial_X W = 0, \quad \partial_Y\partial_X F = 0, \quad \partial_Y^2 F = -P \text{ at } |X| = a/2, \\ \partial_Y^2 W + \nu_1\partial_X^2 W = \partial_Y^3 W + (2-\nu_1)\partial_X^2\partial_Y W = \partial_Y\partial_X F = \partial_X^2 F = 0 \text{ at } |Y| = b/2. \end{cases} \quad (4)$$

$$\begin{cases} W = \partial_X^2 W = 0, \quad \partial_Y\partial_X F = 0, \quad \partial_Y^2 F = -P \text{ at } |X| = a/2, \\ \partial_Y^2 W + \nu_1\partial_X^2 W = \partial_Y^3 W + (2-\nu_1)\partial_X^2\partial_Y W = \partial_Y\partial_X F = \partial_X^2 F = 0 \text{ at } |Y| = b/2. \end{cases} \quad (5)$$

$[W,F] \equiv \partial_X^2 W\partial_Y^2 F + \partial_Y^2 W\partial_X^2 F - 2\partial_X\partial_Y W\partial_X\partial_Y F$, $D_i = E_i h^3/(12(1-\nu_1\nu_2))$, $i = 1,2$; $D_k = Gh^3/12$, $D_3 = D_1\nu_2 + 2D_k$, $E_1\nu_2 = E_2\nu_1$.

Here ν_1, ν_2, E_1, E_2, G — Poisson's coefficients, Young's modules for the main directions and the shear modulus of the plate material; D_1, D_2 — bending stiffness in the main directions; D_k — torsion stiffness; the function $W(X,Y)$ expresses deflection, and $F(X,Y)$ denotes the stress function; *h* — plate thickness, KW — base reaction; *K* — modulus of subgrade reaction; the origin of coordinates *X*, *Y* is in the center of the plate and the axes are parallel to its edges; ∂_X^n — partial derivative of the *n*-th order with respect to the variable *X*. We assume that the edges of the plate are loosely pinched (2) or pivotally supported (3). In this case, the compressive forces *P* and *Q* are evenly distributed along the edges $X = \pm a/2$ and $Y = \pm b/2$ respectively. The cases are also considered when two parallel edges of the plate $Y = \pm b/2$ are free from loads, and the other two are freely pinched (4) or pivotally supported (5). In these cases, the compressive load is applied only to the edges $X = \pm a/2$.

Let us assume that $F = \Phi - P\dfrac{Y^2}{2} - Q\dfrac{X^2}{2}$. Then, for the function Φ, homogeneous boundary conditions are valid $\Phi_{XY} = \Phi_{YY} = 0$ at $|X| = a/2$, $\Phi_{XY} = \Phi_{XX} = 0$ at $|Y| = b/2$. These conditions can be replaced by equivalent boundary conditions $\Phi = \Phi_X = 0$ at $|X| = a/2$; $\Phi = \Phi_Y = 0$ at $|Y| = b/2$. Let us move on to dimensionless variables by formulas:

$$X = ax;\ Y = by;\ \delta = \frac{b}{a};\ \Phi(X,Y) = D_1 f(x,y);\ W(X,Y) = w(x,y)h;\ K = \frac{kD_1}{b^4};\ P = \frac{pD_1}{b^2};\ Q = \frac{qD_1}{b^2};$$

$$\alpha = 6(1-\nu_1\nu_2);\ 2c_1 = \frac{E_2}{G} - 2\nu_2;\ c_2 = \frac{D_2}{D_1};\ c_3 = \frac{D_3}{D_1}.$$

Then system of equations (1) and boundary conditions (2), (3) can be rewritten as

$$\begin{cases}\delta^4\partial_x^4 w + 2c_3\delta^2\partial_x^2\partial_y^2 w + c_2\partial_y^4 w + \delta^4 k w = \delta^2[w,f] - p\delta^2\partial_x^2 w - q\partial_y^2 w,\\ \delta^4\partial_x^4 f + 2c_1\partial_x^2\partial_y^2\delta^2 f + c_2\partial_y^4 f = -\alpha c_2\delta^2[w,w].\end{cases} \tag{6}$$

$$[w,\partial_x w,f,\partial_x f]\big|_{|x|=1/2} = 0;\ [w,\partial_y w,f,\partial_y f]\big|_{|y|=1/2} = 0. \tag{7}$$

$$[w,\partial_x^2 w,f,\partial_x f]\big|_{|x|=1/2} = 0;\ [w,\partial_y^2 w,f,\partial_y f]\big|_{|y|=1/2} = 0. \tag{8}$$

$$[w,\partial_x w,f,\partial_x f]\big|_{|x|=1/2} = 0;\ [\partial_y^2 w + \nu_1\partial_x^2 w,\partial_y^3 w + (2-\nu_1)\partial_x^2\partial_y w,f,\partial_y f]\big|_{|y|=1/2} = 0. \tag{9}$$

$$[w,\partial_x^2 w,f,\partial_x f]\big|_{|x|=1/2} = 0;\ [\partial_y^2 w + \nu_1\partial_x^2 w,\partial_y^3 w + (2-\nu_1)\partial_x^2\partial_y w,f,\partial_y f]\big|_{|y|=1/2} = 0. \tag{10}$$

For any values of the parameters *k*, *p*, *q* the nonlinear boundary value problem (6) with any of the conditions (7)–(10) satisfies a trivial solution $(w_*,f_*) = (0,0)$.

Let us denote by E^2 the set of vector functions $f = (f_1,f_2)$ with a finite norm, which is determined using the scalar product:

$$\langle f,g\rangle_{E^2} = \iint_\Omega (f_1g_1 + f_2g_2)\,dxdy;\quad f = (f_1,f_2), g = (g_1,g_2). \tag{11}$$

By E^1 we denote the space of infinitely differentiable vector functions $u = (w,F)$, $v = (w_1,F_1)$ in the domain $\Omega = \{(x,y): |x| < 1/2, |y| < 1/2\}$, which satisfy one of the boundary conditions (5) or (6) on the boundary $\partial\Omega$ of the domain Ω. We define the norm in E^1 using the scalar product

$$\langle u,v\rangle_{E^1} = \sum_{i+j\le 4}\left\langle \frac{\partial^{i+j}u}{\partial x^i\partial y^j}, \frac{\partial^{i+j}v}{\partial x^i\partial y^j}\right\rangle_{E^2}. \tag{12}$$

The boundary value problem (6) with one of the boundary conditions (7)–(10) can be considered as a nonlinear operator equation

$$M_0 u = \Pi u,\quad u = (w,f) \in E^1, \tag{13}$$

where

$$M_0 u \equiv \begin{pmatrix}\delta^4\partial_x^4 w + 2c_3\delta^2\partial_x^2\partial_y^2 w + c_2\partial_y^4 w + kw + p\delta^2\partial_x^2 w + q\partial_y^2 w\\ \delta^4\partial_x^4 f + 2c_1\partial_x^2\partial_y^2\delta^2 f + c_2\partial_y^4 f\end{pmatrix};\ \Pi u \equiv \begin{pmatrix}\delta^2[w,f]\\ -\alpha c_2\delta^2[w,w]\end{pmatrix}. \tag{14}$$

Here M_0 — linear, and Π — nonlinear operators, since

$$[w,f] \equiv \partial_x^2 w\partial_y^2 f + \partial_y^2 w\partial_x^2 f - 2\partial_x\partial_y w\partial_x\partial_y f.$$

From the results of the works of I. I. Vorovich and N. F. Morozov, it follows [9] that the operators M_0 and Π act from the space E^1 to E^2. Let *k* = 0, *p* = 0, *q* = 0. Then equation (9) has a unique trivial solution $u_* = (w_*,f_*) = (0,0)$. With small changes in the values of the parameters p, q and k the trivial solution remains the only one. If, for any small values of a number $\varepsilon > 0$ and the fixed value k there are parameter values p, q, that satisfy the inequality $|p-p_0| + |q-q_0| < \varepsilon$ and for which there are at least two solutions to equation (9), then the point $(p_0, q_0,)$ is called the branching point (or bifurcation point) [9] of this equation. It is shown in [9] that in order to find the bifurcation point (p_0, q_0), it is necessary to solve the eigenvalue boundary value problem, which is a linearized equation on a trivial solution

$$M_0 u = 0. \tag{15}$$

The eigenvalues (p_0, q_0) are the critical values of the parameters of the compressive load (p, q). Considering (13) and (14), equation (15) can be written as the following eigenvalue boundary value problem: to find values of the parameter *p*, such that for fixed values of the base parameter (modulus of subgrade reaction) *k* and the load parameter *q* along the *y* axis, the following problem has a nontrivial solution:

$$\delta^4\partial_x^4 w + 2c_3\delta^2\partial_x^2\partial_y^2 w + c_2\partial_y^4 w + kw + q\partial_y^2 w = -p\delta^2\partial_x^2 w, \tag{16}$$

$$\left[w, \partial_x w\right]\Big|_{|x|=1/2} = 0;\ \left[w, \partial_y w\right]\Big|_{|y|=1/2} = 0, \tag{17}$$

$$\left[w, \partial_x^2 w\right]\Big|_{|x|=1/2} = 0;\ \left[w, \partial_y^2 w\right]\Big|_{|y|=1/2} = 0, \tag{18}$$

$$\left[w, \partial_x w\right]\Big|_{|x|=1/2} = 0;\ \left[\partial_y^2 w + \nu_1\partial_x^2 w, \partial_y^3 w + (2-\nu_1)\partial_x^2\partial_y w, f, \partial_y f\right]\Big|_{|y|=1/2} = 0, \tag{19}$$

$$\left[w, \partial_x^2 w\right]\Big|_{|x|=1/2} = 0;\ \left[\partial_y^2 w + \nu_1\partial_x^2 w, \partial_y^3 w + (2-\nu_1)\partial_x^2\partial_y w, f, \partial_y f\right]\Big|_{|y|=1/2} = 0. \tag{20}$$

In this case, the critical value of the loss of stability of the compressed plate corresponds to the minimum eigenvalue of the parameter *p*, and the eigenfunction corresponding to this value shows the form of equilibrium after the loss of stability. For the case of the hinge support of the edges (18), exact solutions can be written for equation (16):

$$p_{m,n} = \frac{\left(\delta^4 m^4 + 2c_3 m^2 n^2 + c_2 n^4\right)\pi^4 - q\pi^2 n^2 + k}{\pi^2 m^2};\ w_{m,n} = \sin\pi m\left(x - \frac{1}{2}\right)\sin\pi n\left(y - \frac{1}{2}\right), \tag{21}$$

where *m* and *n* are arbitrary natural numbers.

From the analysis of formulas (21), it follows that with different ratios of the plate edge lengths δ, the physical parameters of the orthotropy of the plate material c_3, c_2, the parameter *q* of the compressive load along the *y* axis, and the modulus of subgrade reaction *k* (characterizing the reaction of the base), one or more half-waves in the form of equilibrium (21) can correspond to the critical load value $p_* = \min\limits_{m,n>0} p_{m,n}$. In this case, the so-called buckling by two proper forms is possible, when, for example, $p_* = \min\limits_{m,n>0} p_{m,n} = p_{1,1} = p_{2,1}$. Such cases are listed below. To solve the problem (16) with boundary conditions of free pinching of the edges (17), a variational method is used in combination with a finite-difference method, which was justified in [9, 10] and is easily transferred to the case of an orthotropic plate. At the same time, the computer program developed for this task was tested on the solution of the problem (16), (18). In addition, a computer program has been developed for solving the variational method in combination with the finite difference method of the problem (16) with each of the boundary conditions (19), (20). For these cases, test examples of the corresponding boundary value problems have been constructed.

In [7], in the problem of asymptotic integration of the equation of small oscillations of a long (*b* << *a*) rectangular orthotropic plate, an expansion of the solution by small parameter degrees $\delta = b/a$ is constructed and it is shown that the main expansion is determined from the equation of vibrations of a beam with an elastic modulus $E = E_1$. Repeating the reasoning of works [7] and [10], we will look for a solution to problem (16) with boundary conditions (19) or (20) in the form of series:

$$p = \sum_{i=0}^{\infty} p_{2i}\delta^{2i},\ w = \sum_{i=0}^{\infty} w_{2i}\delta^{2i}. \tag{22}$$

It can be shown that the main term of the asymptotic expansion (22) of the solution to problem (16) with boundary conditions (19) or (20) is determined from the problem in dimensionless variables about the critical loads of a compressed elastic beam on an elastic base with freely pinched or movably hinged edges:

$$\left(1-\nu_1^2\right)w_0'''' + kw_0 + p_0 w_0'' = 0, \tag{23}$$

$$w_0 = w_0' = 0, \tag{24}$$

$$w_0 = w_0'' = 0. \tag{25}$$

Here the prime symbol indicates the ordinary derivative of a function depending on the variable *x*. It is possible to construct an algorithm for determining all coefficients of the terms of the expansions (22), but the authors will not do this in this paper.

When moving to dimensional variables from (23)–(25), we obtain the problem of critical loads of a compressed beam with an elastic modulus $E = E_1$. The eigenvalue problem (23) with boundary conditions (25) has an exact solution

$$p_m = \pi^2 m^2 + \frac{k}{\pi^2 m^2};\ w_m(x) = \sin(\pi m x). \tag{26}$$

In the case of boundary conditions (24), problem (23) is solved by the variational-difference method.

Research Results. Numerical calculations of the critical values of the load parameter *p* compressing along the direction of the *x* axis with fixed values of the modulus of subgrade reaction *k* and fixed values of the load parameter *q* compressing along the direction of the *y* axis and the specified values of the orthotropy parameters of the plate material are carried out. The plate equilibrium forms corresponding to critical loads are constructed.

Example 1. Let us consider an example of a square orthotropic plate from work [16] "plywood of the first type" — three-ply: if you direct the *x* axis along the fibers of the face (upper and lower of the three layers), then Young's modules along the fibers and across, respectively, are equal to $E_1 = 1.4 \cdot 10^5\ \text{kg/cm}^2$ and $E_2 = \frac{1.4}{12} \cdot 10^5\ \text{kg/cm}^2$; Poisson coefficients — $\nu_1 = 0.46$ and $\nu_2 = 0.46/12$; shear modulus for the main directions of elasticity $G = 1.2 \cdot 10^5\ \text{kg/cm}^2$. Then, for the problem in dimensionless variables (16), we obtain $\delta = \frac{b}{a} = 1$; $c_2 = \frac{D_2}{D_1} = \frac{E_2}{E_1} = \frac{1}{12} = 0.083$; $c_3 = \frac{D_3}{D_1} = 0.207$ taking into account the above formulas for the transition to dimensionless variables. Let the edges of the plate be pivotally supported. Then, from (21) for $k = 0$, $q = 8.193$, it follows $p_* = \min\limits_{m,n>0} p_{m,n} = p_{1,1} = p_{1,2} = 6.580$. Two forms of equilibrium correspond to this critical value. Table 1 shows the values of the critical load p^* loss of stability of an orthotropic plate with pinched edges compressed along the *x* axis for different values of the modulus of subgrade reaction *k* and different values of the compressive load along the *y* axis. Table 1 shows that with an increase in the value of the modulus of subgrade reaction, the critical load of the loss of stability of the compressed orthotropic plate also increases.

Table 1

Dependence of the critical load p^* on the base parameter *k* at different *q*

	p^*		
k	*q* = 0	*q* = 10	*q* = 20
0	47.455	38.011	5.298
1,000	112.142	105.841	88.1469
2,000	146.99	144.252	122.039
3,000	164.809	163.198	141.578
4,000	177.741	176.455	175.106
5,000	189.002	187.843	186.65

Example 2. Let us consider the same orthotropic plate from Example 1 and direct the *x* axis across the fibers of the face. Then Young's modules along the *x* and *y* axes are $E_1 = \frac{1.4}{12} \cdot 10^5 \text{kg/cm}^2$; $E_2 = 1.4 \cdot 10^5 \text{kg/cm}^2$ respectively; Poisson's coefficients — $\nu_1 = 0.46/12$ and $\nu_2 = 0.46$; shear modulus for the main directions of elasticity $G = 1.2 \cdot 10^5 \text{kg/cm}^2$. Then, for the problem in dimensionless variables (12), we obtain $\delta = \frac{b}{a} = 1$; $c_2 = \frac{D_2}{D_1} = \frac{E_2}{E_1} = 12$; $c_3 = \frac{D_3}{D_1} = 2.481$. Let the boundary conditions (13) be fulfilled — the edges of the plate are freely pinched. As a result of numerical calculations using a computer program for solving the problem (12), (13) for this orthotropic plate, dependencies are constructed between the load *q* on the *y* axis and the critical value p_* of the load *p* on the *x* axis at fixed values of the remaining parameters of this problem. Table 2 shows the values (q, p^*) at $k = 0$.

Table 2

Dependence between *q* and p^* at $k = 0$

No.	1	2	3	4	5	6
q	0	100	200	300	400	500
p^*	254.388	241.867	227.789	208.778	166.462	77.105

It should be noted that all six points (q, p^*) correspond to the form of equilibrium, gradually transforming from the form shown in Fig. 1 *a* to the form in Fig. 1 *c*. Figure 1 illustrates the first, third and sixth eigenfunctions corresponding to the critical points (q, p^*) of Table 1. These eigenfunctions show the forms of equilibrium of the plate after loss of stability (forms of loss of stability).

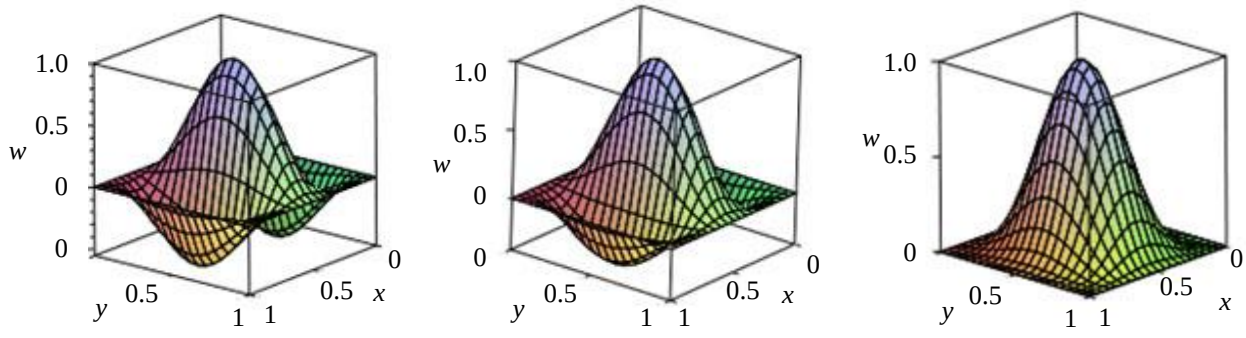

Fig. 1. Forms of plate stability loss: *a* — at *q* = 0, *p* = 254.388; *b* — at *q* = 200, *p* = 227.789; *c* — at *q* = 400, *p* = 166.462

As a result of numerical calculations using a computer program for solving the boundary value problem (16), (17) for this orthotropic plate, parameter values are found $k = 200$, $q = 0$ for which two eigenfunctions w_1 and w_2 correspond to the eigenvalue $p^* = 255.6$. This case corresponds to the loss of stability of the plate in two proper forms. Figure 2 shows graphs of the forms of stability loss corresponding to this case.

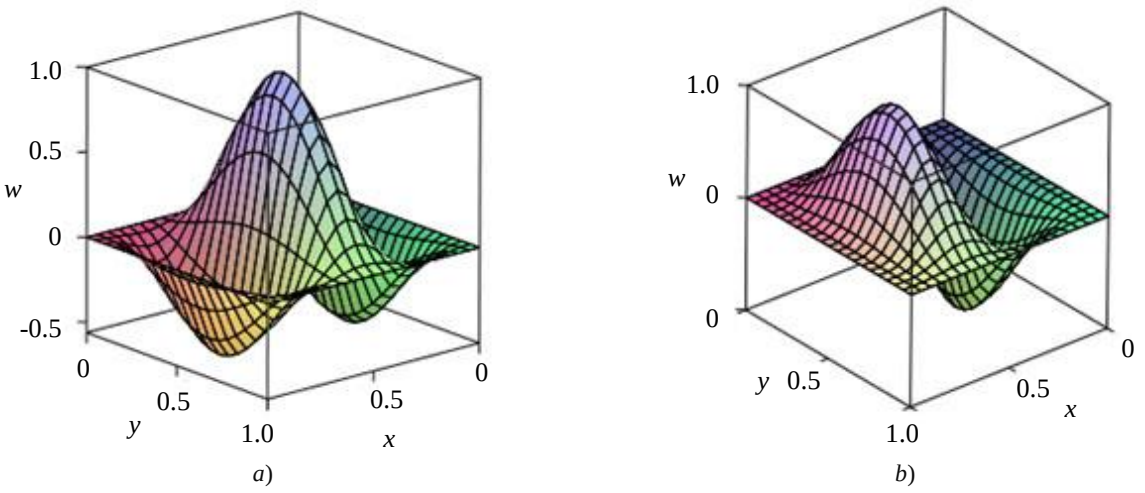

Fig. 2. Two forms of stability loss: *a* — w_1; *b* — w_2

Example 3. Let us consider an orthotropic plate with parameters $E_1 = 1.4 \cdot 10^5 \text{kg/cm}^2$, $E_2 = \frac{1.4}{12} \cdot 10^5 \text{kg/cm}^2$; Poisson coefficients — $\nu_1 = 0.46$ and $\nu_2 = 0.46/12$; shear modulus for the main directions of elasticity $G = 1.2 \cdot 10^5 \text{kg/cm}^2$. Let the length of the plate be $a = 5$, the width — $b = 1$, the edges $x = \pm\frac{a}{2}$ — are pinched, and the edges $y = \pm\frac{b}{2}$ are free, the parameter — $\delta = \frac{1}{5}$ (the plate can be considered long), modulus of subgrade reaction — $k = 350$. Numerical calculation of the solution of the problem (16) with boundary conditions (17) gives the value of the critical load $p = 37.42$, the graph of the corresponding eigenfunction is shown in Fig. 3*a*. Numerical calculation of the solution to the problem (23), (24) at $\nu_1 = 0.46$ and $k = 350$ for a beam of length $a = 5$ gives $p_0 = 39.01$, while the eigenfunction has the form shown in Fig. 3*b*. As you can see, the critical load of the plate stability loss coincides with the critical load of the beam with an error $|p - p_0| = |37.42 - 39.01| \approx 0.04$. The eigenfunctions of problems (16), (17) and (23), (24) have the same number of half-waves.

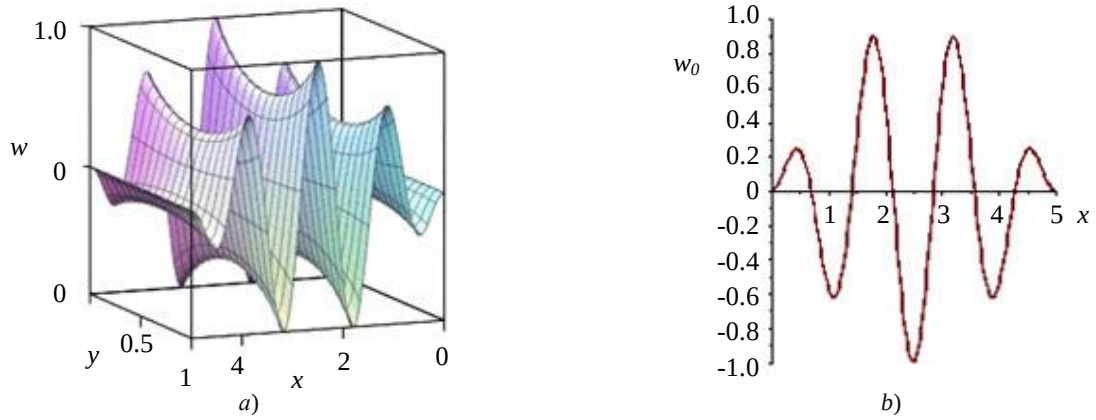

Fig. 3. Forms of stability loss: *a* — $w(x, y)$, compressed orthotropic long plate; *b* — $w_0(x)$, compressed beam

Discussion and Conclusion. The problem of critical loads of an orthotropic plate compressed in two directions lying on an elastic base is investigated. The problem is reduced to solving a parametric linear boundary value eigenvalue problem. In the case of boundary conditions of a movable hinge support, exact formulas of eigenvalues and eigenfunctions are given, and in the case of free pinching of the edges, a variational method is applied in combination

with a finite difference method and a computer program for solving the problem is constructed. The following conclusions are obtained:

1. When the compressive load component q increases along the y axis, the critical value p^* of the load compressing the plate along the x axis decreases.

2. If an orthotropic plate is compressed by a load along a direction that corresponds to greater bending stiffness, then the critical value of the loss of stability is greater than the critical value of the compressive load acting along the direction of lesser bending stiffness.

3. In the presence of an elastic base, a greater value of the modulus of subgrade reaction $k > 0$ corresponds to a greater value of the critical value of the compressive load. The presence of an elastic base increases the bearing capacity of the compressed plate.

4. In the case of a long orthotropic plate on an elastic base, the critical load of a compressed plate can be calculated approximately as the critical load of a compressed beam on an elastic base with an elastic modulus equal to the elastic modulus of the plate in the longitudinal direction.

References

1. Zubov LM. Uravneniya Karmana dlya uprugoi plastinki s dislokatsiyami i disklinatsiyami. Doklady Akademii Nauk. 2007;412:343–346. (In Russ.)

2. Zubov LM. The Linear Theory of Dislocation and Disclinations in Elastic Shells. Journal of Applied Mathematics and Mechanics. 2010;74:663–672. https://doi.org/10.1016/j.jappmathmech.2011.01.006

3. Zubov LM, Stolpovskii AV. A Theory of Dislocations and Disclinations in Elastic Plates. Journal of Applied Mathematics and Mechanics. 2008;72:996–1013.

4. Zubov LM, Fam Tan Khung. Strong Deflections of Circular Plate with Continuously Distributed Disclinations. Bulletin of Higher Education Institutes. North-Caucasian region. Natural Sciences. 2010;158:28–33.

5. Zubov LM, Fam Tan Khung. Osesimmetrichnnyi izgib nelineino uprugoi kol'tsevoi plastiki s raspredelennymi disklinatsiyami. Ecological Bulletin of Research Centers of the Black Sea Economic Cooperation. 2010;7:36–43. (In Russ.)

6. Papkov SO. Vibrations of a Rectangular Orthotropic Plate with Free Edges: Analysis and Solution of an Infinite System. Akusticheskiy zhurnal. 2015;61:152–160. https://doi.org/10.7868/S0320791915010086

7. Stolyar AM. Povedenie uzkikh panelei i sfericheskikh obolochek v usloviyakh staticheskogo i dinamicheskogo nagruzheniya. Asimptoticheskii i chislennyi analiz: monografiya. Rostov-on-Don: SFU Publ. House; 2014. 146 p. (In Russ.)

8. Finiukova VO, Stolyar AM. Asymptotic Integration of One Narrow Plate Problem. In book: Shell-like Structures. Non-Classical Theories and Applications. Advanced Structured Materials Series. Springer-Verlag: Berlin — Heidelberg. 2011;15:53–62.

9. Peshkhoev IM, Sobol BV. Buckling a Compressed Elastic Rectangular Plate with Free Edges. Problems of Strength and Plasticity. 2020;82:244–251. https://doi.org/10.32326/1814-9146-2020-82-2-244-251

10. Peshkhoev IM. Asymptotics of Critical Loads of a Compressed Narrow Elastic Plate with Internal Stresses. Problems of Strength and Plasticity. 2021;82:227–234. https://doi.org/10.32326/1814-9146-2021-83-2-227-234

11. Peshkhoev IM, Stolyar AM. Buckling of the Nonuniformly Compressed Plate with Dislocations and Disclinations. In book: Analysis of Shells, Plates, and Beams. Advanced Structured Materials Series. 2020;134:345-366. Springer, Cham. http://dx.doi.org/10.1007/978-3-030-47491-1_18

12. Belyaev AK, Morozov NF, Tovstik PE, et al. Two-Dimensional Linear Models of Multilayered Anisotropic Plates. Acta Mechanica. 2019;230:2891–2904. https://doi.org/10.1007/s00707-019-02405-y

13. Morozov NF, Tovstik PE. O formakh poteri ustoichivosti szhatoi plastiny na uprugom osnovanii. Doklady Akademii Nauk. 2012;446:37–41. (In Russ.)

14. Morozov NF, Tovstik PE, Tovstik TP. Flexural Rigidity of Multilayer Plates. Izvestiya RAN. Mechanics of Solids. 2020;5:7–12. https://doi.org/10.31857/S0572329920050128

15. Yankovskii AP. Modelling of Thermo-Elastic-Visco-Plastic Deformation of Flexible Reinforced Plates. Journal of Applied Mathematics and Mechanics. 2022;86:121–150. https://doi.org/10.31857/S003282352201009X

16. Altenbach H, Eremeyev VA. On the Effective Stiffness of Plates Made of Hyperelastic Materials with Initial Stresses. International Journal of Non-Linear Mechanics. 2010;45:976–981. https://doi.org/10.1016/j.ijnonlinmec.2010.04.007

17. Eremeev VV, Zubov LM. Buckling of a Two-Layered Circular Plate with a Prestressed Layer. Mathematics and Mechanics of Solids. 2017;22:773–781. https://doi.org/10.1177/1081286515612527

18. Altenbach H, Eremeyev VA. Bending of a Three-Layered Plate with Surface Stresses. In book: Analysis and Modelling of Advanced Structures and Smart Systems. Advanced Structured Materials Series. 2018;81:1–10. Springer: Singapore. http://dx.doi.org/10.1007/978-981-10-6895-9_1

19. Eremeev VV, Zubov LM. On Instability of Three-Layered Nonlinear Elastic Rectangular Plate with Prestressed Middle Layer. In book: Shell Structures: Theory and Applications. 2018;4:215-218. London: CRC Press, Taylor and Francis Group.

Received 01.07.2022
Revised 25.07.2022
Accepted 01.08.2022

About the Authors:

Peshkhoev, Isa M., associate professor of the Information Technologies Department, Don State Technical University (1, Gagarin sq., Rostov-on-Don, 344003, RF), Cand.Sci. (Phys.-Math.), associate professor, ORCID, peshkhoev@rambler.ru

Sobol, **Boris V.,** Head of the Information Technologies Department, Don State Technical University (1, Gagarin sq., Rostov-on-Don, 344003, RF), Dr.Sci. (Eng.), professor, ORCID, b.sobol@mail.ru

Claimed contributorship:

I. M. Peshkhoev: basic concept formulation; research objectives and tasks; computational analysis; text preparation; formulation of conclusions. B. V. Sobol: academic advising; analysis of the research results; the text revision; correction of the conclusions.

Conflict of interest statement

The authors do not have any conflict of interest.

All authors have read and approved the final manuscript.

MECHANICS

UDC 539.3

Original article

https://doi.org/10.23947/2687-1653-2022-22-3-224-231

Microhardness and Dynamic Yield Strength of Copper Samples upon Impact on a Rigid Wall

Nadezhda V. Pakhnutova[1,2] ✉, Evgeniy N. Boyangin[2], Olga A. Shkoda[2], Sergey A. Zelepugin[1,2]

[1]National Research Tomsk State University, 36, Lenin Avenue, Tomsk, Russian Federation

[2]Tomsk Scientific Center, Siberian Branch, RAS, 10/4, Akademichesky Av., Tomsk, Russian Federation

✉ nadin_04@mail.ru

Abstract

Introduction. One of the commonly used methods for assessing the dynamic characteristics of a material is the Taylor test, which establishes the relationship between the dynamic yield strength of a cylindrical sample material and its length after hitting a non-deformable barrier. The purpose of this work was to study the microhardness and determine the dynamic yield strength of copper samples for various impact velocities in the Taylor test.

Materials and Methods. Experiments were carried out with cylindrical copper (M1) samples. The throwing conditions were selected on the ballistic stand, which provided the speed of the sample in the range of 150–450 m/s at the exit from the barrel. After the impact, the microhardness of the samples in the section plane was measured. The calculation of the dynamic yield strength was carried out according to the classical Taylor formula.

Results. Experimental data are presented for cylindrical copper samples upon impact on a rigid wall with velocities in the range of 162–416 m/s, including configurations and sizes of images before and after impact. Microhardness distributions in the axial section of the samples were obtained. For each sample, the dependences of the averaged values of microhardness were constructed, which made it possible to identify four areas of deformation of the samples (the area of elastic deformations, plastic deformations, intense plastic deformations, the area of the material undergoing destruction) and determine their sizes. The dynamic yield strength of copper in the studied range of impact velocities was calculated.

Discussion and Conclusions. The values of microhardness in the entire considered region and for all studied impact velocities exceeded the initial value. There was a significant increase in the value of the dynamic yield strength compared to its static value. The correlation of the maximum averaged values of microhardness and dynamic yield strength, which grew with increasing impact velocity, was identified.

Keywords: Taylor test, copper cylinder, high-speed impact, microhardness, deformation, dynamic yield strength.

Acknowledgments. The authors would like to thank Yu. F. Khristenko, Dr.Sci (Engineering), leading researcher of the Scientific Research Institute of Applied Mathematics and Mechanics, Tomsk State University (Tomsk), for his assistance in conducting experiments. The authors express their gratitude to reviewers.

Funding information. The research is done within the frame of the government task from Tomsk Scientific Center, Siberian Branch, RAS (no. 121031800149–2).

For citation. N. V. Pakhnutova, E. N. Boyangin, O. A. Shkoda, S. A. Zelepugin. Microhardness and Dynamic Yield Strength of Copper Samples upon Impact on a Rigid Wall. Advanced Engineering Research, 2022, vol. 22, no. 3, pp. 224–231. https://doi.org/10.23947/2687-1653-2022-22-3-224-231

Introduction. The development in the scientific and technical fields related to the dynamic loading of bodies depends largely on the creation of new materials with specified properties. This was the impetus for active experimental, analytical and numerical studies related to the dynamic loading of deformable solids [1–4].

One of the commonly used methods for assessing the dynamic characteristics of a material is the Taylor test (method, task). The Taylor method establishes the relationship of the dynamic yield strength of the material of a cylindrical sample and its length after impact on a non-deformable barrier (rigid wall). This approach is often used to determine the dynamic yield strength of new materials [5–8], as well as to choose the determining ratios and select constants under the numerical modeling [9–14].

Light-gas guns (LGG) are used to accelerate bodies with a given shape. These installations make it possible to obtain a throwing speed of up to 7–9 km/s, in some experiments — up to 11 km/s, thanks to which they have been widely used in gas dynamics, ballistics, materials science, etc. The Research Institute of Applied Mathematics and Mechanics, Tomsk State University, has developed a single-stage light-gas gun [15] in which the sample is accelerated by compressed gas (helium) supplied from a balloon. It was used to conduct experiments by the Taylor method presented in this paper.

This paper is aimed at studying the microhardness and determining the dynamic yield strength of copper samples for various impact velocities in the Taylor test.

Materials and Methods. The experiment was carried out with cylindrical copper (M1) samples with a length of 34.5 mm, a diameter of 7.8 mm, and a weight of about 15 g. The composition of the sample material is indicated in Table 1.

Table 1

Composition of copper (M1)

Cu	Ag	Fe	Ni	S	As	Pb	O	Sb	Bi	Sn
> 99.9	<0.003	< 0.005	< 0.002	< 0.004	< 0.002	< 0.005	< 0.05	< 0.002	< 0.001	< 0.002

The throwing conditions were selected on the ballistic stand, which provided the speed of the sample in the range of 150–450 m/s at the exit from the barrel. The selection of conditions was required, since samples of significantly smaller mass were usually used for such experiments, which were thrown at a much higher initial velocity. By adapting the initial conditions and equipment, it was possible to provide stable throwing of the copper cylinder at a given speed. After the experiment, the samples were cut into two equal parts along the axis of symmetry using DK7732 CNC machine for electroerosion cutting.

Microhardness was measured in the section plane along the axial line of the samples on a PTM–3 hardness tester according to GOST 9650–76 by indentation of diamond tips. The measurement error of this device was 2 %. The microhardness values were also calculated according to GOST 9650–76.

The calculation of the dynamic yield strength σ was carried out according to the classical Taylor formula:

$$\sigma = \frac{\rho \upsilon^2 (L_0 - L_e)}{2(L_0 - L)\ln(\frac{L_0}{L_e})},$$

where ρ — density of the material; υ — impact velocity; L_0 — initial length; L — final length after impact; L_e — length of the elastic part of the sample. In this formula, the key indicators were the length of the elastic part of the sample and the final length of the cylinder after impact.

Research Results. *Microhardness*. Figure 1 shows cross sections of copper samples after impact at different initial velocities. For all samples, there was a region of elastic deformation with a finite diameter equal to the initial one, including for a speed of 416 m/s. The elastic region turned into a plastic one, which was accompanied by deformation, including in the radial direction, and, accordingly, an increase in the final diameter. Closer to the contact surface, a zone of intense plastic deformations that passed into the zone of destruction of the cylinder material was observed. There was also a slight asymmetry of the deformation of the samples due to the characteristic properties of throwing, which might create some difficulties for direct comparison of the results of experiments and numerical modeling when using the axis of symmetry or the plane of symmetry in the formulation of the problem.

a) *b*) *c*) *d*)

Fig. 1. Cross sections of copper samples after impact at different initial velocities:
a — 162 m/s; *b* — 225 m/s; *c* — 316 m/s; *d* — 416 m

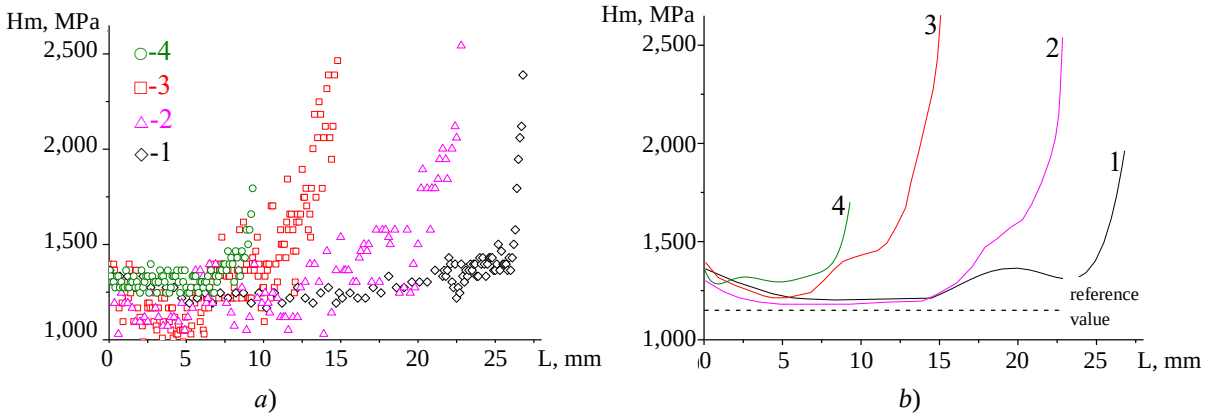

a) *b*)

Fig. 2. Distribution of values along the centerline of samples for different impact velocities
(1— 162 m/s, 2— 225 m/s, 3— 316 m/s, 4— 416 m/s): *a* — microhardness;
b — calculated averaged distribution of microhardness

In the initial state, the measured average microhardness was 1,150 ± 100 MPa. Such a spread of values, apparently, occurred due to the structural features of the material and the presence of inhomogeneities in the structure. Figure 2 *a*

shows the distribution of microhardness values along the centerline of the sample for different impact velocities, and Figure 2 *b* presents the results of averaging the obtained values.

Through comparing the average values of microhardness to the value in the nondeformable sample (1,150 MPa), we obtained that microhardness in the entire region under consideration exceeded the initial value. Several deformation zones can be distinguished. This is the rear region of the sample, where there is a slight increase in microhardness to values of 1,250–1,350 MPa, apparently associated with the effect of gas pressure during throwing. In the middle part, microhardness approaches the indicators of undeformed samples. Further, closer to the contact boundary, microhardness starts to grow to values of 1,400–1,600 MPa with an exit to the inflection point, after which there is a sharp increase in microhardness to 1,800–2,700 MPa.

The maximum microhardness is observed at an impact velocity equal to 316 m/s, while at higher speeds, a sharp decrease in the microhardness value is observed in Figure 2. The drop in microhardness in the sample for the impact velocity of 416 m/s is due to its destruction in the impact area and the loss of part of the cylinder material in the form of fragments.

Let us take a closer look at a sample with an impact velocity of 316 m/s. For this sample, two series of measurements were made along two lines, which are notionally named C and C1. The location of these lines was chosen from the following considerations. Line C was located along the axis of symmetry, and line C1 passed through the middle of the radius of the sample section. During the microhardness measurements, over 100 measurements were made along each line. This array of microhardness values was averaged, the result of averaging is shown in Figure 3.

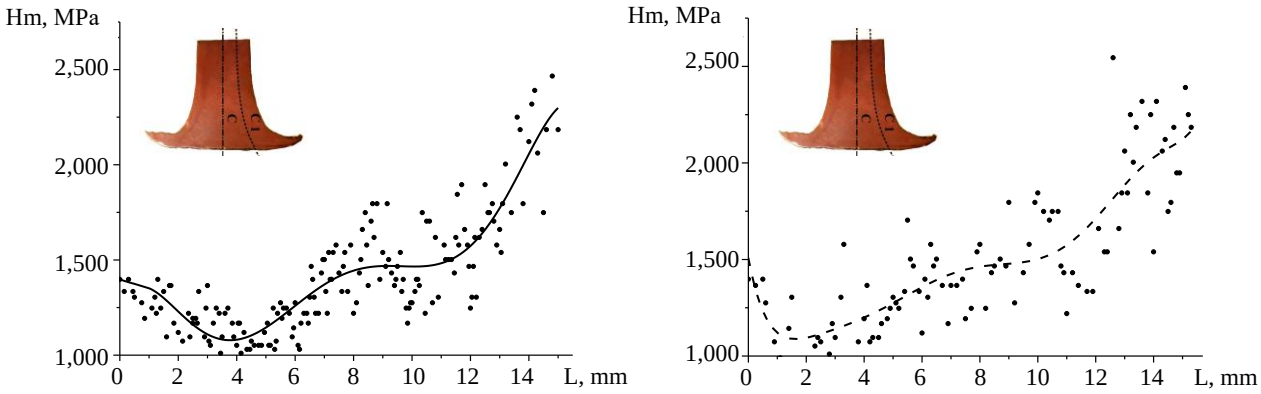

a) *b*)

Fig. 3. Averaged distribution of microhardness of a copper sample at an impact velocity of 316 m/s along the lines: *a* — C; *b* — C1

Figure 3 shows that both curves have a nonlinear character, and the distribution of microhardness in both cases is qualitatively similar and quantitatively close. Such data make it possible to identify areas of deformation of samples and determine their dimensions.

Areas of deformation of cylindrical samples. It is proposed to consider the scheme of deformation of a cylindrical sample, shown in Figure 4 and including four areas, whose size is determined based on the analysis of the distribution of microhardness.

Zone 1 corresponds to the area of elastic deformations; 2 — plastic; 3 — intense plastic deformations; 4 — the area of the material undergoing destruction. Table 1 shows the sizes of these sample areas depending on the impact velocity, where υ — impact velocity; L — final length after impact; L_e — length of the elastic deformation zone; L_p — length of

the plastic deformation zone; L_{ipf} — length of the zone of intense plastic deformations; L_f — length of the fracture zone; D_1 — diameter of the rear end of the cylinder; D_2 — diameter of the contact boundary.

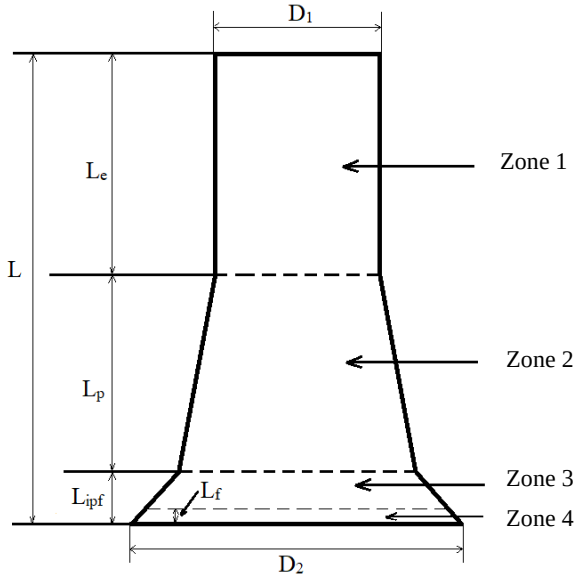

Fig. 4. Scheme of sample deformation after collision with a rigid wall

Table 2

Geometric dimensions of the deformation areas of the samples

υ, m/s	L, mm	L_e, mm	L_p, mm	L_{ipf}, mm	L_f, mm	D_1, mm	D_2, mm
0	34.5	0	0	0	0	7.8	7.8
162	26.1	12.34	10.63	3.13	0	7.8	12.7
225	22.5	9.78	9.51	3.21	0.93	7.8	15.8
316	16.1	5.87	6.83	3.4	1.14	7.9	21.4
416	9.3	3.5	1.38	4.42	2.01	7.9	31.28

The data given in Table 2 show that the sample had no material destruction zone at an impact velocity of 162 m/s. The resulting sample is an example of the classical Taylor test, which can later be used to create an adequate numerical model of the impact of a cylindrical sample on a rigid barrier, and the selection of constants of the material models. Samples at speeds of 225 m/s and 316 m/s exhibited all four zones, but compared to the sample at a speed of impact of 416 m/s, the destruction zone was small. A cylinder with an impact velocity of 416 m/s had practically no plastic deformation zone after the test. At a given impact velocity, the elastic deformation zone quickly turned into a zone of intense plastic deformations combined with a fracture zone.

Dynamic yield strength. The results of the calculation of the dynamic yield strength σ are presented in Figure 5 *a*. The speed value of 416 m/s was not taken into account, since in this case, the destruction of the cylinder was significant, which did not allow applying this calculation method. The static yield strength of M1 copper was 0.1 HPa. There was a significant increase in the value of the dynamic yield strength compared to its static value; there was also an increase in the dynamic yield strength with an increase in the impact velocity.

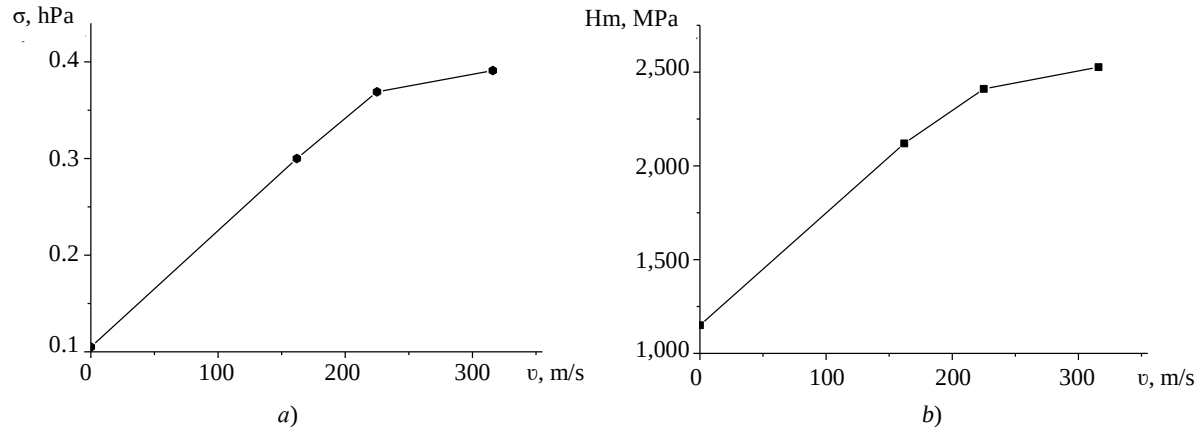

Fig. 5. Dependences on the impact velocity: *a* — dynamic yield strength; *b* — maximum microhardness

Figure 5 *b* shows the dependence of the maximum microhardness of the samples on the impact velocity. The graphs in Figure 5 *a* and 5 *b* are qualitatively similar, which implies a correlation of the dynamic yield strength and maximum microhardness, and the possibility of their mutual recalculation.

Discussion and Conclusions. The results of Taylor test experiments for cylindrical copper samples in the range of impact velocities of 162–416 m/s are presented. The data obtained has shown that after the impact of the cylinder on the rigid wall, the microhardness in the entire sample exceeded the initial value of 1,150 MPa, and in the impact area there was a significant increase in microhardness up to 1,800–2,700 MPa. The separation of the deformed cylinder into four areas was proposed: elastic deformation, plastic, intensive plastic deformation and destruction. Estimates of the sizes of these areas for the studied impact velocities were given. According to the classical Taylor formula, the dynamic yield strength was calculated, which significantly exceeded the static yield strength and grew with increasing impact velocity. The dependences of the dynamic yield strength and the maximum averaged value of microhardness on the impact velocity of the sample on a nondeformable barrier were shown. The correlation of the maximum averaged values of microhardness and dynamic yield strength, which increased with growing impact velocity, was specified. The presented data can be of value for assessing the adequacy of the physicomathematical model used for numerical calculation of problems of high-speed deformation of metals and alloys.

References

1. Lapshin VL, Zenkov EV. Control Algorithm for an Elastic-Viscoplastic Model to Study Processes of Shock Interaction of Bodies. Advanced Engineering Research. 2021;21:191–199. https://doi.org/10.23947/2687-1653-2021-21-2-191-199

2. Sungbo Lee, Kwanghyun Yu, Hoon Huh, et al. Dynamic Hardening of AISI 304 Steel at a Wide Range of Strain Rates and Its Application to Shot Peening Simulation. Metals. 2022;12:403. https://doi.org/10.3390/met12030403

3. Rodionov ES, Lupanov VG, Taylor NA, et al. Impact Tests with Copper Cylinders: Experiments, Microstructural Analysis and 3D SPH Modeling with Dislocation Plasticity and MD-Informed Artificial Neural Network as Equation of State. Metals. 2022;12:264. https://doi.org/10.3390/met12020264

4. Bin Jia, Alexis Rusinek, Xinke Xiao, et al. Simple Shear Behavior of 2024-T351 Aluminum Alloy over a Wide Range of Strain Rates and Temperatures: Experiments and Constitutive Modeling. International Journal of Impact Engineering. 2021;156:103972. https://doi.org/10.1016/J.IJIMPENG.2021.103972

5. Chong Gao, Takeshi Iwamoto. Instrumented Taylor Impact Test for Measuring Stress-Strain Curve through Single Trial. International Journal of Impact Engineering. 2021;157:103980. https://doi.org/10.1016/J.IJIMPENG.2021.103980

6. Jun-Cheng Li, Gang Chen, Feng-Lei Huang, et al. Load Characteristics in Taylor Impact Test on Projectiles with Various Nose Shapes. 2021;11:713. https://doi.org/10.3390/met11050713

7. Li Juncheng, Chen Gang, Lu Yonggang, et al. Investigation on the Application of Taylor Impact Test to High-G Loading. Frontiers in Materials. 2021;8:717122. 10.3389/fmats.2021.717122

8. Subhajit Sen, Biswanath Banerjee, Amit Shaw. Taylor Impact Test Revisited: Determination of Plasticity Parameters for Metals at High Strain Rate. International Journal of Solids and Structures. 2020;193–194:357–374. https://doi.org/10.1016/j.ijsolstr.2020.02.020

9. Kiselev AB, Serezhkin AA. The Distinctive Features of the Collision between an Elastoplastic Cylinder and a Non-deformable Obstacle. Journal of Applied Mathematics and Mechanics. 2015;79:571–583. https://doi.org/10.1016/j.jappmathmech.2016.01.011

10. Bayandin YuV, Bilalov DA, Uvarov SV. Verification of Wide-Range Constitutive Relations for Elastic-Viscoplastic Materials Using Taylor-Hopkinson Test. Computational Continuum Mechanics. 2020;13:449–458.

11. Yanov DV, Bodrov AS, Pakhnutova NV, et al. Simulation of Dynamic Channel-Angular Pressing of Copper Samples with Allowance for Experimental Data of Loading. Tomsk State University Journal of Mathematics and Mechanics. 2019;60:141–151. https://doi.org/10.17223/19988621/60/11

12. Bodrov AS, Olimpieva NV, Zelepugin AS, et al. Numerical Simulation of Dynamic Channel-Angular Pressing of Titanium Specimens. Tomsk State University Journal of Mathematics and Mechanics. 2015;37:56–63. http://dx.doi.org/10.17223/19988621/37/5

13. Zelepugin SA, Zelepugin AS, Bodrov AS, et al. Trekhmernoe modelirovanie protsessov plasticheskogo deformirovaniya metallicheskikh obraztsov pri dinamicheskom kanal'no-uglovom pressovanii. Russian Physics Journal. 2013;56:50–52. (In Russ.)

14. Armstrong RW. Constitutive Relations for Slip and Twinning in High Rate Deformations: A Review and Update. Journal of Applied Physics. 2021;130:245103. https://doi.org/10.1063/5.0075916

15. Khristenko YF, Zelepugin SA, Gerasimov AV. New Light-Gas Guns for the High-Velocity Throwing of Mechanical Particles. ARPN Journal of Engineering and Applied Sciences. 2017;12:6606–6610.

Received 13.06.2022
Revised 30.06.2022
Accepted 14.07.2022

About the Authors:

Pakhnutova, **Nadezhda V.,** post-graduate student of the Solids Mechanics Department, National Research Tomsk State University (36, Lenin Avenue, Tomsk, 634050, RF), junior researcher of the Research Department for Structural Macrokinetics, Tomsk Scientific Center, Siberian Branch, RAS (10/4, Akademichesky Av., Tomsk, 634055, RF), ScopusID, ORCID, nadin_04@mail.ru

Boyangin, Evgeniy N., leading engineer of the Research Department for Structural Macrokinetics, Tomsk Scientific Center, Siberian Branch, RAS, 10/4, Akademichesky Av., Tomsk, 634055, RF), Cand.Sci. (Eng.), ScopusID, ORCID, jeck2000@list.ru

Shkoda, Olga A., senior research worker of the Research Department for Structural Macrokinetics, Tomsk Scientific Center, Siberian Branch, RAS (10/4, Akademichesky Av., Tomsk, 634055, RF), Cand.Sci. (Eng.), ScopusID, ORCID, O.Shkoda@dsm.tsc.ru

Zelepugin, Sergey A., leading researcher, Head of the Research Department for Structural Macrokinetics, Tomsk Scientific Center, Siberian Branch, RAS (10/4, Akademichesky Av., Tomsk, 634055, RF), professor of the Solids Mechanics Department, National Research Tomsk State University (36, Lenin Avenue, Tomsk, 634050, RF), Dr.Sci. (Phys.-Math.), senior research fellow, ScopusID, ORCID, szel@yandex.ru

Claimed contributorship:

N. V. Pakhnutova: participation in experimental research; processing of the results obtained; writing a draft of the article; formulation of preliminary conclusions. E. N. Boyangin: photographing samples; measuring the microhardness of samples; processing the results obtained. O. A. Shkoda: microhardness measurement; processing the results obtained. S. A. Zelepugin: research objectives and tasks setting; organization and conduct of experimental work; editing of the text and conclusions.

Conflict of interest statement

The authors do not have any conflict of interest.

All authors have read and approved the final manuscript.

MACHINE BUILDING AND MACHINE SCIENCE

UDC 621.791
https://doi.org/10.23947/2687-1653-2022-22-3-232-241

Original article

Increasing the Durability of Butt-Welded Joints Operating under Cyclic Loads in a Biaxial Stress Field

Yury G. Lyudmirsky[1], **Valery P. Leonov**[2], **Semyon S. Assaulenko**[1] ✉

[1] Don State Technical University, 1, Gagarin sq., Rostov-on-Don, Russian Federation

[2] Central Research Institute of Structural Materials "Prometey" named after I. V. Gorynin of National Research Center "Kurchatov Institute", 49, Shpalernaya St., Petersburg, Russian Federation

✉ assaulenko_s@mail.ru

Abstract

Introduction. In sheet and hull structures operating under pressure, destruction, as a rule, is localized along the transition line from the base metal to the weld metal. Methods of increasing the durability of butt-welded joints, which are aimed at reducing stress concentration and creating favorable residual compression stresses, are described.

Materials and Methods. The tests were carried out on an installation for biaxial bending, which created a biaxial stress field. Factory-made coupons and samples with an additionally processed transition zone from the weld metal to the base metal were tested. The effectiveness of further processing is shown by the following methods:

– abrading;
– grit hardening;
– abrading with grit hardening;
– melting of the fusion line in argon without filler wire;
– melting of the fusion line in argon with filler wire EP-410U;
– melting of the fusion line without filler wire with plastic deformation between narrow rollers.

Results. The origin, development of destruction, and its features were analyzed using different methods of further processing of joint welds. Confidence spans (95 %) of the origin and development of failures for joint welds and base metal were calculated. The efficiency of the proposed methods for further processing was evaluated.

Discussion and Conclusions. An analysis of the effectiveness of methods for increasing the durability of butt-welded joints has shown that the creation of a smooth transition from the weld metal to the base metal reduces significantly the stress concentration. This provides increasing the number of cycles before the onset of destruction and the survivability of compounds. Due to compressive stresses in the near-weld area, it is possible to increase the durability of joint welds. The most effective methods of further processing of welds combine the reduction of stress concentration and the creation of residual compression stresses. The high-tech solution is remelting the transition zone in an argon medium with an additional EP-410U filler wire.

Keywords: durability increase, cyclic loads, butt joints, stress concentration, residual stresses, origin and development of fracture.

Acknowledgements. The authors are deeply grateful to V. F. Lukyanov, Dr.Sci. (Engineering), professor, Head of the Machines and Welding Fabrication Automation Department, for years of joint work and academic advising.

For citation. Y. G. Lyudmirsky, V. P. Leonov, S. S. Assaulenko. Increasing the Durability of Butt-Welded Joints Operating under Cyclic Loads in a Biaxial Stress Field. Advanced Engineering Research, 2022, vol. 22, no. 3, pp. 232–241. https://doi.org/10.23947/2687-1653-2022-22-3-232-241

Introduction. Welded hull and shell structures operating under pressure are widely used in shipbuilding, chemical, power engineering and other industries. Reducing the metal consumption of such structures while increasing their efficiency is a critical task [1–4]. To reduce the weight of structures, it is required to use stronger materials under stresses close to the yield point. In this case, special requirements are put forward for the implementation of welded structures to ensure high structural strength. In other words, it is required to develop measures that increase the durability of structures to values close to the indicators of the base metal.

The work is aimed at studying the possibilities of increasing the durability of welded joints operating under cyclic loads in a corrosive environment (3 % *NaCl* solution), with the help of additional processing of joints.

Materials and Methods. Butt-welded joints were made of chromium-nickel-molybdenum steel. Preliminary heat treatment of sheet material provided yield limits of 900 MPa; 1,100 MPa; 1,150 MPa. The tests [5, 6] were carried out with a biaxial stress field and simultaneous action of repeated static loads in a corrosive environment (3 % *NaCl* solution). Manual multi-pass welding was performed with low-alloy electrodes 48H 11, 48H13, and austenitic electrodes EA 981/15. The failure nucleated from the stretched fibers, so the stress state was studied on the stretched surface of the sample. The stresses were determined by calculation. They were measured with a lever Huggenberger tensometer and tensoresistors with a base of 5 mm at a distance of 10 mm from the weld. If the measured stress values differed from the calculated values by more than 5 %, the pressure under the sample was corrected.

The failure of welded joints was localized along the transition line from the base metal to the weld metal, as shown in Figure 1.

Fig. 1. Fracture pattern of the butt-welded joint (photo of the authors)

The main reasons for the decrease in the working capacity of welded joints compared to sheet metal [7–11]:

– geometric stress concentration;

– residual welding stresses;

– deterioration of the structure and properties of the base metal in the near-weld area under the influence of the thermal welding cycle.

The influence of each of these factors can be partially or completely neutralized.

At the Department of "Machines and Automation of Welding Production", DSTU, butt-welded joints of high strength steels have been tested by various post-treatment methods for many years (Table 1). The experiments corresponded to the loading conditions of real structures.

Table 1

Techniques of additional treatments of butt-welded joints in the transition zone from the joint to the base metal

No	Treatment
1	Cleaning with an abrasive wheel with a grain size of 80. Fillet radius R = 30–40 mm
2	Grit hardening with AD-1 shot blaster with DSL–1.5cast steel shot. Pressure is 5 atm, head travel speed is 75 mm/min. Processing zone at the transition point from joint to metal is 15–30 mm
3	Cleaning the weld metal – base metal transition zone with an abrasive wheel by the first method, and grit hardening – by the second method
4	Washing in argon medium without filler wire. Diameter of the tungsten electrode – 3 mm, current I = 120 A, arc voltage U = 10–12 B, welding speed is 8 m/h, transverse vibration frequency – 60 min^{-1}, vibration amplitude – 6 mm
5	Washing with EP–410U filler wire by the fourth method. Filler wire diameter is 1.6 mm
6	Washing without filler wire by the fourth method. Plastic deformation between the beads. Bead diameter – 120 mm, width – 20 mm. Bead pressure – 18,000 kgf, rolling speed – 1.4 m/min.

Physical and metallurgical processes occurring under welding cannot be modeled in full. Therefore, the tests were carried out on full-scale butt-welded joints with full preservation of the factory welding technology and geometric parameters of the joints. Low-cycle fatigue of welded joints was studied on samples in the form of disks with a diameter of 550 mm and a thickness of 30 mm on UDI–550 installation [12]. They were pivotally fixed along the contour and loaded with hydrostatic oil pressure. Under the action of hydrostatic pressure, the disk was axially bent. Compression stresses appeared on the inner surface, tensile stresses appeared on the outer surface, and a corrosive medium, a 3 % aqueous solution of sodium chloride, affected it. The samples were tested under repeated static loading with a frequency of 10 cycles/min.

The maximum stresses occurred in the central part of the samples. On a large surface, the statistical probability of the occurrence and development of failure is higher, which in general brings the test conditions closer to the real working conditions of the loaded hull structures.

Research Results. Table 2 shows the test results of samples after additional processing of welded joints under cyclic loading.

Table 2

Influence of additional methods of processing butt-welded joints on performance characteristics

No.	Yield strength, MPa	Welding materials	Type of joint processing	Max cycle voltage, MPa	Additional processing	Number of cycles before		Breaking point
						appearance of cracks, N_T	loss of tightness, Np	
1	1,100	EA 981/15	1st method: abrading	700	No	2,600	20,560	Transition line*
2						3,890	24,401	
3					Yes	10,840	27,237	
4						9,115	28,947	
5	1,100	48H13	2nd method: grit hardening	860	No	2,000	7,430	Transition line
6						2,100	11,500	
7					Yes	1,410	27,349	Transition line

No.	Yield strength, MPa	Welding materials	Type of joint processing	Max cycle voltage, MPa	Additional processing	Number of cycles before		Breaking point
						appearance of cracks, N_T	loss of tightness, N_p	
8						2,000	14,051	
9	1,100	48H13	3rd method: abrading and grit hardening	700	Yes	10,670	32,310	Transition line with access to the base metal
10						12,430	37,540	
11	1,100	EA 981/15		720	Yes	10,870	32,840	
12						9,300	34,460	
13	1,100	48H13	4th method: washing in argon without filler wire	700	No	3,800	24,930	Transition line with access to the base metal
14						2,680	21,980	
15					Yes	6,240	33,287	
16						6,450	29,714	
17		EA 981/15			Yes	8,320	25,400	
18						7,000	24,250	
19	900	48H11	5th method: surfacing of fillet bead with EP410U wire	605	No	4,300	29,074	Transition line
20						4,200	23,079	
21					Yes	25,600	100,000	Base metal and perpendicular to the weld
22						29,800	58,384	
23						30,910	91,300	
24						24,100	86,000	
25	1,150	48H11	5th method	720	No	3,386	22,639	Transition line
26						2,566	22,433	
27					Yes	7,627	39,457	Transition line and base metal
28						4,890	33,405	
29	1,150	48H13	5th method	760	No	3,890	24,401	Transition line
30						3,285	23,245	
31					Yes	8,500	36,400	Transition line and base metal
32						9,886	34,636	
33	900	48H13	Washing of fusion line + 6th method: weld rolling between narrow beads	605	No	3,270	21,980	Transition line
34						1,300	26,074	
35						1,200	19,079	
36						3,160	26,880	
37					Yes	20,860	48,210	Base metal and cracks across the weld
38						19,321	139,300	
39						17,300	93,552	
40						24,475	99,910	
41		ЭА981/15		720	No	3,386	22,630	Transition line
42						2,566	22,433	
43					Yes	31,950	96,875	Base metal and cracks across the weld
44						23,450	78,543	
45	1150	48H13		760	No	3,285	23,245	Transition line
46					Yes	22,900	87,280	Base metal and cracks across the weld
47						21,168	55,039	

*from weld to base metal.

Additional processing of welded joints by the 1st and 4th method (Table 1) reduced the stress concentration through increasing the interface radius of the weld metal and the base metal.

The 2nd method created small compressive stresses in the weld area, but practically did not change their concentration. An alternative to the proposed method is rolling the transition zone, presented in [13].

The third, fifth and sixth methods, in addition to reducing the stress concentration, made it possible to obtain favorable residual compression stresses in the transition zone from the weld metal to the base metal.

Figure 2 *a* shows the confidence intervals (95 %) of the failure initiation, and Figure 2 *b* — intervals before failure for welded joints (dotted lines) made according to the factory technology, and for the base metal (solid lines). The intervals were plotted according to the data from Table 2.

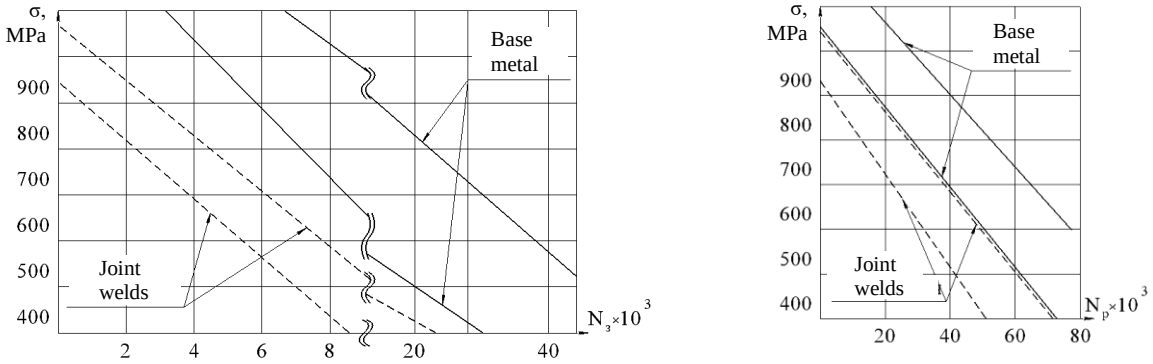

a) *b*)

Fig. 2. Comparison of the operability of the base metal and butt-welded joints under repeated static loading:
a — number of cycles before appearance of cracks; *b* — number of cycles before failure

The spread of values of resistance to damage and durability of butt-welded joints (Fig. 2 *a*) and the base metal (Fig. 2 *b*) depending on the maximum stresses at zero pulsating loading cycle are presented.

It can be seen that the resistance to the failure nucleation $N_э$ and the durability of butt-welded joints before failure N_p (in this case, before the loss of tightness) is much less than that of the base metal.

To determine the compressive stresses generated in the joints as a result of processing, residual stresses were measured. This method is described in [14, 15].

Table 3 presents the results of measurements of residual stresses in the direction perpendicular to the axis of the weld on the surface of the welded joints in the near-weld zone.

Table 3

Residual compression stresses in the interface zone of weld metal and base metal,
depending on the additional processing methods

Method of additional processing of the weld	Compressive stresses, MPa
2nd and 3rd	60–80
5th	240–320
6th	700–800

According to Table 2 and Figure 3, it is possible to judge the effectiveness of various methods of additional processing of welded joints operating under cyclic loading.

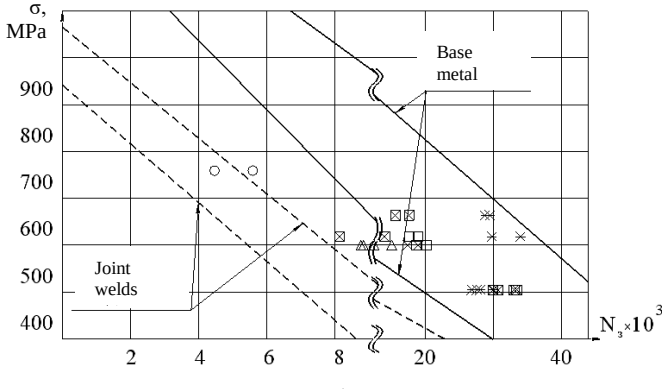

a)

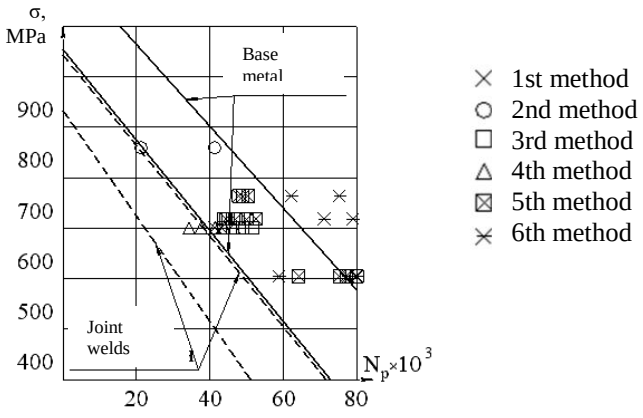

b)

Fig. 3. Efficiency of methods of additional processing of the weld metal – base metal interface zone: *a* — number of cycles before cracks appear; *b* — number of cycles before failure

Figure 3 shows the results of testing samples of butt-welded joints processed in different ways. Figure 3 *a* shows the confidence areas of the spread of values before the initiation of the destruction of the base metal and butt-welded joints without additional processing. Figure 3 *b* shows the same areas before the destruction of the samples (before loss of tightness).

Dressing the weld metal — base metal transition zone increased the resistance to the fracture nucleation due to a decrease in the concentration of stresses (Table 2). However, this method did not practically affect the fracture geometry. Cracks nucleated and developed along the interface line of the weld metal and the base metal.

Samples had a similar fracture pattern, in which the fusion line of the weld and base metal was washed by an arc in argon without a filler metal (4th method). This caused a decrease in stress concentration. As a result, the resistance to the failure nucleation increased. At the same time, the resistance to the development of fracture did not practically change (Fig. 3). The 4th method is more technologically advanced compared to the 1st one, since it does not require additional equipment other than welding.

Grit-hardening (2nd method) did not practically affect the damage resistance, determined by the number of cycles before the appearance of a visible crack — N_T, but increased the survivability — the number of cycles that the sample withstood after the formation of the first crack until it lost its bearing capacity (leak). This is due to the fact that grit-hardening does not guarantee uniformity of the surface deformation of the metal, specifically, at the junctions with undercuts, surges, craters, and non-melting outlines of the weld. It is here that failure starts. However, in places of smooth coupling of the weld metal and base metal, shot blasting, which caused the greatest compression stresses, prevented the formation of an extended main crack, which increased the resistance to the development of destruction.

To increase the efficiency of the grit-hardening, the 3rd method was proposed. Abrading was performed by the 1st method, and then shot blasting followed. In comparison to the 2nd method, the durability of the samples increased by about 20 % before the onset of fracture and before the loss of tightness. Comparison of the 1st and 3rd methods showed that the number of cycles before the fracture nucleation did not actually change, but the number of cycles before fracture (loss of tightness) increased by 20 %.

The 5th method [16] was washing with an EP–410U filler wire with a diameter of 1.6 mm. When cooled (140 °C and below), the fillet beads underwent martensitic transformations. When cooled to room temperature, the volume increased by 1.5 % in total [11]. As it was shown earlier, this causes the appearance of residual compression stresses up to 300 MPa. Fillet beads with an increased specific volume contributed to an increase in damage resistance and the development of failure, i.e., an increase in survivability. In such joints, the first cracks appeared either on the base metal, away from the weld, or simultaneously along the transition line from the weld to the base metal (Table 2). Cracks found on the fusion line, as a rule, developed at a low rate, failure was caused by crack coalescence in the base metal and in the welded joint. The typical appearance of the welded joints, additionally processed by the 5th method, after the test is shown in Figure 4.

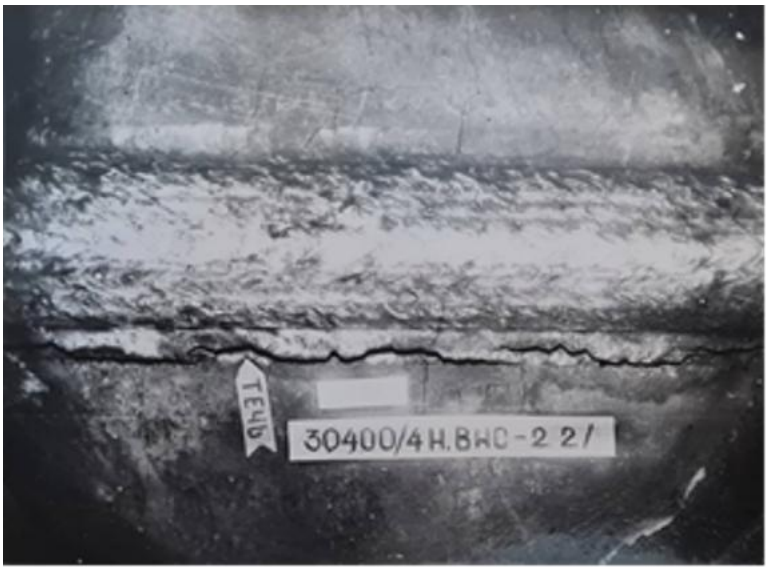

Fig. 4. Destruction of a butt-welded joint made by the 5th method (photo of the authors)

The considered type of treatment reduces the stress concentration along the entire length of the weld and creates favorable residual compression stresses in the area of the fillet beads with an increased specific volume.

The action of compressive stresses inhibits the fracture nucleation. With the development of cracks along the fillet bead, the action of transverse compressive stresses is no longer effective and is partly eliminated. This can explain the absence of the influence of beads of increased specific volume on the survivability of welded joints. If the failure nucleates not on the fillet bead, but on the base metal, the survivability of welded joints increases.

Treatment of the transition zone from the base metal to the weld metal by the 5th method increased the resistance to failure nucleation and development approximately 3–4 times. At the same time, the topography of the failure changed markedly. The first cracks, as a rule, originated in the base metal (Fig. 4). In the presence of poorly welded craters on the front surface of the weld, cracks initiated in these places and developed mainly perpendicular to the weld, but even in this case, the resistance to the failure nucleation and development remained quite high (Table 2, 5th method).

Surface plastic deformation of the near-weld zone [12] in butt joints by rolling with narrow beads (6th method) made it possible to bring the resistance to nucleation and development of failure to the level of similar characteristics of the base metal. This conclusion was confirmed by the fracture pattern of welded joints made by the 6th method (Fig. 5).

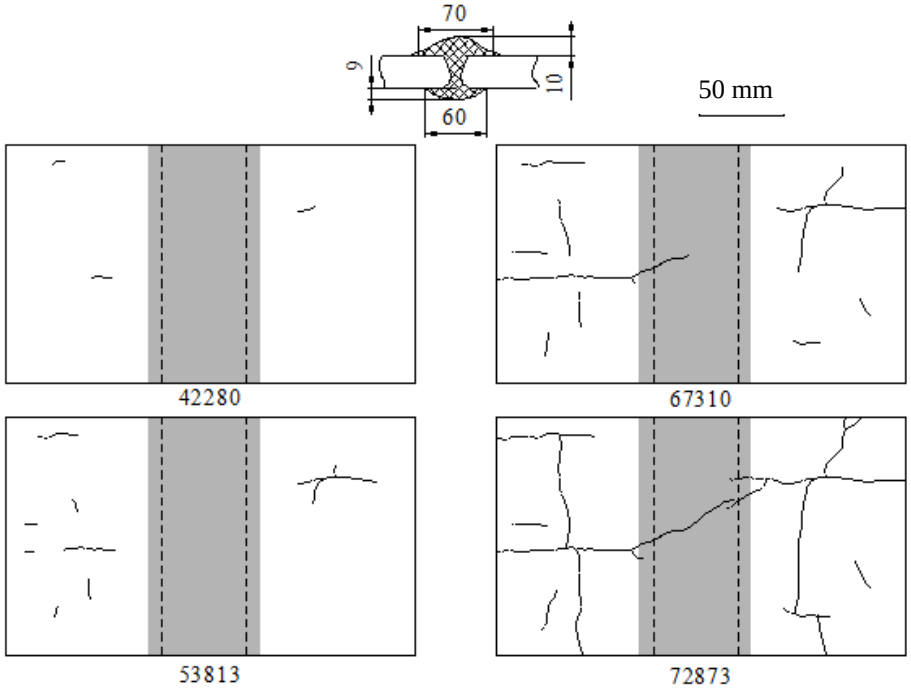

a)

b)

Fig. 5. Fracture nucleation and development pattern of the welded joint,
whose interface zone was run between narrow beads (6th method):
a — record of the sample fracture development; *b* — appearance of the welded joint during fracture (photo of the authors)

It can be seen that the fracture nucleated and developed according to the basic method (Fig. 5 *a*, Table 2, and the fracture pattern of the joints, shown in Fig. 5 *b*). The washing of the fusion line and its subsequent running between the narrow beads (6th method) increased the resistance to the fracture nucleation by about eight times, the survivability of welded joints — by about four times.

Discussion and Conclusions

1. As initial samples, we considered welded joints made according to the factory technology without additional processing of the transition zone. In this case, during cyclic loading along the transition line from the weld metal to the base metal, multistage nucleation of fatigue cracks was observed. They developed rapidly and were combined into one mainline. Then, it developed in depth, which caused loss of tightness. The durability of welded joints turned out to be 2–3 times less than that of the base metal.

2. Two types of additional processing were involved:

– abrading of the transition zone from the weld to the base metal (1st method);

– remelting of the transition zone from the weld to the base metal with a non-melting electrode, an arc burning in an argon medium (4th method).

This made it possible to increase the resistance to the fracture nucleation by almost 2 times. The survivability of these welded joints did not change much.

3. Grit hardening (2nd method) did not practically affect the number of cycles before the fracture nucleation, but slightly increased the number of cycles before fracture.

4. Preliminary abrading of the weld metal – base metal transition zone and subsequent grit hardening (3rd method) increased the resistance of welded joints to the fracture nucleation and development by almost 1.5 times.

5. When the fillet bead was surfaced with a material with suitable volumetric changes (5th method), cracks occurred in the transition zone and in the base metal. At the same time, the resistance to the fracture nucleation and development increased approximately 3–4 times.

6. Washing without filler wire (4th method) and plastic deformation between narrow beads (6th method) provided an increase in the resistance to fracture and survivability of welded joints almost to the level of similar characteristics of the base metal.

References

1. Vinokurov VA, Kurkin SA, Nikolaev GA. Svarnye konstruktsii. Mekhanika razrusheniya i kriterii rabotosposobnosti. BE Paton (ed.) Moscow: Mashinostroenie; 1996. 576 p. (In Russ.)

2. Leonov VP, Malyshevskii VA. Structural and Technological Strength of Steel for Marine Structures. Metal Science and Heat Treatment. 2001;43:444.

3. Ilyin AV, Leonov VP, Filin VYu. Opredelenie parametra treshchinostoikosti CTOD dlya metalla svarnykh soedinenii sudokorpusnykh stalei pri nizkikh klimaticheskikh temperaturakh. Research Bulletin by Russian Maritime Register of Shipping. 2009;32:120–146. (In Russ.)

4. Fetisova EA, Lupachev AG. Peculiarities of Diffusion Processes in Dissimilar Steels Welded Joints. Vestnik of Belarusian-Russian University.2014;3:79–87. https://doi.org/10.53078/20778481_2014_3_79

5. Ilyin AV, Filin VYu. On the Problem of Quantitative Service Life Assessment for High-Strength Steel Welded Structures under the Effect of Corrosion Medium. Procedia Structural Integrity. 2019;14:964–977. https://doi.org/10.1016/j.prostr.2019.07.078

6. Kazuo Tateishi, Takeshi Hanji. Low Cycle Fatigue Strength of Butt-Welded Steel Joint by Means of New Testing System with Image Technique. International Journal of Fatigue. 2004;26:1349–1356. https://doi.org/10.1016/j.ijfatigue.2004.03.016

7. Peredelsky VA, Harchenko VY, Chernogorov AI, et al. On Detection of Crack-Like Welding Defects by Existing Quality Control Methods. Advanced Engineering Research. 2021;21(1):89–95. https://doi.org/10.23947/2687-1653-2021-21-1-89-95.

8. Bychenok VA, Berkutov IV, Mayorov AL, et al. Residual Stress Control in the near Seam Zone of the Welding Joint. Tekhnologiya Mashinostroeniya. 2019;12:45–50.

9. Leonov VP, Schastlivaya IA, Igolkina TN, et al. Application of Finite Element Method for Simulation of Stress-Strain State in Manufacturing of Long Turbine Blades Made of High-Strength Titanium Alloys. Inorganic Materials: Applied Research. 2014;5:578–586. https://doi.org/10.1134/S2075113314060069

10. Zerbst U, Hensel J. Application of Fracture Mechanics to Weld Fatigue. International Journal of Fatigue. 2020;139:105801. https://doi.org/10.1016/j.ijfatigue.2020.105801

11. Jong-Hyun Baek, Yun-Chan Jang, Ik-Joong Kim, et al. Influence of Weld Joint Geometry and Strength Mismatch on Load Bearing Capacity of API Pipeline. International Journal of Pressure Vessels and Piping. 2022;199:104737. https://doi.org/10.1016/j.ijpvp.2022.104737

12. Ilyin AV, Sadkin KE. Assessment of Structural and Technological Stress Concentration in Welded Joints for Fatigue Strength Estimation of Hull Structures. Materials Science Issues. 2012;2:161–176.

13. Lyudmirskii YG, Assaulenko SS, Ageev SO. Constructive and Technological Method of Increasing Durability of "Choke Connections". Journal of Physics Conference Series. 2021;2131:042061. https://doi.org/10.1088/1742-6596/2131/4/042061

14. Franks J, Wheatley G, Zamani P, et al. Fatigue Life Improvement Using Low Transformation Temperature Weld Material with Measurement of Residual Stress. International Journal of Fatigue. 2022;164:107137. https://doi.org/10.1016/j.ijfatigue.2022.107137

15. Ritsu Nishimura, Ninshu Ma, Yong Liu, et al. Measurement and Analysis of Welding Deformation and Residual Stress in CMT Welded Lap Joints of 1180 MPa Steel Sheets. Journal of Manufacturing Processes. 2021;72:515–528. https://doi.org/10.1016/j.jmapro.2021.10.050

16. Xiaohui Zhao, Yanjun Fan, Yu Liu, et al. Evaluation of Fatigue Fracture Mechanism in a Flash Butt Welding Joint of a U75V Type Steel for Railroad Applications. Engineering Failure Analysis. 2015;55:26–38. https://doi.org/10.1016/j.engfailanal.2015.05.001

Received 08.08.2022
Revised 29.08.2022
Accepted 07.09.2022

About the Authors:

Lyudmirsky, Yury G., professor of the Machines and Automation of Welding Production Department, Don State Technical University (1, Gagarin sq., Rostov-on-Don, 344003, RF), Dr.Sci. (Eng.), professor, ScopusID, ORCID, lyudmirskiy40@mail.ru

Leonov, Valery P., Deputy director general, Central Research Institute of Structural Materials "Prometey" named after I.V. Gorynin of National Research Center "Kurchatov Institute" (49, Shpalernaya St., Petersburg, 191015, RF), Dr.Sci. (Eng.), ScopusID, ORCID, leonov_vp@spbstu.ru

Assaulenko, Semyon S., senior lecturer of the Machines and Automation of Welding Production Department, Don State Technical University (1, Gagarin sq., Rostov-on-Don, 344003, RF), ScopusID, ORCID, assaulenko_s@mail.ru

Claimed contributorship:

Yu. G. Lyudmirsky: academic advising; the text revision; formulation of conclusions. V. P. Leonov: analysis of the research results; correction of the conclusions. S. S. Assaulenko: basic concept formulation; research objectives and tasks; computational analysis; text preparation.

Conflict of interest statement

The authors do not have any conflict of interest.

All authors have read and approved the final manuscript.

MACHINE BUILDING AND MACHINE SCIENCE

UDC 620.179.18
https://doi.org/10.23947/2687-1653-2022-22-3-242-251

Original article

Study of Tapered Threads Parameters Affecting the Quality of the Oil Pipeline Connection

Irina K. Tsybrii[1] ✉, **Nikolai S. Koval**[1], **Zhanibek N. Issabekov**[2]
[1] Don State Technical University, 1, Gagarin sq., Rostov-on-Don, Russian Federation
[2] Satbayev University, 22, Satbaev St., Almaty, Republic of Kazakhstan
✉ irconst@mail.ru

Abstract

Introduction. With the growth in the production and transportation of gas and oil, the urgency of the problem of tightness of the connection of pipes of the oil and gas range increases. The most common are coupling and streamline threaded connections. Threads of the buttress type, conical trapezoidal, and triangular threads are used. The tightness of the connection depends directly on their quality. The production of pipes and couplings is influenced by many factors. Examples include technological heredity, rigidity of technological equipment, its setting and resetting. The required connection quality is provided by the quality of the elements. The assembly should take into account the possibility of complete interchangeability. The second recommended option is a group assembling. In all cases, control operations are mandatory. The paper presents the results of studies on the distribution of pipe and coupling thread quality parameters in the batch.

Materials and Methods. Fragments (tubular parts) of casing pipes with trapezoidal thread and increased tightness (CPTT) and with trapezoidal thread of the buttress profile were studied. They were randomly selected from different batches. When measuring, the samples were fixed in the chuck of 1I611P lathe. The measuring instrument was a clock type 0 accuracy class indicator with a stand. Generally accepted statistical methods were used to evaluate the data obtained.

Results. The experiments have found how the tightness of the connection through the method of complete interchangeability is affected by the radial runout of the surfaces of the thread profile tops, the pipe chamfers, and the sealing belt.

Discussion and Conclusions. Significant deviations of the values of the thread parameters from the permissible ones were found, which might cause a leak in the connection. Obtaining a high-quality and reliable connection is possible when assembling by the method of incomplete or group interchangeability.

Keywords: OCTG connection, connection quality, quality control, buttress connection, CPTT connection, radial runout of buttress thread surfaces, radial runout of CPTT thread surfaces.

Acknowledgements. The authors express their gratitude to reviewers, whose critical assessment of the materials and suggestions for their improvement contributed to a significant improvement in the quality of the article.

For citation. I. K. Tsybrii, N. S. Koval, Zh. N. Issabekov. Study of Tapered threads parameters affecting the quality of the oil pipeline connection. Advanced Engineering Research, 2022, vol. 22, no. 3, pp. 242–251. https://doi.org/10.23947/2687-1653-2022-22-3-242-251

Introduction. Exaggeration of the operating conditions for pipes is associated with the complication of profiles and an increase in the depths of wells in new oil-and-gas fields. Oil and gas grade pipes are exposed to significant alternating loads at the operating temperature ranges from minus 60 °C to plus 200 °C [1–6]. The products in question must meet the requirements for resistance to fatigue and brittle fracture, as well as corrosion resistance in aggressive

environments. This determines the choice of materials for their production. The considerable length of oil and gas pipelines implies providing reliable connection of pipes. Domestic manufacturers offer coupling and inserted connections with conical trapezoidal and triangular threads [7–10]. In the coupling types, the following are distinguished:

– CPTT (for casing pipes with trapezoidal thread and increased tightness);

– with buttress trapezoidal thread.

The connection of the first type is characterized by high tightness and resistance to tensile loads. These qualities are provided by the shape of the thread profile — an uneven trapezoid with a pitch of 5.08 mm and a taper of 1:16 (Fig. 1)

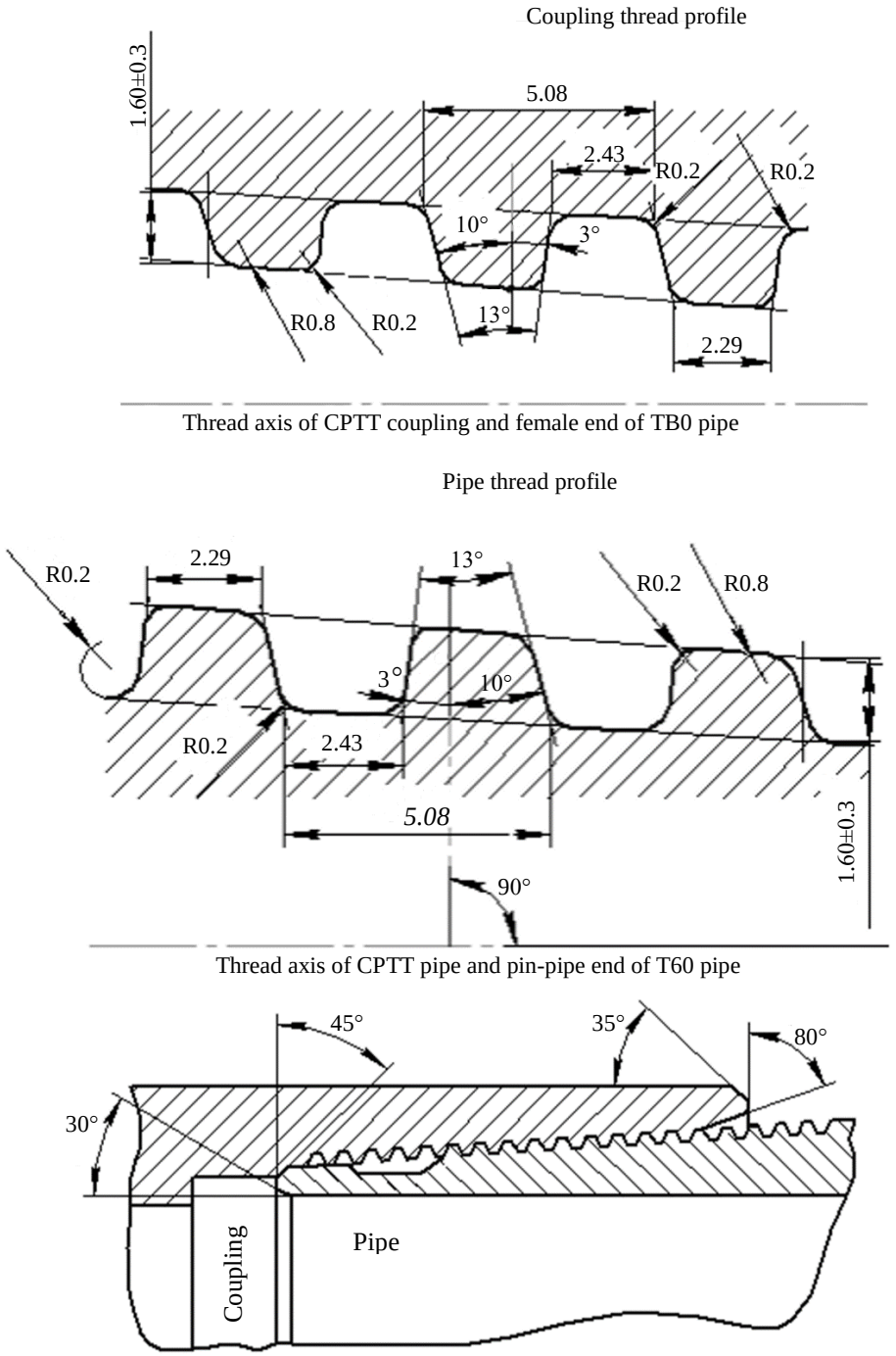

Fig. 1. Coupling connection of casing pipes of CPTT type

The angle of the stab flank of the pipe of 10 ° provides an easy fit into the coupling and reduces the probability of thread jamming. Under tensile and bending loads, the pipe thread should not disengage from the coupling thread; therefore, the support end of the profile is made at an angle of 3 ° [8–12]. The mating conical sealing surfaces located behind the thread increase the tightness. When connecting, the amount of tension is limited due to the contact of the products along the inner bearing faces. The sealing ring made of PTFE increases the tightness of the joint [13].

The scheme of the coupling connection with a trapezoidal buttress thread is shown in Figure 2.

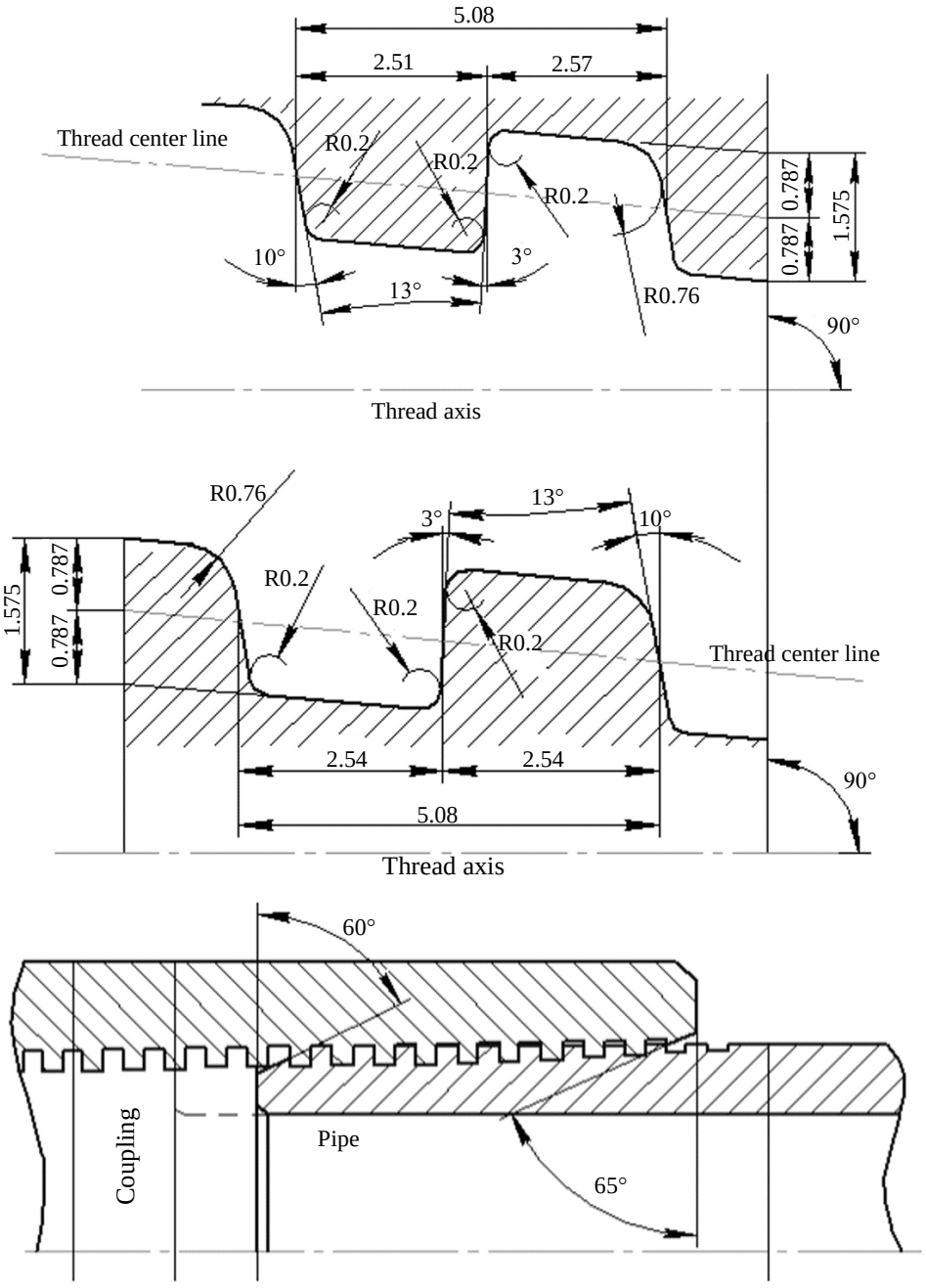

Fig. 2. Coupling connection of buttress casing pipes

A distinctive feature of this type of connection is the ability to take significant tensile loads for a long time. The buttress thread profile has the shape of an unequal trapezoid with a pitch of 5.08 mm and a taper of 1:16 [14].

The angles of inclination of the embedded and support ends are 10° and 3°, respectively. This simplifies assembly and reduces the probability of jamming. For tightness, a special lubricant or fluoroplastic rings are used [15].

Basic requirements for common type of casing pipe connections:

– permeability in wellbores of varying complexity and depth, including in areas of significant curvature;

– tightness of pipe columns and high strength for all types of loads;

– providing the passage of devices and tools into the inner space of the pipe columns during technological operations.

It is required to strictly comply with the requirements of standards for the quality of threaded connections, as well as for the means and methods of control. The characteristics of threaded connections of casing pipes are regulated by GOST 632–80 and API 5B international standards. These documents prescribe to control the following parameters: appearance of the thread, thread geometry and sealing conical surfaces, tension on the threaded working gage.

Note that the shapes of the mating elements of the pipe and coupling in cross sections do not always coincide. In these cases, in some areas, the mating surfaces will not contact, that is, the mating will remain loose. This creates conditions for a leak in the connection. If such a gap is not eliminated by positive drawing-up of the conical joints, then it is impossible to provide the effect of a ring lock, which guarantees tightness. Thus, deviations from the taper create prerequisites for leaks. As an example, consider the connections of CPTT and buttress pipes with an outer diameter of 127 mm. On a section of 25.4 mm, the permissible deviations from the taper are respectively: $^{+0.3}_{-0.2}$ mm and $^{+0.45}_{-0.25}$ mm.

Materials and Methods. The data obtained in the framework of the study were statistically processed using generally accepted methods.

To determine the degree of tightness of the suitable pipes, the radial runout of the conical and cylindrical surfaces of the pipes was measured. These elements were fixed in the outside jaws of a three-lobe lathe chuck (i.e., along the pipe base surface on 1I611P machine), subject to minimization of elastic deformations of the object from the clamping forces. First, the lathe jaws were brought into contact with the nozzle with a force sufficient to hang it off — this is how its axial position in the chuck was corrected when the spindle was turned. The surface runout was visually controlled. Then, in the plane of the jaws, a contact was created between the surface of the tubular part and the dial gauge mounted on the rack (Fig. 3). The tubular part was clamped in the chuck jaws. The gauge arrow was used to make sure that the clamping force did not deform the wall of the tubular part between the chuck jaws.

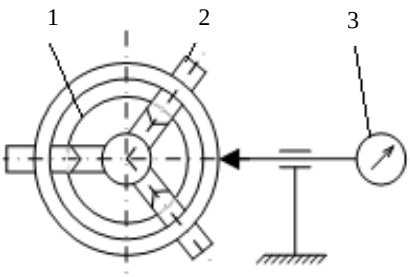

Fig. 3. Scheme for measuring radial runout of the tubular parts and couplings:
1 — product; 2 — three-lobe lathe chuck; 3 — dial gauge

To measure the runout of the seal band and chamfer, the lathe slide with the gage holder initially remained stationary, and the ball attachment of the gage was installed in the middle of the band and in the middle of the chamfer. The gage readings were taken and recorded by turning the machine spindle every 10° (fixed in 36 sections, starting from zero). The gage moved in the axial direction of the part, the ball attachment maintained its position relative to the center of the chamfer or band.

The runout of the threaded surface was measured along the thread ledge ribbon. To do this, the gear and the feed box of the machine were tuned to an inch thread with five threads per inch. After turning on the sliding clasp nut through spinning the spindle, all backlashes in the kinematics of the machine were selected. At that, the gage was set to

the middle of the ribbon of the first thread in the zero section.

Research Results. Figure 4 shows the results of measuring the radial runout of the outer surfaces of the tubular parts with various connections in the polar coordinate system.

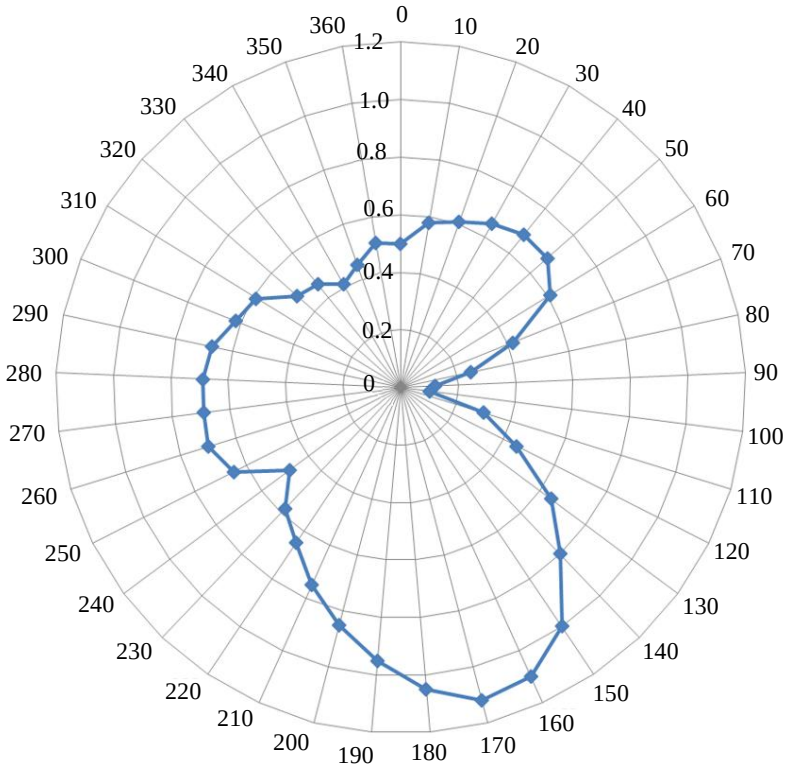

a)

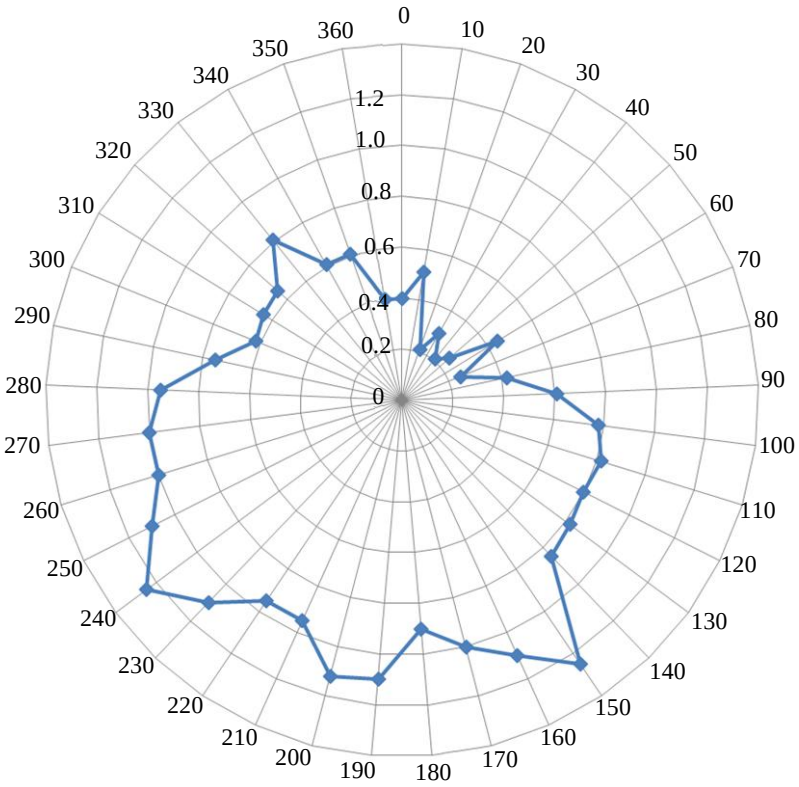

b)

Fig. 4. Radial runout of the outer surfaces of threaded pipes: *a* — buttress; *b* — CPTT

To control the taper in the tolerance field, the deviations of the thread heads on five threads from a given profile (Archimedean spiral) in the radial direction were measured. For the buttress tubular part, a graph was plotted in the polar coordinate system based on the values of the measured radial runout of the surface of the thread heads (Fig. 5 *a*). Here, the radial scale had values from 0 to 2 mm, and the circular scale — from 0 ° to 360 °. Similarly, the radial runout of the thread apexes on the CPTT tubular parts was investigated (Fig. 5 *b*).

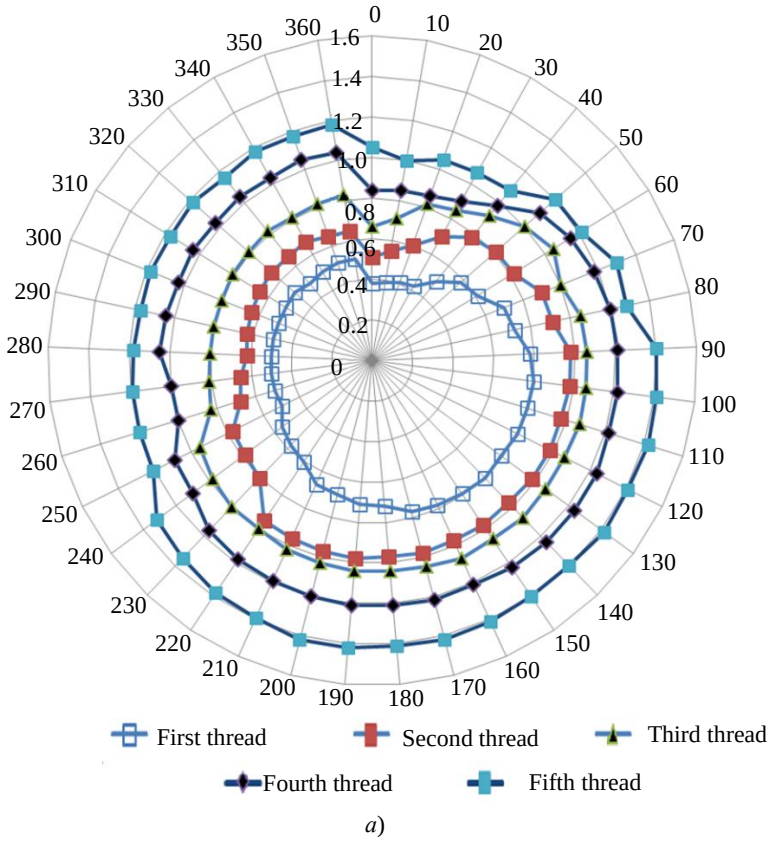

a)

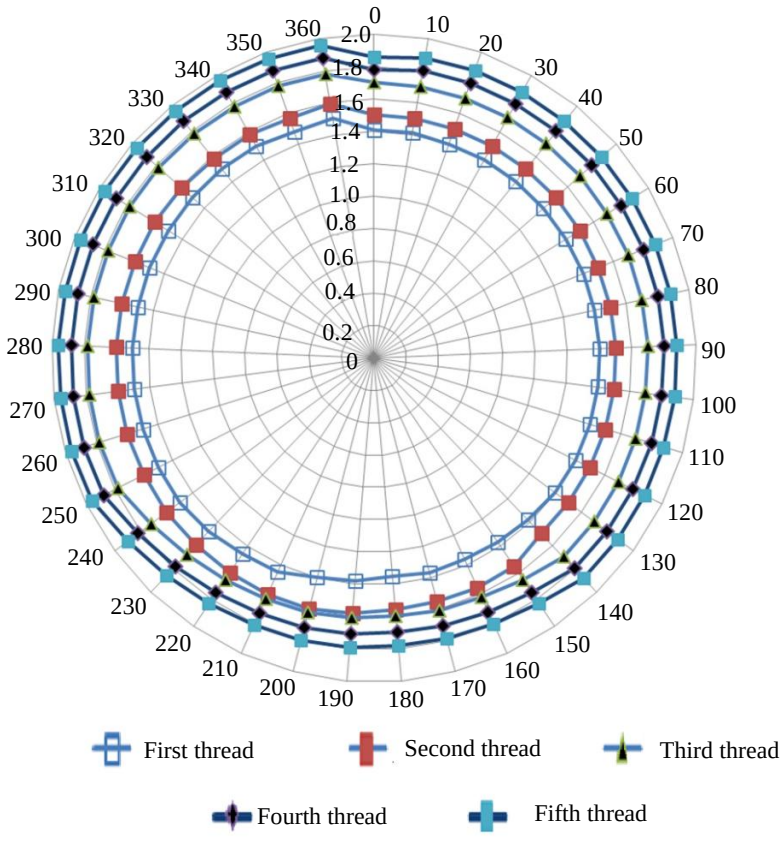

b)

Fig. 5. Radial runout of the surface of the thread heads from the start of thread at five turns: *a* — buttress; *b*— CPTT

The diagram (Fig. 6 *a*) is based on the results of measuring the radial runout of the chamfers of tubular parts with buttress thread. The values of the radial runout of the band are reflected in graph 6 *b*, which shows the circularity deviation of the seal band. Comparison of the values of the circularity deviation of the band shape obtained by different methods shows their identity.

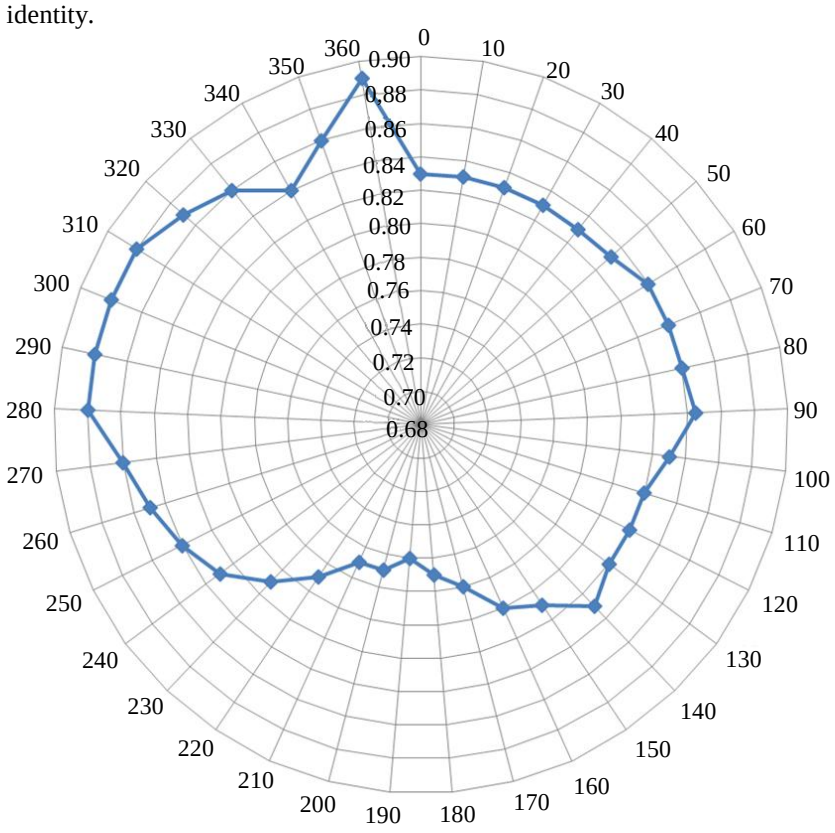

a)

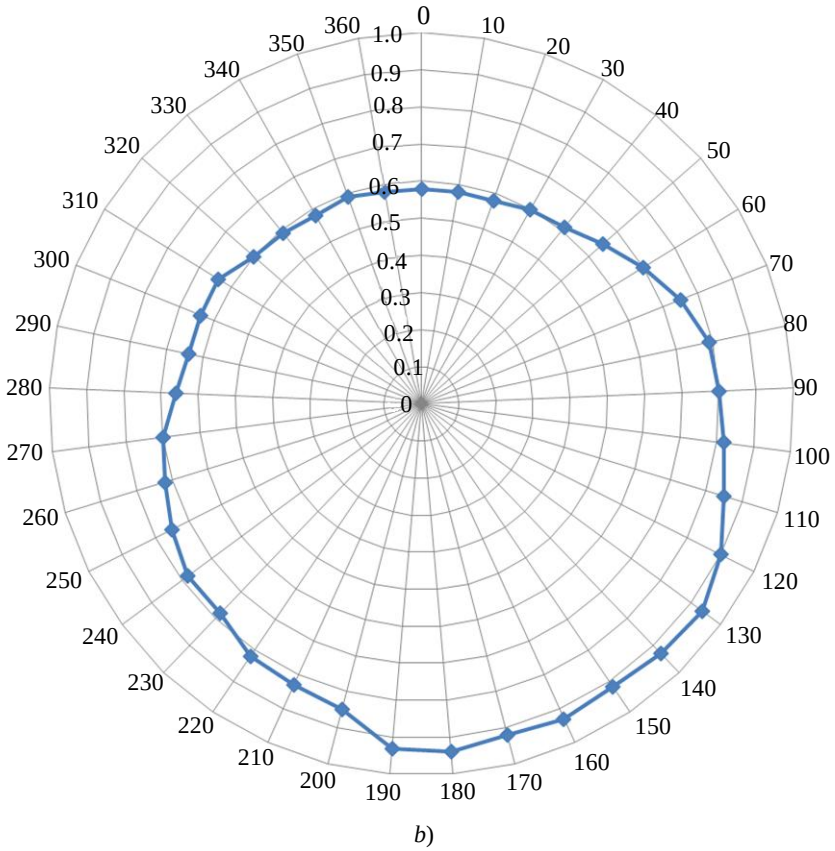

b)

Fig. 6. Radial runout: *a* — of the tubular part chamfer with buttress thread; *b* — of the seal band of the CPTT connection

Discussion and Conclusions. The analysis of Figure 4 has shown that pipes with different types of connections are characterized by significant taper deviations. At the same time, the surface of the pipe with a buttress thread is relatively smooth. If the diagram visualizes the CPTT thread, then there are sharp outliers of a large number of points. This means that there is a rough microrelief on the surface of the pipe with significant random surface level differences.

In Figure 5 *a*, the irregularity of the ascending spiral line with a difference of radius vectors of more than 0.4 mm is clearly visible. The wave-like change in the ordinate line of the profile is a consequence of the mismatch of the rotation axis of the tubular parts and the thread axis. This harmonic component can be compensated by special mathematical processing, which was not planned in this study. The analysis of Figure 5 *b* shows rather large irregularity of the ascending line of the thread head. This indicates significant deviations of the surface under consideration from a given profile (Archimedean spiral) for the CPTT connection.

The analysis of Figure 6 has shown that the deviation from sphericity (difference between the largest and smallest radii-runout vectors) is about 0.25 mm. The shape errors of the seal band for the CPTT connection were determined by different methods. According to the measured values of the band diameter (in the plane of the end face), a variation in size up to 0.25 mm (from the zero section, through 30 °) was detected: 169.35; 169.20; 169.10; 169.15; 169.25; 169.30. The angular distribution of the diameter counts indicated the oval shape of the band surface in cross section.

Thus, it can be concluded that there are significant deviations on the surfaces of pipes and couplings. We are talking about the quality of threads, chamfers, bands, which determines the connection reliability. These deviations cause the appearance of defective products in the batch. Their use does not provide the tightness and reliability of the pipe — coupling connection, which causes leaks during hydraulic tests. The specified connection quality is provided only by the method of group interchangeability, which requires preliminary separation of the assembled products into groups and generates additional costs. It is required to tighten the tolerances for the manufacture of threaded parts of pipes and couplings, which will allow for the assembly by the method of complete interchangeability. The considered deviations may occur due to the instability of the technological process of obtaining threads. In particular, the insufficient rigidity of the technological system and its untimely adjustment affects negatively.

References

1. Cirimello GP, Otegui L, Carfi G, et al. Failure and Integrity Analysis of Casings Used for Oil Well Drilling. Engineering Failure Analysis. 2017;75:1–14. http://dx.doi.org/10.1016/j.engfailanal.2016.11.008

2. Song S, Collins SH. Optimizing Exoskeleton Assistance for Faster Self-Selected Walking. IEEE Transactions on Neural Systems and Rehabilitation Engineering. 2021;29:786–795. http://dx.doi.org/10.1109/TNSRE.2021.3074154

3. Jackson RW, Dembia CL, DelpSL, et al. Muscle-Tendon Mechanics Explain Unexpected Effects of Exoskeleton Assistance on Metabolic Rate during Walking. Journal of Experimental Biology. 2017;220:2082–2095. https://doi.org/10.1242/jeb.150011

4. Li Tian, Yan Hai, Zeng Qingyue, et al. Non-destructive Testing Techniques Based on Failure Analysis of Steam Turbine Blade. IOP Conference Series: Materials Science and Engineering. 2019;576:012038. https://iopscience.iop.org/article/10.1088/1757-899X/576/1/012038/meta

5. Yinping Cao, Yan Pan, Hongxue Mi, et al. Experimental Study of Hoop Stress of Crescent Shaped and Eccentric Worn Casing. IOP Conference Series: Earth and Environmental Science. 2021;804:022014. 10.1088/1755-1315/804/2/022014

6. Yihua Dou, Yufei Li, Yinping Cao, et al. FE Simulation of Sealing Ability for Premium Connection Based on ISO 13679 CAL IV Tests. International Journal of Structural Integrity. 2020;12:138–148. 10.1108/IJSI-11-2019-0125

7. Huifeng Liu, Wei Zhang, Yinping Cao, et al. Analysis of the Performance Improvement Effect of Combined Packing for Oil and Gas Well Packer. IOP Conference Series: Earth and Environmental Science. 2020;514:022017. 10.1088/1755-1315/514/2/022017

8. Jie Zheng, Yihua Dou, Yinping Cao, et al. Prediction and Analysis of Wellbore Temperature and Pressure of HTHP Gas Wells Considering Multifactor Coupling. Journal of Failure Analysis and Prevention. 2020;2:23–28. 10.1007/s11668-020-00811-2

9. Yinhua Dou, Stefan Miska, Yinping Cao. An Experimental Study of Whirling Motion and the Relationship between Torque and Rotary Speed for Simulated Casing Drilling. Chemistry and Technology of Fuels and Oils. 2020;56:285–299. 10.1007/s10553-020-01138-2

10. Shangyu Yang, Lihong Han, Jianjun Wang, et al. Laboratory Study on Casing Deformation during Multistage Horizontal Well Fracturing in Shale Gas Development and Strain Based Casing Design. Journal of Natural Gas Science and Engineering. 2021;89:103893. https://doi.org/10.1016/j.jngse.2021.103893

11. Hang Wang, Wenlong Zhao, Zhenhui Shu, et al. Failure Analysis of Casing Dropping in Shale Oil Well during Large Scale Volume Fracturing. Engineering Failure Analysis. 2020;118:104849. https://doi.org/10.1016/j.engfailanal.2020.104849

12. Lihong Han, Fei Yin, Shangyu Yang, et al. Coupled Seepage-Mechanical Modeling to Evaluate Formation Deformation and Casing Failure in Waterflooding Oilfields. Journal of Petroleum Science and Engineering. 2019;180:68–72. 10.1016/j.petrol.2019.05.035

13. Lihong Han, Ming Liu, Sheji Luo, et al. Fatigue and Corrosion Fatigue Behaviors of G105 and S135 High-Strength Drill Pipe Steels in Air and H_2S Environment. Process Safety and Environmental Protection. 2019;124:63–74. 10.1016/j.psep.2019.01.023

14. Shangyu Yang, Lihong Han, Chun Feng, et al. Mechanical Performance of Casing in In-situ Combustion Thermal Recovery. Journal of Petroleum Science and Engineering. 2018;168:32–38. 10.1016/j.petrol.2018.04.068

15. Yufei Li, Yinping Cao, Yuxue Liu, et al. Research on Well Trajectory Deduction Method Based on Pythagorean-Hodograph Quintic Space Curves. IOP Conference Series: Materials Science and Engineering. 2019;688:033068.

Received 01.08.2022

Revised 29.08.2022

Accepted 31.08.2022

About the Authors

Tsybrii, Irina K., associate professor of the Tool Engineering and Biomedical Engineering Department, Don State Technical University (1, Gagarin sq., Rostov-on-Don, 344003, RF), Cand.Sci. (Eng.), associate professor, SRF, ORCID, irconst@mail.ru

Koval, Nikolai S., associate professor of the Tool Engineering and Biomedical Engineering Department, Don State Technical University (1, Gagarin sq., Rostov-on-Don, 344003, RF), Cand.Sci. (Eng.), ResearcherID, ScopusID, ORCID, koval-nc@mail.ru

Zhanibek N. Issabekov, Head of the Industrial Engineering Department, Satbayev University (22a, Satpaev St., Almaty, 050013, Republic of Kazakhstan), M.Sci. (Eng.), ORCID, zh.issabekov@satbayev.university

Claimed contributorship:

I. K. Tsybrii: academic advising; basic concept formulation; research objectives and tasks; computational analysis; correction of the conclusions. N. S. Koval: text preparation; formulation of conclusions; analysis of the research results. Zhanibek N. Issabekov: the text revision.

Conflict of interest statement

The authors do not have any conflict of interest.

All authors have read and approved the final manuscript.

MACHINE BUILDING AND MACHINE SCIENCE

UDC 621.792
https://doi.org/10.23947/2687-1653-2022-22-3-252-260

Original article

Methods and Equipment for Experimental Evaluation of the Performance of Shell and Hull Structures

Yury G. Lyudmirsky[1] ✉, **Semyon S. Assaulenko**[1], **Aleksandr V. Kramskoi**[2]
[1] Don State Technical University, 1, Gagarin sq., Rostov-on-Don, Russian Federation
[2] AEM-Technologies, Atommash Branch, 10, Zhukovsky Highway, Volgodonsk, Rostov Region, Russian Federation
✉ lyudmirskiy40@mail.ru

Abstract

Introduction. Pressure-operated thick-walled hull structures are the most common type of high-duty welded structures. When these structures are loaded with internal pressure, a complex biaxial stress field arises in them, which is summed up with the fields of residual welding stresses. Therefore, when selecting a technology for manufacturing critical welded structures, the results obtained during conventional uniaxial tests of samples are insufficient. The variety of factors affecting the performance of structures, and the difficulties of separate assessment of their influence, caused the need to maximize the approximation of experimental conditions to the real working conditions of the structure.

Materials and Methods. Testing of full-scale structures has a number of advantages, but they are extremely expensive, and, as a rule, only one, the weakest link, is identified, the bearing capacity of the other structural elements remains unclear. For testing, UDI radiometric installations designed for different sample sizes were used. The presented installations allow testing samples of various shapes, types of welded joints (butt, T-bar), changing the position of welded parts.

Results. Without rejecting the results obtained during the testing of full-scale structures in the works of the Bauman Moscow State Technical University, DSTU, NRC "Kurchatov Institute" – CRISM "Prometey", and the authors proposed to conduct the basic scope of the research on individual structural elements that would reflect the characteristic features of loading, manufacturing technology, and operating conditions. The design of the "fitting-sheet" connections was applied, which made it possible to increase the indicators of the failure initiation and propagation to the level of the base metal.

***Discussion and Conclusions*.** Schemes of structures for obtaining a biaxial tension or bending field in samples were presented. Samples tested according to the proposed schemes allowed us to draw conclusions about the performance of welded joints under conditions close to the actual operation of the structures under study. The proposed test scheme is used by research laboratories in our country and around the world.

Keywords: tests of full-scale structures, design experience, installations for biaxial tension and bending, durability, "fitting-plate" connection.

Acknowledgments. The authors are deeply grateful to V. F. Lukyanov, Dr.Sci. (Engineering), professor, Head of the Machines and Welding Fabrication Automation Department, for years of joint work and academic advising.

For citation. Y. G. Lyudmirsky, S. S. Assaulenko, A. V. Kramskoi. Methods and Equipment for Experimental Evaluation of the Performance of Shell and Hull Structures. Advanced Engineering Research, 2022, vol. 22, no. 3, pp. 252–260. https://doi.org/10.23947/2687-1653-2022-22-3-252-260

Introduction. Thick-sheet hull pressure-operated structures are the most common type of high-duty welded structures. When these structures are loaded with internal pressure, a complex, predominantly biaxial stress state occurs, in which the fields of residual welding stresses are summed up with the stress fields from the external load. Under these conditions, there is often an increased sensitivity of both the base metal and welded joints to the presence of stress concentrators or a local change in the mechanical properties of the metal associated with the manufacturing process, which can cause a sharp decrease in strength. Currently, despite a number of fundamental studies on the strength of welded sheet and hull structures, there is still insufficient systematic data on the patterns of resistance to the initiation and development of destruction of large-sized elements of welded structures, depending on structural, technological, and operational factors. Therefore, for the choice of material and manufacturing technology of critical platework, the data obtained through conventional uniaxial tests of samples is sometimes insufficient. The variety of factors affecting the operability of structures and the difficulties of separate assessment of their influence necessitates bringing the course of the experiment to real conditions as close as possible. This has led to the spread of methods for testing full-size structures or their models. To conduct such tests in our country and abroad, stands equipped with sophisticated testing and diagnostic instruments have been created. One example is as follows: for testing full-size large-diameter pipes, there are stands in UralNITI, Volga Pipe Plant, VNIIST, CRISM “Prometey”, and in other laboratories. There are stands of a similar purpose in Japan. In the USA, there are more than 300 installations for testing structures operating under static and pulsating pressure.

Tests of full–scale structures have a number of advantages:

– real technology of manufacturing the structure is preserved, as a result of which the uncertainty associated with the influence of simulation of the manufacturing process on the test results is eliminated;

– real scheme of loading of individual elements and components of structures is preserved;

– they enable to establish the actual distribution of failures in the structure and to specify the accepted design scheme;

– they provide assessing the resistance to the initiation and development of fracture of only one of the weakest structural elements;

– they enable to study the effect of stress concentration and residual stresses on fatigue strength.

Despite the undoubted value of field tests to assess the structural strength of the product, it is extremely irrational to use such tests to study individual factors affecting the strength of the structure. The abundance of factors simultaneously affecting the course of the study makes it difficult to analyze the causes of premature fracture and does not allow us to separately assess the degree of influence of each of them. As a result of testing of full-size structures, as a rule, it is possible to identify the weakest link, whereas the bearing capacity of the rest of the sections (elements) of the structure remains unknown.

The above disadvantages can be practically eliminated if the bulk of the research is carried out on reduced-size models of shell structures. Such tests allow us to get answers to questions related to the structural strength and reliability of the product, to identify the degree of danger of the initiation and development of crack-like defects, to evaluate the effectiveness of various ways to increase durability.

Without rejecting the test results obtained on simple uniaxial samples and when testing full-scale structures at the Bauman Moscow State Technical University, DSTU, NRC “Kurchatov Institute” – CRISM “Prometey”, the authors propose to transfer the bulk of the research to testing individual structural elements that reflect the characteristic features of its loading, manufacturing technology, and operating conditions.

In relation to shell and hull structures, during testing, it is required to take into account:

– stress state (biaxial with equal or unequal components of the primary stresses);

– loading condition (static or repeated static with different loading cycles);

– environmental impact;

– influence of operating temperature.

Materials and Methods. This paper describes the experience of designing installations for testing metal and welded joints under biaxial stress.

The analysis carried out in [1–5] has shown that the working conditions of metal and welded joints in steel-plate structures are most fully reproduced when tested under hydrostatic buckling. In this case, the sample is fixed or supported along the contour and loaded with hydrostatic pressure.

The stress state that occurs in the sample metal depends on the shape of the sample, the conditions of its fixation (pinching or loose support on the die), the shape of the die. Figure 1 shows the loading schemes and the resulting biaxial bending or stretching stresses.

When a flat sample supported along the contour of the circular hole of the die is loaded with hydrostatic pressure, a biaxial bend occurs. A significant part of the external convex surface of the sample is subject to uniform stretching with equal stress components $\sigma_1 = \sigma_2$ (Fig. 1 *a*). If the flat sample is securely pinched along the contour of the die hole, then biaxial stretching is applied to the biaxial bend. In the case of loading not a flat sample, but a spherical segment with a sufficiently large ratio of the diameter of the die hole to the thickness of the sample, the bending component is small, and it can be assumed that the central part of the sample is subject to the biaxial stretching with $\sigma_2/\sigma_1 = 1$ (Fig. 1 *b*). Biaxial stretching with unequal components within the ratio $\sigma_2/\sigma_1 = 1.0...0.75$ can be obtained by buckling the sample according to the scheme shown in Figure 1*b*, using dies with elliptical holes.

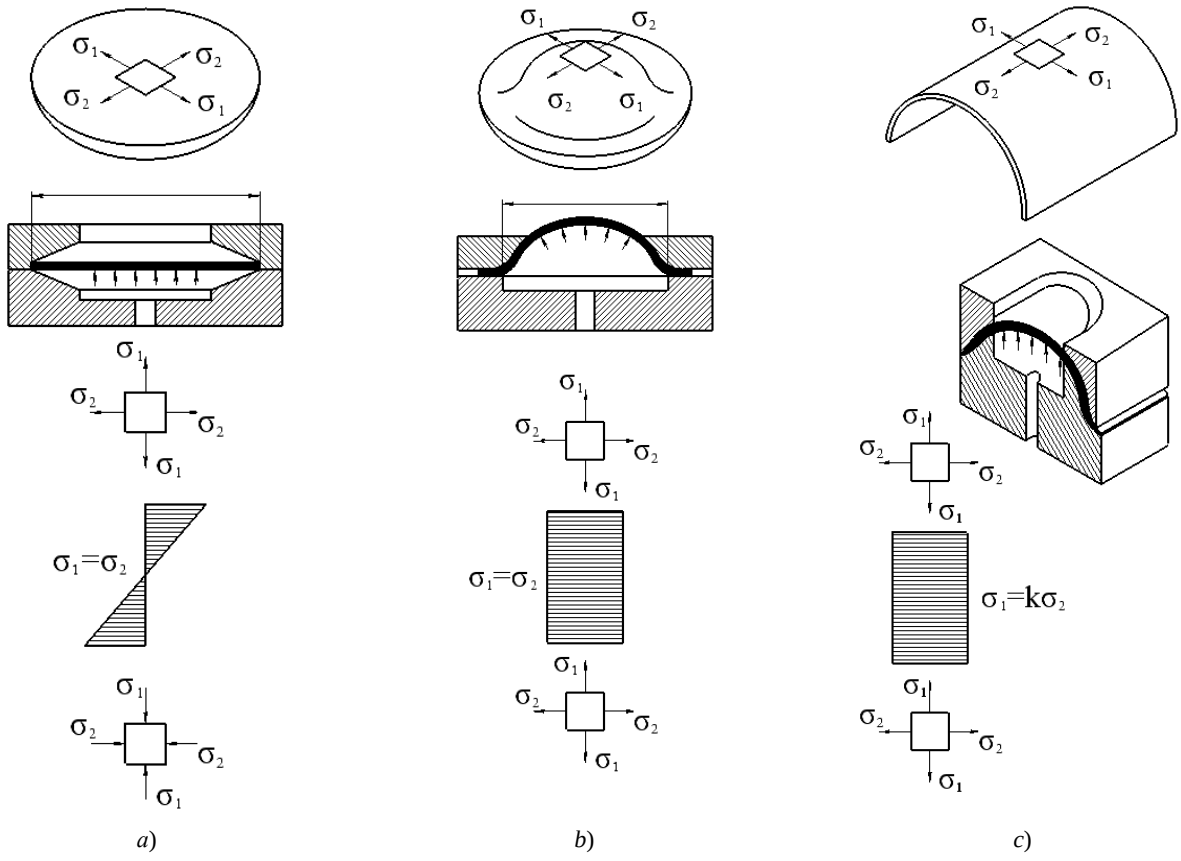

Fig. 1. Loading schemes of samples to obtain a biaxial stress field in them :
a — loading of a flat sample with equal stress components; *b* — loading of a spherical segment;
c — loading of a sample in the form of a cylindrical panel

A further decrease in the ratio σ_2/σ_1 = (0.7… 0.3) is obtained using the scheme shown in Figure 1 *b*, where a cylindrical-panel sample, pinched by a flange part between the cylindrical die and the cylindrical punch, is loaded with hydrostatic pressure [3, 4].

For steel-plate pressure-operated structures, two types of loading are characteristic: single (static) and low-cycle (repeated static). For the first, it is reasonable to use schemes *a* and *b* (Fig. 1). Under static loading, the scheme test can be carried out both on samples in the form of flat sheets and the pre-formed spherical segments [5–7].

Plates are preferable, since their production is less labor-intensive. Samples in the form of a spherical segment can reduce the edge effect of fixing the sample along the contour. However, the preparation of such samples requires plastic deformation, and this can cause a change in the mechanical properties of the material, which is not always correctable even by subsequent heat treatment.

When testing under low-cycle loading conditions, all three schemes shown in Figure 1 can be used. However, preference should be given to biaxial bending according to scheme *a*, since it provides testing large thicknesses.

The resistance to fracture nucleation and development under tension is usually evaluated using schemes *b* and *c* (Fig. 1) on pre-formed samples that are made in the form of a spherical segment or a cylindrical panel.

The environment has a particularly strong impact on the results of long-term and repeated static tests. Of great interest is the resistance of materials under repeated static loading in corrosive environments [8–10].

To study the processes of nucleation and the development kinetics of fracture in the elements of hull structures, a series of installations has been developed in DSTU together with the NRC "Kurchatov Institute" — CRISM "Prometey": UDI–550, UDI–980, UDI–1300. Their key characteristics for biaxial bending are presented in Table 1.

Advantages of these installations:

– powerful force actuators are not required for loading;

– it is possible to test samples with a relatively uniform distribution of stresses on a large surface;

– it is possible to test individual elements of welded structures with almost complete preservation of technological features and the pattern of stress distribution in the area of welds, to take into account the influence of the corrosive environment.

Table 1

Characteristics of power units of installations for testing base metal and welded joints under biaxial bending conditions

Installations	Geometry of test samples		Yield strength of materials Ϭ0.2, MPa	Maximum pressure P, MPa
	diameter, mm	thickness, mm		
UDI-550	550	20-40	≤ 900	≤ 1,000
UDI-980	980	30-60	≤ 900	≤ 1,000
UDI-1300	1300	60-100	≤ 900	≤ 1,000

The created installations make it possible to determine the cyclic strength of various materials in air and in a corrosive environment, to obtain information about the failure pattern with different structural and technological design of welded joints of full thickness, to evaluate the efficiency of various methods to increase durability.

The design of the installations intended for testing under conditions of biaxial bending of welded joints made of sheet metal with a thickness of 20-100 mm with a yield strength up to 15 MPa is shown in Figure 2. They consist of four blocks 1, in which samples are fixed, a control panel 2 and pumping stations, which are not shown in the figure.

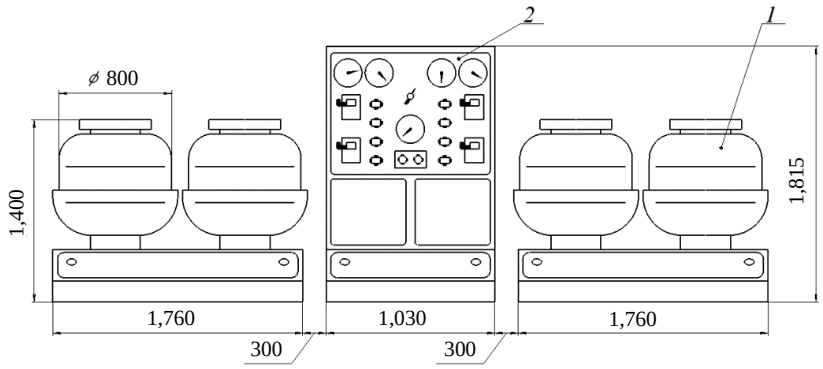

Fig. 2. Design of installations for testing under biaxial bending conditions:
1 — test installation; 2 — control panel

The basic design of the power units of UDI-550, UDI-980, and UDI-1300 installations is the same and is shown in Figure 3.

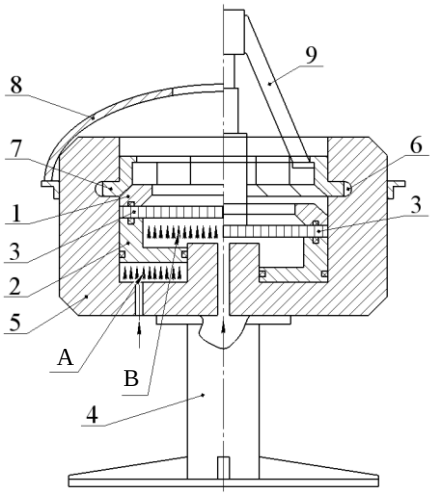

Fig. 3. UDI-type power unit of installations for testing welded joints under biaxial bending:
1 — die; 2 — hydraulic clamp; 3 — test sample; 4 — base; 5 — locking device (cup); 6 — inner ring groove;
7 — ring locking sectors; 8 — protective casing; 9 — hydraulic jack

The installation contains a die 1 and a hydraulic clamp 2, between which a sample 3 and a locking device 5 are placed, which is fixed on the base 4. The locking device is made in the form of a fixed smooth cup with an internal groove 6, in which annular locking sectors 7 (eight pcs.) are located along the entire perimeter, having an L-type shape in axial section.

The installation works as follows. The sample 3 in the form of a round disk is mounted on the hydraulic clamp 2, a die 1 is mounted on top of it. Then, eight removable annular sectors 7 are laid in the groove of the locking device 5, pressing them tightly together so as to provide minimal gaps between them.

The installation is covered with a protective casing 8. After that, the pumping station is turned on, and pressure is applied to the cavity A formed by the bottom of the locking device 5 and the hydraulic clamp 2. Under the impact of pressure, the hydraulic clamp 2 moves upwards, presses the sample 3 to the die 1, and the die — to the annular sectors 7. The sectors rest against the support surface of the annular groove and the inner surface of the cup 5, preventing the movement of the die 1, thereby fixing the sample 3 in the installation.

Then, the liquid flow is directed into the cavity B under the sample 3. Under the influence of pressure, the sample, resting on the edge of the hole in the die 1, bends, and biaxial tensile stresses arise on its outer side. The magnitude of tensile stresses on the surface is regulated by the pressure in the cavity B. The hydraulic system allows for repeated static loading of samples with a loading frequency of ten cycles per minute.

The scheme of disassembly and extraction of the sample is shown in the right part of Figure 3.

After the end of the tests, a hydraulic jack 9 is installed on the sample 3, which rests with its paws on the projections on the annular sectors 7. When connecting the jack to the hydraulic system of the installation, its piston presses on the sample and moves it together with the hydraulic clamp 2 down to the start position, which provides disassembling of the installation.

In the process of testing, the number of cycles before the failure (crack length 8–12 mm), the crack development kinetics, and the destruction of the sample (in this case, it is loss of tightness) are recorded.

The electrical and hydraulic circuits of the installations allow for static or repeated static loading. The loading cycle can be pulsating or with a positive coefficient of asymmetry. The frequency of loading samples is adjustable from two to ten cycles per minute.

In cases where the effect of a corrosive medium is of interest, it is poured into the cavity formed by the sample and the die 1. To protect against corrosion, the die should be coated with a layer of epoxy resin or varnish, or an annular rubber collar should be glued to the sample, preventing the spreading of the corrosive medium beyond the test part of the sample.

Depending on the testing purpose, samples of various types and sizes are used. Some of them are shown in Figure 4 as an example.

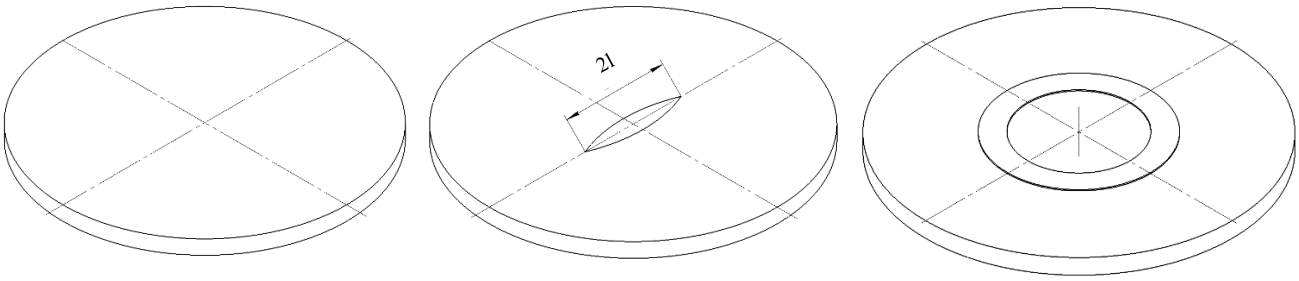

a) *b*) *c*)

Fig. 4. Samples providing for assessment of the corrosive environment impact (3% NaCl solution): a – from the basic; b – linear notch; c – annular notch

To assess the resistance to the nucleation and development of the base metal fracture in a biaxial stress field under the simultaneous action of a corrosive medium, it is reasonable to use smooth and notched samples. Comparative tests of these samples in air and in a 3 % NaCl solution have shown that this medium accelerates the processes of nucleation and development of fracture. When tested in air, as a rule, one crack nucleates and develops. In the presence of a corrosive medium (3 % NaCl solution), even in the presence of stress concentrators, a multifocal pattern of the nucleation and development of cracks is observed, which significantly accelerates the destruction process — by 2–2.5 times [11–13].

The paper considers a method for increasing low-cycle fatigue of welded joints of the “fitting – plate” type. It is proposed to increase durability by reducing stresses on the stretched surface, where a corrosive environment acts, through reducing the average stresses in the joint [14, 15]. Figure 5 shows the proposed welded joint.

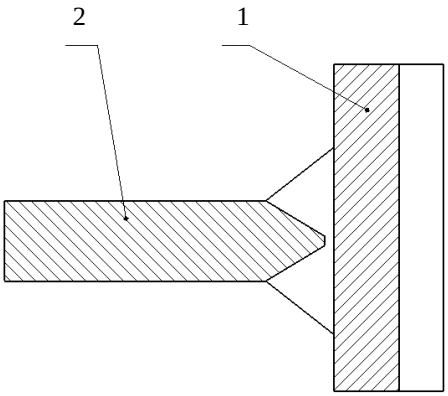

Fig. 5. Section of the welded joint of "fitting – plate" type: 1 — fitting; 2 — plate (shell)

The sample was tested on UDI-550 installation in a 3 % NaCl solution at rated voltages of 850 MPa. The test results showed that the number of cycles before the failure initiation doubled, and cracks appeared on the base metal. Photos of macrosections of the test results are shown in Figure 6.

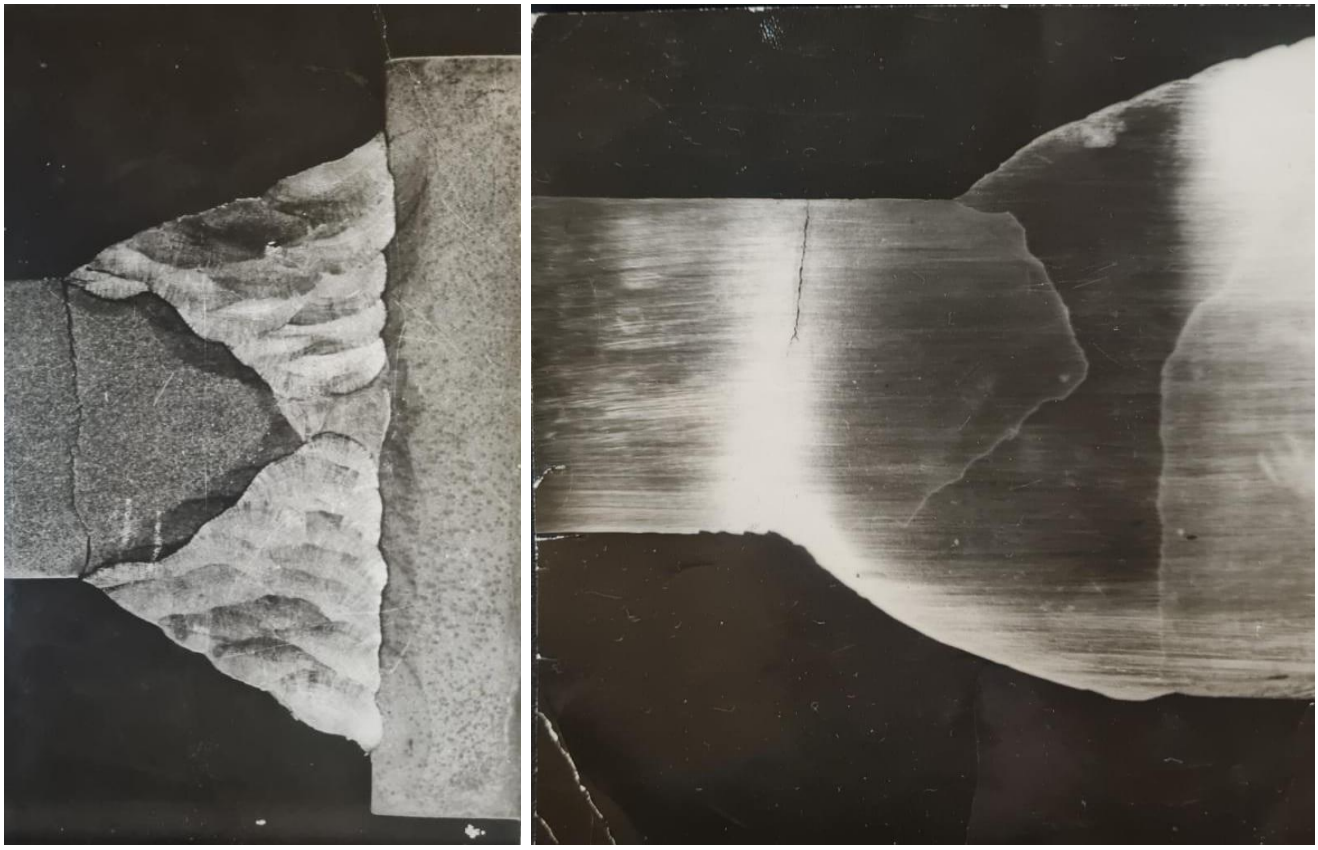

a) *b*)

Fig. 6. Test results of "fitting – plate" welded joints in a corrosive environment:
a — fitting connection with symmetrical welds; *b* — fitting connection
with reinforcing weld on compressed fibers (photo of the authors)

Analysis of the test samples allows us to establish that the durability of the fitting connection made by the proposed method turns out to be longer. In addition, due to the reinforcing influence of the weld metal from the side opposite to the action of the corrosive environment, the magnitude of the maximum tensile stresses in the most dangerous zone decreases; therefore, the resistance to the fracture initiation and development increases [16].

Research Results. Using the experience of designing individual installations and assemblies intended to test welded joints under biaxial bending conditions, scientists of DSTU and NRC "Kurchatov Institute" – CRISM "Prometey" have developed a series of installations designed to test sheet metal welded joints with a thickness of 20–100 mm with a yield strength up to 15 MPa under the biaxial bending conditions [17].

Discussion and Conclusions. 1. Equipment and testing methods of welded joints of the "fitting – plate" type, which operate under biaxial axisymmetric bending in a corrosive environment, were developed. This allowed us to evaluate the resistance to the fracture nucleation and development. The large size of the samples and the preservation of welding technology brought the results of these tests closer to the assessment of the bearing capacity of full-scale structures.

2. To assess the feasibility of using new technological or design solutions, it is required to test samples of full-scale thickness.

3. Failure of welded joints made according to serial (factory) technologies starts simultaneously at several sites along the fusion line, where there is a combination of unfavorable factors. The main role is played by factors of local stress increase, residual welding stresses, and the presence of corrosive environment.

4. To increase durability, designs of welded joints with an asymmetrical arrangement of welds relative to the plane of the sheet are proposed, which have a smaller weld leg from the side of the action of tensile stresses and corrosive environment than from the opposite side.

5. Installations and test methods have been implemented in the People's Republic of China and in the Republic of India.

References

1. Leonov VP, Malyshevskii VA. Structural and Technological Strength of Steel for Marine Structures. Metal Science and Heat Treatment. 2001;43:444.

2. Ilyin AV, Leonov VP, Filin VYu. Opredelenie parametra treshchinostoikosti CTOD dlya metalla svarnykh soedinenii sudokorpusnykh stalei pri nizkikh klimaticheskikh temperaturakh. Research Bulletin by Russian Maritime Register of Shipping. 2009;32:120–146. (In Russ.)

3. Fetisova EA, Lupachev AG. Peculiarities of Diffusion Processes in Dissimilar Steels Welded Joints. Vestnik of Belarusian-Russian University. 2014;3:79–87. https://doi.org/10.53078/20778481_2014_3_79

4. Ilyin AV, Filin VYu. On the Problem of Quantitative Service Life Assessment for High-Strength Steel Welded Structures under the Effect of Corrosion Medium. Procedia Structural Integrity. 2019;14:964–977. https://doi.org/10.1016/j.prostr.2019.07.078

5. Kazuo Tateishi, Takeshi Hanji. Low Cycle Fatigue Strength of Butt-Welded Steel Joint by Means of New Testing System with Image Technique. International Journal of Fatigue. 2004;26:1349–1356. https://doi.org/10.1016/j.ijfatigue.2004.03.016

6. Ilyin AV, Sadkin KE. Assessment of Structural and Technological Stress Concentration in Welded Joints for Fatigue Strength Estimation of Hull Structures. Materials Science Issues. 2012;2:161–176.

7. Dudka DV, Yakovlev SS, Bessmertnaya YuV. Kriterii sheikoobrazovaniya kristallicheskogo anizotropnogo listovogo materiala pri dvukhosnom rastyazhenii. Izvestiya Tula State University. 2010;3:108–112. (In Russ.)

8. Evdokimov DV. Otsenka predel'noi plastichnosti listovogo materiala pri dvukhosnom rastyazhenii. Izvestiya Tula State University. 2009;2–2:83–88. (In Russ.)

9. Dudka DV, Yakovlev SS, Bessmertnaya YuV. Lokalizatsiya deformatsii kristallicheskogo anizotropnogo listovogo materiala pri plasticheskom dvukhosnom rastyazhenii. Izvestiya Tula State University. 2010;3:85–88. (In Russ.)

10. Zenkov EV, Bagieva LA. Metodika modelirovaniya napryazhennogo sostoyaniya deformiruemykh ehlementov transportnykh sistem v usloviyakh dvukhosnogo rastyazheniya. Transportnaya infrastruktura Sibirskogo regiona. 2016;1:342–345. (In Russ.)

11. Bychenok VA, Berkutov IV, Mayorov AL, et al. Residual Stress Control in the near Seam Zone of the Welding Joint. Tekhnologiya Mashinostroeniya**.** 2019;12:45–50.

12. Sushanta Kumar Panda, D. Ravi Kumar. Experimental and Numerical Studies on the Forming Behavior of Tailor Welded Steel Sheets in Biaxial Stretch Forming. Materials & Design. 2010;31:1365–1383. https://doi.org/10.1016/j.matdes.2009.08.046

13. Lyudmirskii YG, Assaulenko SS, Ageev SO. Constructive and Technological Method of Increasing Durability of "Choke Connections". Journal of Physics Conference Series. 2021;2131:042061. https://doi.org/10.1088/1742-6596/2131/4/042061

14. Ritsu Nishimura, Ninshu Mab, Yong Liu, et al. Measurement and Analysis of Welding Deformation and Residual Stress in CMT Welded Lap Joints of 1180 MPa Steel Sheets. Journal of Manufacturing Processes. 2021;72:515–528. https://doi.org/10.1016/j.jmapro.2021.10.050

15. Xiaohui Zhao, Yanjun Fan, Yu Liu, et al. Evaluation of Fatigue Fracture Mechanism in a Flash Butt Welding Joint of a U75V Type Steel for Railroad Applications. Engineering Failure Analysis. 2015;55:26–38. https://doi.org/10.1016/j.engfailanal.2015.05.001

16. Shuai Wang, Cheng Hou, Bin Wang, et al. Mechanical Responses of L450 Steel under Biaxial Loading in the Presence of the Stress Discontinuity. International Journal of Pressure Vessels and Piping. 2022;198:104662. https://doi.org/10.1016/j.ijpvp.2022.104662

17. Andrea Corti, Tariq Shameen, Shivang Sharma, et al. Biaxial Testing System for Characterization of Mechanical and Rupture Properties of Small Samples. HardwareX. 2022;12:e00333. https://doi.org/10.1016/j.ohx.2022.e00333

Received 07.08.2022
Revised 02.09.2022
Accepted 05.09.2022

About the Authors:

Lyudmirsky, Yury G., professor of the Machines and Automation of Welding Production Department, Don State Technical University (1, Gagarin sq., Rostov-on-Don, 344003, RF), Dr.Sci. (Eng.), professor, ScopusID, ORCID, lyudmirskiy40@mail.ru

Assaulenko, Semyon S., senior lecturer of the Machines and Automation of Welding Production Department, Don State Technical University (1, Gagarin sq., Rostov-on-Don, 344003, RF), ScopusID, ORCID, assaulenko_s@mail.ru

Kramskoi, Aleksandr V., Head of the section of Development of Control of Welded Joints, AEM-Technologies, Atommash Branch (10, Zhukovsky Highway, Volgodonsk, Rostov Region, 347360, RF), Cand.Sci. (Eng.), ScopusID, ORCID, kramskoi_av@atommash.ru

Claimed contributorship:

Yu. G. Lyudmirsky: academic advising; analysis of the research results; correction of the conclusions. S. S. Assaulenko: computational analysis; text preparation; formulation of conclusions. A. V. Kramskoi: basic concept formulation; research objectives and tasks; the text revision.

Conflict of interest statement

The authors do not have any conflict of interest.

All authors have read and approved the final manuscript.

INFORMATION TECHNOLOGY, COMPUTER SCIENCE, AND MANAGEMENT

Original article

https://doi.org/10.23947/2687-1653-2022-22-3-261-271

Describing Pulmonary Nodules Using 3D Clustering

Amera Al-Funjan [1] ✉, **Farid Meziane** [2], **Rob Aspin** [3]
[1]Babylon University, Iraq
[2]University of Derby, Derby, UK
[3] Manchester Metropolitan University, Manchester, UK
✉ amera.alfunjan@uobabylon.edu.iq

Abstract

Introduction. Determining the tumor (nodule) characteristics in terms of the shape, location, and type is an essential step after nodule detection in medical images for selecting the appropriate clinical intervention by radiologists. Computer-aided detection (CAD) systems efficiently succeeded in the nodule detection by 2D processing of computed tomography (CT)-scan lung images; however, the nodule (tumor) description in more detail is still a big challenge that faces these systems.

Materials and Methods. In this paper, the 3D clustering is carried out on volumetric CT-scan images containing the nodule and its structures to describe the nodule progress through the consecutive slices of the lung in CT images.

Results. This paper combines algorithms to cluster and define nodule's features in 3D visualization. Applying some 3D functions to the objects, clustered using the K-means technique of CT lung images, provides a 3D visual exploration of the nodule shape and location. This study mainly focuses on clustering in 3D to discover complex information for a case missed in the radiologist's report. In addition, the 3D-Density-based spatial clustering of applications with noise (DBSCAN) method and another 3D application (plotly) have been applied to evaluate the proposed system in this work. The proposed method has discovered a complicated case in data and automatically provides information about the nodule types (spherical, juxta-pleural, and pleural-tail). The algorithm is validated on the standard data consisting of the lung computed tomography scans with nodules greater and less than 3mm in size.

Discussion and Conclusions. Based on the proposed model, it is possible to cluster lung nodules in volumetric CT scan and determine a set of characteristics such as the shape, location and type.

Keywords: automated 3D Clustering, CT lung images, describing the nodule characteristics.

Acknowledgements. The authors would like to thank the reviewers for their suggestions that improved the article.

For citation. Amera Al-Funjan, Farid Meziane, Rob Aspin. Describing Pulmonary Nodules Using 3D Clustering. Advanced Engineering Research, 2022, vol. 22, no. 3, pp. 261–271. https://doi.org/10.23947/2687-1653-2022-22-3-261-271

Introduction. Lung cancer is a leading cause of death worldwide among both men and women, with an impressive rate for nearly 10 million deaths in 2021. Around one-third of deaths from cancer are to smoking and second-hand smoke. Many cancers can be cured if detected early and treated effectively (1).

Computed Tomography (CT) is one of the most commonly medical imaging techniques used in the screening of lungs by generating three-dimensional imaging modalities and shows the lesions that cannot be visualized by conventional chest X-ray. CT technology is used widely by clinicians to detect, analyze, and diagnose numerous asymptomatic disease lung diseases such as pulmonary nodules and lung cancers, that cannot be detected by other

medical imaging technologies. Where, early detection of these diseases is an important of health promotion and chronic disease prevention. However, it is noted that a big challenge associated to radiologists is the analysis of huge amount of data generated by CT technology. Therefore, computer-aided diagnostic (CAD) is needed to provide a computerized diagnosis to assist clinicians for detection and interpretation of CT lung scans (2, 3). Segmentation and clustering are tasks that manipulate the medical image to extract significate information and reduce the search area of the region of interest in image components. Where, using clustering on volumetric scan of CT can provide more details about nodule shapes, characteristics, and their types which are suspected be missed by radiologists during the diagnosis. Additionally, it provides a precise description of lung's tissues with low-intensity (4, 5). The outcomes of 3D clustering can improve the precision in diagnosis of lung by identifying the nodule structures in the different levels, and the number of nodules (6, 7). This study aims to improve the accuracy of three- dimensional clustering of lung's nodules by using volumetric CT scans of lung. Where, the three-dimensional clustering efficiently can be used to observe the current nodule's progress which serves significantly the early diagnosis of lung. Furthermore, the precise details that can be extracted from the three-dimensional clustering offers a high potential to detect nodules and lesions with less than 3 mm.

Many studies focused on the possibility of developing a computer-aided system for diagnosing, detecting, and segmenting lung lesions in CT scans of lung (8). However, without using volumetric CT scans of lungs, the accurate identification and characterization of small pulmonary nodules have not been defined in the studies. Where, implementing quantitative analysis of CT scans of lungs face an obstacle due to inter-scan image intensity variations and irregular shapes of lung lesions. A major difficulty is encountered during clustering of lung's lesions because of the complex characteristics of lung's lesions and overlapping in intensity distributions in such cases. Additionally, some parts of lung's lesions may not be distinguished correctly because of the image resolution and the complexity of diagnosing lung's lesions in a visual examination. Therefore, a multi-dimensional CT scan is required to determine type and volume of lesions.

Javaid, Javid (9) proposed an automated method for segmenting and recognizing the pulmonary nodules into juxta-vascular or juxta-pleural. Where, thresholding and k-means were combined to segment lung and detect the pulmonary nodules respectively. Then, the pulmonary nodules were classified into sex groups according to percentage of connectivity with lung walls and thickness. Fetita, Preteux (10) developed a method for discriminating lung's nodules from other dense structures by using volumetric space of the thorax. Where, the achieved false positive rate was 8.5 per exam. Fetita, Preteux (10) applied a three-dimensional active contour method to segment 96 lung's nodules, then the texture features were extracted and classified into classes by a linear discriminant analysis (LDA). Ozekes and Osman (11) suggested a CAD system based on volumetric CT scans of lung to detect lung's nodules which have diameters (3.5–7.3) mm. In this study, four classifiers were used to evaluated the suggested system.

Furthermore, El-Baz, Elnakib (12) exploited the efficacy of genetic algorithm (GA) to isolate nodules, arteries, veins, bronchi and bronchioles from the surrounding anatomical structures based on volumetric and two-dimensional CT lung scans. It was proved that the lung nodules were recognized precisely when using volumetric CT scans. In this study, it was noted that the false positive rate was reduced significantly when utilizing volumetric CT scan of lung compared to two-dimensional CT scan. The achieved sensitivity and false positive rates were 82.3 % and 9.2 % respectively.

In this study, we proposed a new system to describe automatically lung's lesions in volumetric CT scans, as well as, determining the nodule numbers, type location, shape, progress of lesion. The main contribution of this study is to discriminant the complicated lung's nodules that have non seen through the clinical routine. A successful system can improve the accuracy of the diagnosis process. The following research objectives focus on how the above aim will be achieved:

– to extract the most distinct characteristics of the lung's nodule to that helps to determine treatment decisions and predict expected outcomes;

– to detect the complicated lesions cases that cannot be identified with certainty by radiologists;

– constructing an efficient CAD system that can determine precisely lung's nodules number and types.

The rest of this paper is organized as follows. In Section 2, material and method will be described and the conclusion will be discussed in Section 3.

Materials and Methods. The core-aim of the present study was to build an automated algorithm of clustering nodules from CT lung scans in an axial plane. The proposed algorithm is divided into three stages as shown in Fig. 1. First, the CT lung scan undergoes an enhancing process and separating of lung from background in the pre-processing stage. Then, the CT lung scan is clustered in 2D and 3D for detecting the vessel and nodules from normal tissue in the post-processing stage, as well as reducing the area region about nodules in 2D clustering while describes the nodule shape in 3D clustering. The results of 3D clustering are evaluated using two ways (3D-DBSCAN method and Plot.ly application). The evaluation stage confirms the outcomes precision of previous stage (post-processing) in detecting the number and shape of nodules that founded in the complex case, which is recorded in radiologist's report.

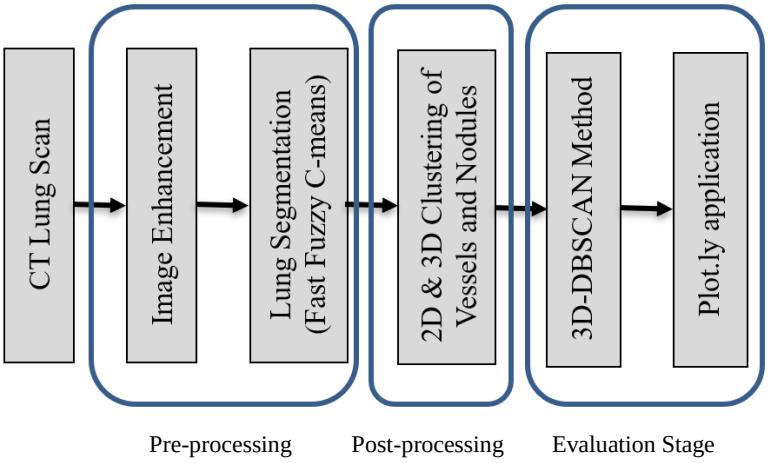

Fig. 1. The Proposed Model of Lung CT scan Clustering

Data Collection This study included 85 lung CT scans with pulmonary nodules, were downloaded from the TCIA (Cancer Imaging Archive) website (13). The provided data was annotated and screened by four radiologists to determine and extract the diagnostic details of lung's nodules such as number, size, location, volume, diameter, type of lung's nodules. In addition to slice number of the pathological lung. Figure 2, shows samples of CT lung scans form the provided dataset in axial viewing.

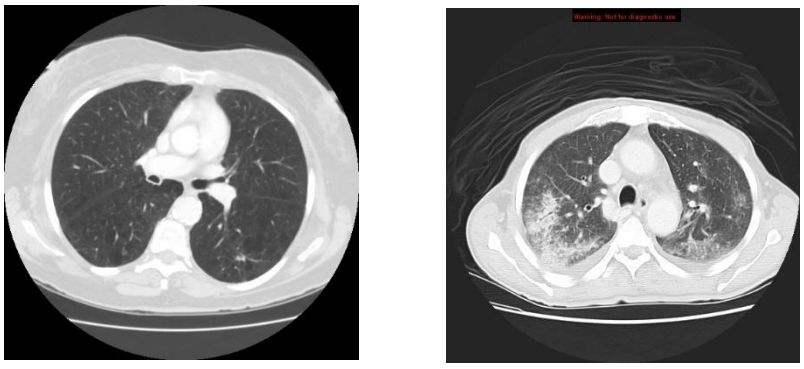

a) *b*)

Fig. 2. Lung CT slices in the axial view: *a* — healthy CT lung scan; *b* — pathological CT lung scan

Pre-processing of Lung CT Scan. To reconstruct the CT images, a million of independent detectors are used to collect the x-ray signals. Subsequently, the CT artifacts may be occurred during the reconstruction process. Where, these artifacts cause intensity variations across consecutive re-constructed CT scan slices. Therefore, the lung CT scans are pre-processed by implementing a set of algorithms such as image enhancement by gaussian filter, intensity normalization by histogram normalization method, lung extraction by thresholding (1, 14) as shown in Fig. 3.

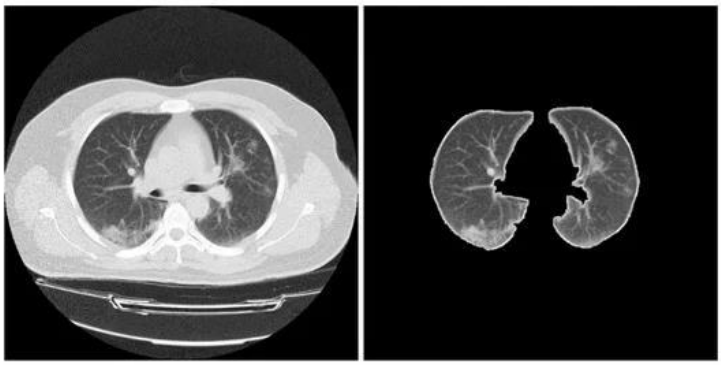

Fig. 3. Lung boundary identification samples: *a* — Original CT image; *b* — Preprocessed CT image

Three-dimensional Clustering. In this step includes implementation of a set of image pre-processing methods to prepare the CT scans of lung more appropriate for implementing the K-mean clustering method. Where, reduction of parenchyma tissue was achieved by isolating the intensity values that represents the vessels and nodules together. Then, vessels and lung's nodules were separated by implementing the K-mean clustering method on each CT image separately. It is an efficient and non-supervised technique that allows the cluster center to shift and fit the ROI (15–17). Subsequently, any hole appearing in the clustered CT scan of lung is removed by implementing a set of morphological operations (1). Then, the clustered CT images of each patient were stacked into single a volumetric CT scan and underwent the 3D graphics functions later.

Finally, a three-dimensional volume reconstruction from cross-sectional CT scans is determined by using isosurface function which was provided by MATLAB and used to measure the geometric computations of clustered data, and improved volumetric visualization of objects. Where, pixel coordination (x,y,z) and intensity values of pixel of each cross-sectional clustered scan was given as input to the function. Moreover, isocaps and isonormal functions were used to enhance produced the three-dimensional representation of the lung's nodules and vessels. Consequently, the three-dimensional clustering stage detects nodules, shape, type, and progress and finds out the unseen lesions in the CT scan of lung. The suggested algorithm was applied to cluster nodules and vessels in volumetric CT scan of lung.

First step was the threshold, where each value of the intensity in the volumetric CT scans by a specific value to extract correctly the lung's nodules from the CT scan of lungs by using Eq. 1.

$$\mathrm{G}(x,y) = \begin{cases} 1 & \text{if } \mathrm{P}(x,y) > \mathrm{T} \\ 0 & \text{Otherwise} \end{cases} \quad (1)$$

Where, $P(x,y)$ indicates the intensity values representing the nodules and vessels which are greater than the threshold value which is set experimentally.

The second step used K-means clustering on each CT lung images individually to eliminate any undesirable holes that occurred in the clustering process. The output of clustering process was labelling pixels of CT images into two main clusters (nodules and vessels). K-means clustering implemented by using the following steps.

1. Initialize k to specify cluster center, C=c_1, c_2,..c_k.

2. Determining the distance between CT lung image's pixels and the cluster centers by using Eq. 2:

$$S = \sum_{i=1}^{m} \sum_{j=1}^{n} || x_i - c_j ||^2 \quad (2)$$

where, x_i is an intensity pixel associated with m and n coordinates.

3. Assigning the CT lung's pixel with minimum distance to the nearest cluster's center.

4. Updating the cluster centers according to Equation (3):

$$\mathrm{C_i} = \frac{1}{\mathrm{N_{i,j}}} \sum_{\mathrm{j=1}}^{\mathrm{N_{i,j}}} \mathrm{x_{i,j}} \quad (3)$$

where, c_i and $N_{i,j}$ indicate the i^{th}cluster center, and all pixels of the i^{th} cluster respectively. While, $x_{i,j}$ signifies all pixels of i^{th} cluster center.

5. Repeating steps 2 to 4 until minimizing the objective function S to the lowest value.

Finally, implemented a three-dimensional function on the labelled clusters of CT images to generate the volumetric data. Where, the volumetric data was plotted according to a set of calculations. The following procedure was used to combine the labeled clusters and produce lung's nodule's shape and type (18). Algorithm 1 shows the pseudo-code for the generating of volumetric lung's nodule steps.

Algorithm 1: Pseudo-code for generating of volumetric lung's nodule.

Input: Clustered image (x.y.z).
Output: Output volumetric figure (i,j,k).
Begin
Apply *Isosurface* function to present a volume visualization.
Apply *Isocaps* function to adjust colors of faces of the produced volumetric lung's nodules.
Apply *Azimuth* and *Elevation* functions to create axes in three-dimensional view.
Apply *Isonormals* to determine the normal vertices and create a surface shadow through vertices gradient.

Results. The plotted three-dimensional space of lung's nodules enhanced visualization of nodules and vessels and provided more descriptions on the lung's nodules than what extracted by two-dimensional space. Where, the former provides more details regarding shape and locations of lung's nodules. Figure 4, shows an example of pathological lung that has two nodules with a red referral that are appear between slices no. 60 and 64. After implementing the three-dimensional clustering, a thin tissue between lung's nodules that is invisible by two-dimensional clustering, becomes visible to the radiologists. Furthermore, it extends through CT slices no. 61 to 63. Therefore, by depending on the two-dimensional clustering leads to make the inspection process by the radiologist prone to error and may diagnose one lung's nodule as two separated nodules.

Moreover, the proposed system provides more details about the lung's nodule type. Where, each lung's nodule was classified into juxta-vascular and juxta-pleural nodules. Figure 5, reveals how an early lung's nodule was detected and notified and this will help the clinicians to improve patient survival rates. Figure 6 shows how the lung's nodules are connected through their center pixels.

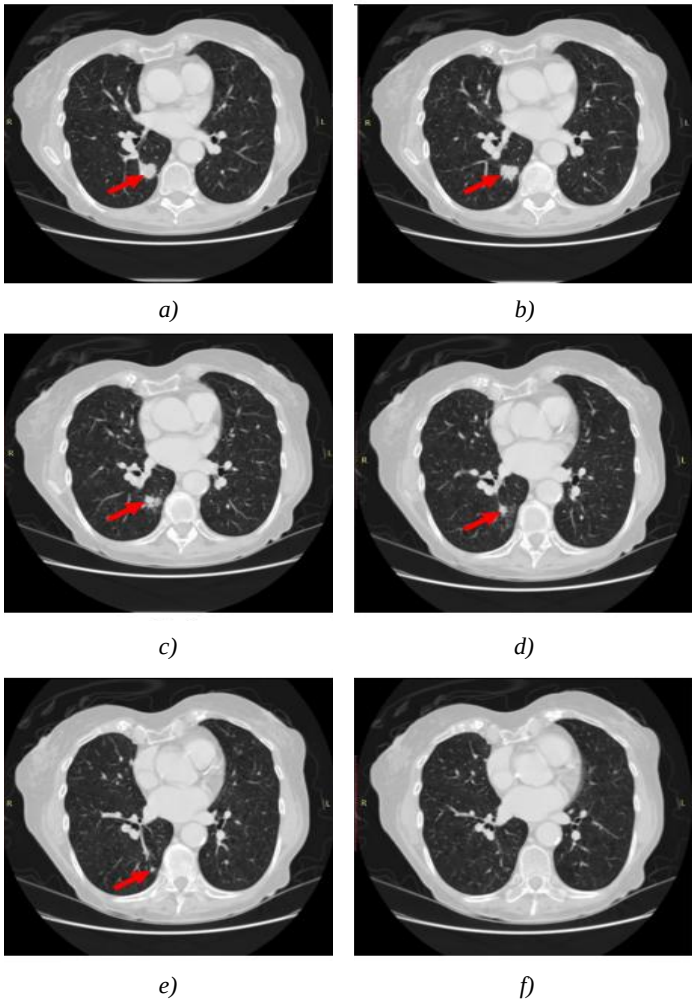

Fig. 4. Original CT Lung scan between Slice 60 and 64 with a Red arrow to indicate Two Attached Nodules: *a* — Candidate Nodule in the 60th slice; *b, c, d* — lung Nodules through slices 61, 62, 63; *e* — Nodule in slice 64; *f* — Normal slice after slice 65

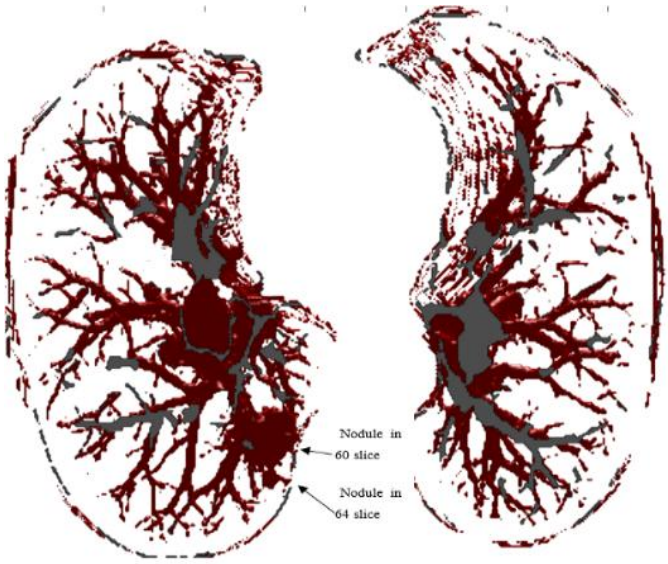

Fig. 5. Three-dimensional Clustering of CT lungs Attached Nodules in 60th and 64th Slices

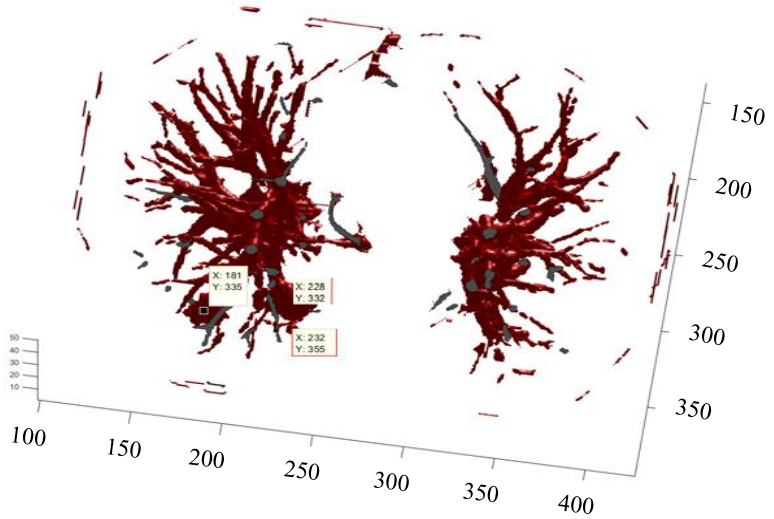

Fig. 6. Three-dimensional Clustering of two lung nodules that are located in different slices

Although the three-dimensional graphic is evaluated visually, it is essential to evaluate quantitively the quality of the achieved results. The Density-based spatial clustering of applications with noise (DBSCAN) method and 3D plot.ly application were used to evaluate the performance of the proposed three-dimensional clustering method (19, 20).

The DBSCAN method is one of the most popular and standard clustering techniques (21–23). It was used to set of nearby pixels are grouped to gather into a single cluster, and isolate the outlier pixels in a low-density area. The clustering process of this method depends on two key parameters (Epsilon and MinPts) that deal with core point in the volumetric space. Where, Epsilon is the distance that specifies the neighborhoods. Two points are considered to be neighbors if the distance between them is less than or equal to eps. While, MinPts represents minimum number of data points to define a cluster. Then, a point is considered as a core point if there are at least MinPts number of points (including the point itself) in its surrounding area with radius eps.

DBSCAN method was modified to cluster the volumetric CT lung scans to compare its output with the proposed system in this study by comparing the cluster's centers that were achieved by both methods. Where, DBSCAN inspects and connects all objects to the core pixels based on eps and MinPts measures. Synchronously, all the points that do not

represent core points are ignored. Many advantages are achieved by using this method, first, no need to initialize cluster numbers like k-means cluster method. Secondly, random shaped clusters are discovered easily. Finally, if the data is fully understood, it is easily to specify the MinPts and ets parameters.

Fig. 7 shows how the lung's nodules were linked through CT slices. Where, the 3D-DBSCAN method evaluated the connection between attached nodules compare with the clustered lung's nodules of the proposed system in this study. It is noted that the center's pixels were approximately matched as shown in Fig. 8. Fig. 9, shows how the lung's nodules were linked and spread by a thin line between CT slices no. 60th and 64th.

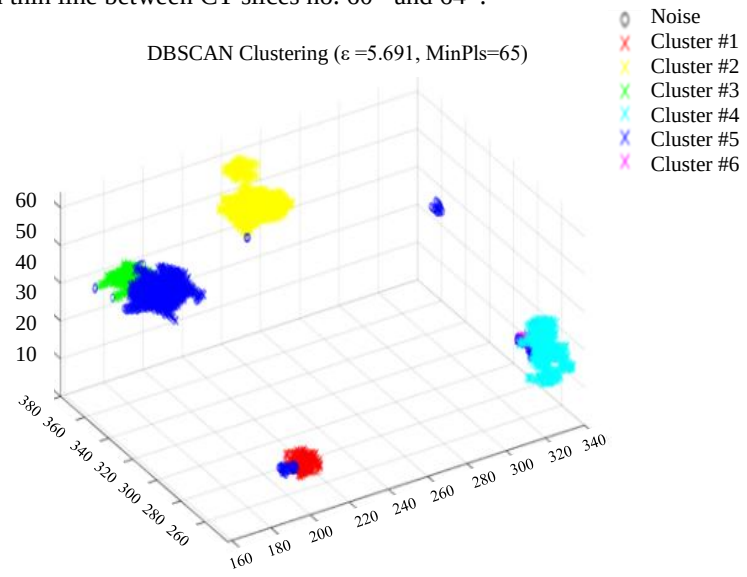

Fig. 7. 3D-DBSCAN clustering Method, yellow cluster refers to Linked Nodules, and other colors refer to the Remaining Nodules of the Same Patient

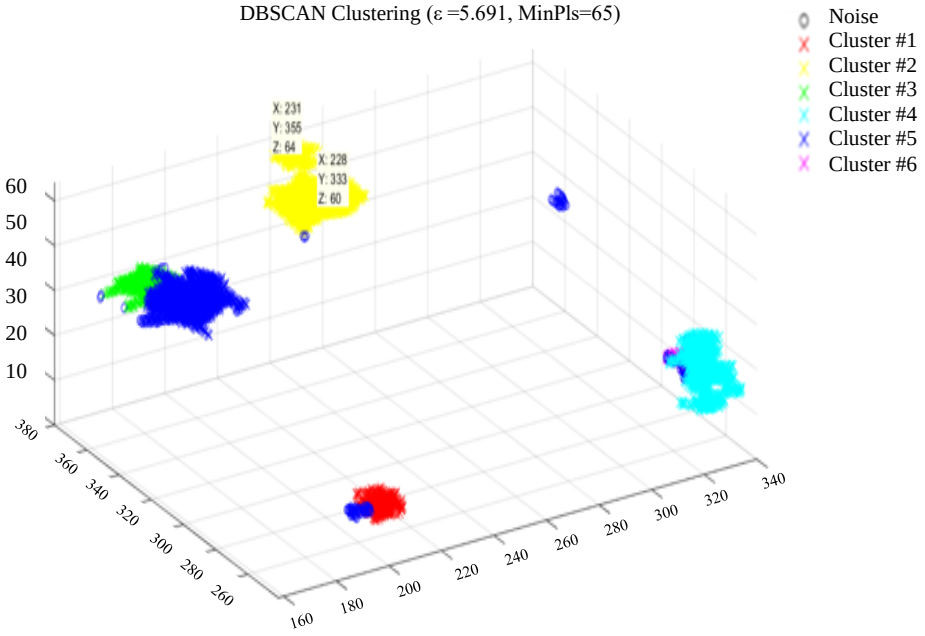

Fig. 8. 3D-DBSCAN clustering Method, yellow cluster refers to the Linked Nodules, Centers Pixels were recognized by Radiologist, and other colors refer to the Remaining Nodules

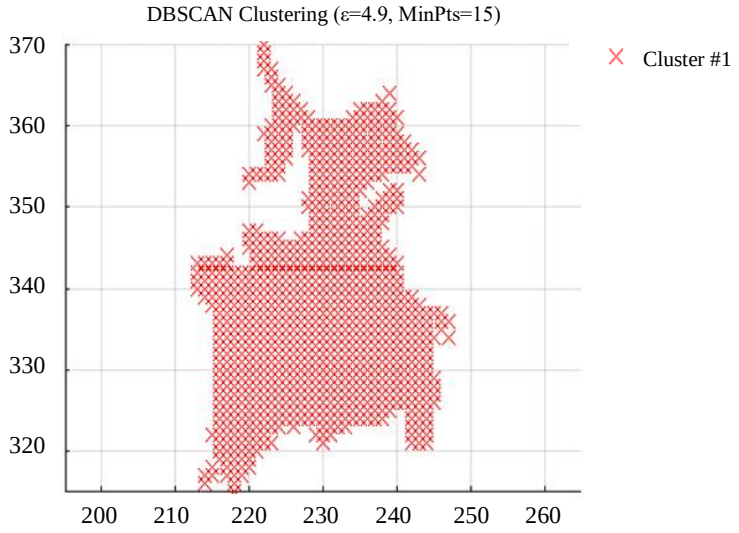

Fig. 9. DBSCAN Method Just Clusters the Linked Nodules and Proves One Nodule

Another 3D application was utilized in this study to evaluate the proposed system. It is named plot.ly application. This application used colored bubbles to locate pixels within the candidate nodule and its structures in different slices, as shown in Fig. 10 and Fig. 11. It was initialized by the coordinates of lung's nodules centers and it extended consecutively through similar structures in neighbor CT slices. Moreover, it was essentially to initialize pixel size and pixel spacing of CT scan, which are determined by Eq. 4 and Eq. 5.

$$\text{Pixel spacing}(\text{x}-\text{size},\text{y}-\text{size}) = \left(\frac{(\text{Field of view(FOV)})}{(\text{Matrix Size})}\right)^2 = \left(\frac{360mm}{512}\right)^2 = 0.703^2 \quad (4)$$

$$voxel\ size = pixel\ spacing(x-size) \times pixel\ spacing(y-size) \times thickness = 0.703 \times 0.703 \times 2.5 = 1.235 \quad (5)$$

Where x and y indicate the distance from the center of one pixel to the center of an adjacent pixel in the X and Y axes respectively. It is determined by squared ratio of the CT image field of view to the image array size (512×512). The image parameters of the provided dataset; pixel spacing, thickness, and voxel size were (0.703/0.703), 2.5 and 1.235 respectively. Fig. 12, shows the centered pixels of lung's nodules were labeled with two colors: red and green that represented actual center that was recognized by radiologist and the determined center by the proposed system. The black and blue colors show the overlapped area between clusters in different slices, and the remaining pixels of the cluster areas respectively. Generally, the plotted volumetric lung's nodules by the Polt.ly application and 3D-DBSCAN methods proved the efficacy of the suggested system in this study. Where, all used methods described accurately the connected regions between linked nodules in CT lung scans.

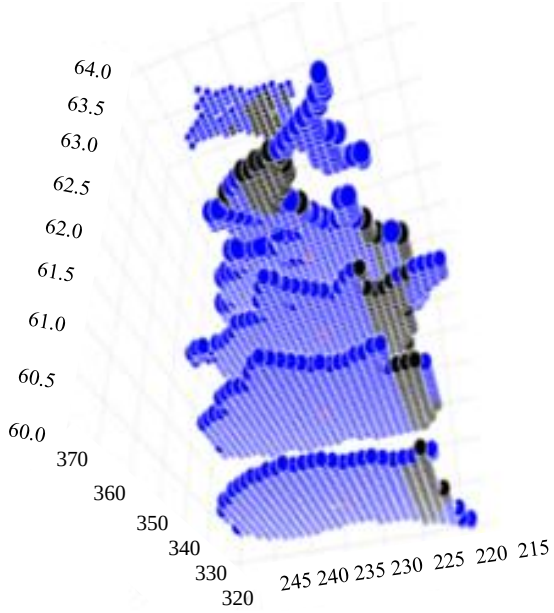

Fig. 10. Three-dimensional Plot of lung's Nodules was distributed on Different Levels from Slice 60 to 64

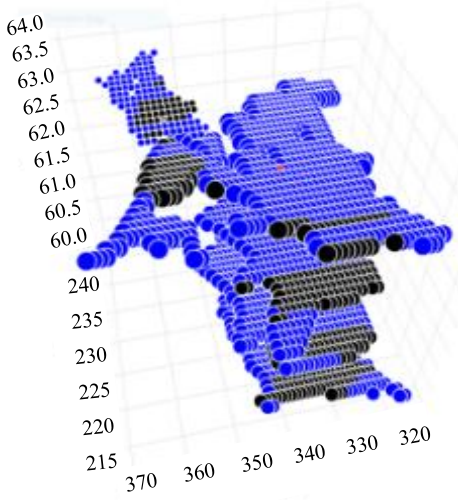

Fig. 11. Three-dimensional Plot of lung's nodule of the same case in Fig.10 but from different view, Black Bubbles Represent the Overlapping between Nodules to Show the Connected Regions

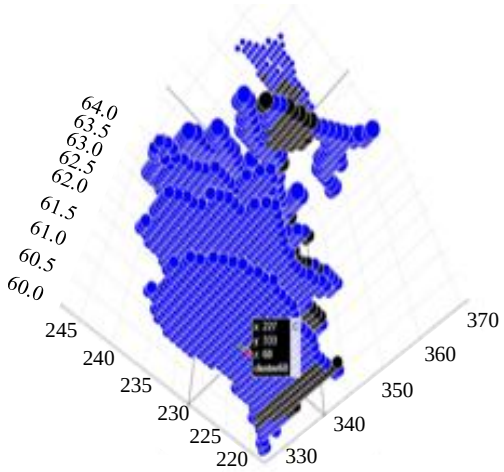

Fig. 12. The Overlapping between Centre Pixels of Clustered and Actual Nodule in the 60 Slice with Two Colors Red and Green Respectively

Discussion and Conclusions. The main objective of this paper was to build and implement a fully automated algorithm to describe the pulmonary nodules in CT lung images regarding shape and location matching the radiologist's report. The proposed method could cluster the nodules and showed their shape, location, type, and progress within the lung organ. The final algorithm outcomes and case study were evaluated by other 3D clustering methods emphasizing the accurate research results. This work is performed within several stages, with different methods are used for this purpose. Firstly, threshold and K-means clustering segment the nodules and vessels of CT lung images as objects with high intensity in 2D images. With 3D function, the 2D clustered images are stacked to display the nodule progress in 3D view. The algorithm results were validated by matching the center pixels of detected nodules by 3D Clustering and actual nodules reported by radiologists. In addition, the study identified a complicated case in the data, which is suspected the radiologists may miss because it was invisible. In this case, the algorithm proves and shows an attachment between two nodules making the nodules as one nodule against the radiologist's report. The evaluation stage has been done by applying the 3D-DBSCAN and 3D application methods, which confirm the proposed method results precision for this work. The Clustering of 3D-DBSCAN demonstrates the number and location of nodules and reflects the nodule shape as far as to describe the type of nodule. Also, determining this case confirms the work abilities in the early detection of nodules, which provides a chance for recovery patient. Our algorithm has a promising result on the standard data of CT scan images in detecting the number and location of nodules, which correspond to radiologist report, and automatically providing nodule shape and type.

References

1. Hasan AM, AL-Jawad MM, Jalab HA, et al. Classification of Covid-19 Coronavirus, Pneumonia and Healthy Lungs in CT Scans Using Q-Deformed Entropy and Deep Learning Features. Entropy. 2020;22:517.

2. Magdy E, Zayed N, Fakhr M. Automatic Classification of Normal and Cancer Lung CT Images Using Multiscale AM-FM Features. International Journal of Biomedical Imaging. 2015;2015. http://dx.doi.org/10.1155/2015/230830

3. Hasan AM, Meziane F, Jalab HA (eds). Performance of Grey Level Statistic Features versus Gabor Wavelet for Screening MRI Brain Tumors: A Comparative Study. International Conference on Information Communication and Management (ICICM); 2016; UK: IEEE.

4. El-Bana S, Al-Kabbany A, Sharkas M. A Two-Stage Framework for Automated Malignant Pulmonary Nodule Detection in CT Scans. Diagnostics. 2020;10:131. http://dx.doi.org/10.3390/diagnostics10030131

5. Valente IRS, Cortez PC, Neto EC, et al. Automatic 3D Pulmonary Nodule Detection in CT Images: A Survey. Computer Methods and Programs in Biomedicine. 2016;124:91–107. https://doi.org/10.1016/j.cmpb.2015.10.006

6. Lederlin M, Revel M-P, Khalil A, et al. Management Strategy of Pulmonary Nodule in 2013. Diagnostic and Interventional Imaging. 2013;94:1081–1094. https://doi.org/10.1016/j.diii.2013.05.007

7. Netto SMB, Silva AC, Nunes RA, et al. Automatic Segmentation of Lung Nodules with Growing Neural Gas and Support Vector Machine. Computers in Biology and Medicine. 2012;42:1110–1021. https://doi.org/10.1016/j.compbiomed.2012.09.003

8. Ma Z, Tavares JMR, Jorge RN (eds). A Review on the Current Segmentation Algorithms for Medical Images. Proceedings of the 1st International Conference on Imaging Theory and Applications (IMAGAPP); 2009.

9. Javaid M, Javid M, Rehman MZU, et al. A Novel Approach to CAD System for the Detection of Lung Nodules in CT Images. Computer Methods and Programs in Biomedicine. 2016;135:125–139. https://doi.org/10.1016/j.cmpb.2016.07.031

10. Fetita CI, Preteux F, Beigelman-Aubry C, et al. (eds). 3D Automated Lung Nodule Segmentation in HRCT. International Conference on Medical Image Computing and Computer-Assisted Intervention; 2003: Springer.

11. Ozekes S, Osman O. Computerized Lung Nodule Detection Using 3D Feature Extraction and Learning Based Algorithms. Journal of Medical Systems. 2010;34:185–194. https://doi.org/10.1007/s10916-008-9230-0

12. El-Baz A, Elnakib A, El-Ghar A, et al. Automatic Detection of 2D and 3D Lung Nodules in Chest Spiral CT Scans. International Journal of Biomedical Imaging. 2013;2013:517632. https://doi.org/10.1155/2013/517632

13. Bloch BN, Jain A, Jaffe CC. Data From BREAST-DIAGNOSIS. In: Archive TCI, ed. http://doi.org/10.7937/K9/TCIA.2015.SDNRQXXR2015

14. Hamid A Jalab, Rabha W Ibrahim, Ali M Hasan, et al. Medical Image Enhancement Based on Statistical Distributions in Fractional Calculus. IEEE Computing Conference 18-20 July 2017. United Kingdom, London; 2017.

15. Peter VJ, Karnan M. Medical Image Analysis Using Unsupervised and Supervised Classification Techniques. International Journal of Innovative Technology and Exploring Engineering. 2013;3:40–45.

16. Rajaraman A, Ullman JD. Mining of Massive Datasets. Cambridge University Press; 2011.

17. Celebi ME, Kingravi HA, Vela PA. A Comparative Study of Efficient Initialization Methods for the K-Means Clustering Algorithm. Expert Systems with Applications. 2013;40:200–210. https://doi.org/10.1016/j.eswa.2012.07.021

18. Smith ST. MATLAB: Advanced GUI Development. Dog Ear Publishing; 2006.

19. Bankman I. Handbook of Medical Image Processing and Analysis. Elsevier; 2008.

20. Papademetris X, Joshi A. An Introduction to Programming for Medical Image Analysis with the Visualization Toolkit. Yale University. 2006;283.

21. Sander J, Ester M, Kriegel H-P, et al. Density-Based Clustering in Spatial Databases: The Algorithm GDBSCAN and Its Applications. Data Mining and Knowledge Discovery. 1998;2:169–194.

22. Kriegel HP, Kröger P, Sander J, et al. Density-Based Clustering. Wiley Interdisciplinary Reviews: Data Mining and Knowledge Discovery. 2011;1(3):231–240. https://doi.org/10.1002/widm.1343

23. Schubert E, Sander J, Ester M, et al. DBSCAN Revisited, Revisited: Why and How You Should (Still) Use DBSCAN. ACM Transactions on Database Systems (TODS). 2017;42(3):1–21. https://doi.org/10.1145/3068335

Received 08.08.2022
Revised 28.08.2022
Accepted 06.09.2022

About the Authors:

Al-Funjan, Amera, Lecturer in Mathematics Department, College of Pure Sciences, Babylon University (PO Box 4 Hilla City, Babylon, 51001, Iraq). Ph.D, ResearcherID, ORCID, amera.alfunjan@uobabylon.edu.iq

Meziane, Farid, College of Science and Engineering, School of Computing and Engineering, University of Derby (DE22 1GB, Derby, UK), Ph.D, ScopusID, ORCID, f.meziane@derby.ac.uk

Aspin, Rob, Deputy Head, Manchester Metropolitan University, (M15 6BH, Manchester, UK), Ph.D, ScopusID, ORCID, R.Aspin@mmu.ac.uk

Claimed contributorship:

A. Al-Funjan: conception, design and drafting the manuscript and acquisition of data and analysis. F. Meziane: interpretation, revision and proofreading. R. Aspin: formal analysis.

Conflict of interest statement

The authors do not have any conflict of interest.

All authors have read and approved the final manuscript.

INFORMATION TECHNOLOGY, COMPUTER SCIENCE, AND MANAGEMENT

UDC 625.7/8
https://doi.org/10.23947/2687-1653-2022-22-3-272-284

Original article

Evaluation of Pavement Condition Deterioration Using Artificial Intelligence Models

Mohamed Mostafa Mahmoud Elshamy[1,2], Artem N. Tiraturyan[1] ✉, Evgeniya V. Uglova[1], Mohamed Zakaria Elgendy[2]

[1]Don State Technical University, 1, Gagarin sq., Rostov-on-Don, Russian Federation
[2] Al-Azhar University, 1, Al Mokhaym Al Daem St., Cairo, Nasr-City, Arab Republic of Egypt
✉ tiraturjan@list.ru

Abstract

Introduction. One of the most significant tasks facing road experts is to maintain the transport network in good condition. The process of selecting an appropriate approach to providing such condition is quite complex since it requires considering many parameters, such as the existing condition of the pavement, road category, weather conditions, traffic volume, etc. Recently, the rising trend of digitization in the industry has contributed to the use of artificial intelligence to address problems in several fields, including the bodies in charge of operational control over the status of roadways. Within the context of any control system, the main task of the control system is to carry out reliable forecasting of the operational state of the road in the medium and long term.

Materials and Methods. This study investigated the possibility of using artificial neural networks to assess existing pavement characteristics and their potential application in developing road maintenance strategies. A back-propagation neural network was implemented, trained using data from 1,614 investigated sections of the M4 "DON" highway in the road network of the Russian Federation in the period from 2014 to 2018. Several models were developed and trained using the MATLAB application, each with a different number of neurons in the hidden layers.

Results. The results of the models showed a convergence between the inferred paving state values and the actual values, as the multiple correlation coefficient (R^2) values exceeded 92 % for most of the models during all learning stages.

Discussion and Conclusions. The findings suggest that public road authorities may utilize the established models to choose the best road maintenance strategy and assign the most efficient steps to restore road bearing capacity and operation.

Keywords: artificial neural network, back-propagation algorithm, falling weight deflectometer test, pavement maintenance, pavement management system.

Funding information. The research is done on the grant of President of the Russian Federation for state support of young Russian scientists – candidates of science (application МК–242.2022.4). Researcher Mohamed Mostafa Elshamy is funded by a fellowship under the executive program between the Arab Republic of Egypt and the Russian Federation. They have his thanks and appreciation.

For citation. M. M. M. Elshamy, A. N. Tiraturyan, E. V. Uglova, M. Z. Elgendy. Evaluation of Pavement Condition Deterioration Using Artificial Intelligence Models. Advanced Engineering Research, 2022, vol. 22, no. 3, pp. 272–284. https://doi.org/10.23947/2687-1653-2022-22-3-272-284

Introduction. Road infrastructure is one of the resources that are vital to any community, so it is necessary to think about ways to maintain its efficiency. However, roads deteriorate over time as a result of being subjected to various deterioration mechanisms [1]. As a result, it is essential to manage these resources strategically to maximize their service life and technical indicators while also lowering maintenance costs [2].

Pavement management systems (PMS) aid in the maintenance of pavement performance at an appropriate level for use and provide a variety of financial and social advantages. Moreover, it contributes significantly to the cleanliness of the surroundings during the usage or maintenance [3]. Accordingly, if the condition of the pavement network is allowed to deteriorate, the damages will not only increase the costs of road maintenance to raise their efficiency. But, it will cause environmental harm due to emissions and traffic noise, as well as expose travelers to the hazards of automobiles travelling on rough roads [4].

Due to the significant damage caused by the deterioration of roads, transportation agencies in various countries allocate a large part of their annual budget to the maintenance or rehabilitation of these damaged roads. The importance of maintenance planning work is to choose the appropriate time and method to reduce the rate of deterioration of pavement sections according to the available budget. To reach this goal, it is required to develop models that help improve the development process and take into account the factors affecting the maintenance decision making [5].

Multi-criteria models are commonly used in complicated decision-making situations, like those involving the network-wide maintenance of road infrastructure [6]. Multi-criteria models emerge as a scientific approach for evaluating multiple alternative interventions in the framework of road rehabilitation, taking into account the properties of pavement sections [7].

It is well recognized that a pavement's surfacing behavior reflects its condition; for this reason, pavement administrations depend on knowing the value of the PCI index through the process of visual inspection of the roads periodically in order to extend the life of the pavement and improve service levels [8]. The value of the pavement condition coefficient is one of the most significant factors based on which the most appropriate method of maintenance is determined, in addition to other factors, such as weather factors and traffic volume.

Over the last two decades, it has become clear that traditional knowledge of road maintenance is not enough, and there is an urgent need to develop new methods that help collect and process data for use in pavement management [9]. Due to the rapid development in the domains of information technology and artificial intelligence networks, many opportunities have been provided to find solutions to many problems in various fields, including road engineering.

Artificial neural network models are an application of the field of artificial intelligence used to solve non-linear geometric models, such as forecasting, recognition, and estimation of different patterns [10]. Artificial neural network models mimic the human brain's ability to solve issues using previous experiences. As a result, we can use this approach for choosing the most appropriate way to maintain the road after calculating its current or future condition instead of relying on human experience and knowledge.

Artificial neural networks (ANN) review:

Many studies focused on the possibility of using the artificial neural networks approach to determine the current and future state of the pavement to using it in the development of pavement management systems and determining the method of maintenance. We will mention some of these studies as follows:

R. Kumar, et al. created a neural network model for determining the condition rating of flexible pavements depending on pavement distress data collected. The study result appeared that the neural network was able to calculate pavement condition rating accurately [11].

Hamdi, et al. built an artificial neural network model using distress data generated from a visual assessment method to determine the Surface Distress Index. The positive modeling results showed that it could be used to determine the SDI coefficient [12].

After the results of the ANN models showed superiority in predicting the values of the pavement condition, many researchers were interested in developing models that can predict the values of pavement distress as an indicator of the pavement condition.

D. T. Thube used a neural networks approach to construct four models to predict pavement defects (cracking, rut depth, roughness, and raveling) as pavement condition indicators. The small differences between the observed and calculated distress values were evidence of the model's success [13].

L. Yao, et al. used a neural network approach to construct five models that predict five indicators of pavement distress: the transverse crack index, the skid-resistance index, roughness, the rut index, and pavement surface distress. The results of the models showed an acceptable performance in predicting the condition of the pavement, with an average testing R^2 of 0.8692 [14].

A. Shtayat, et al. [15], M. Mazari and D. D. Rodriguez [16] studied the possibility of predicting the International Roughness Index (IRI) based on distress data or different pavement performance indicators, such as traffic coefficients

and structural properties of pavement through neural network models or combined with gene expression programs or regression analysis. However, the results of neural network models showed an acceptable superiority compared to other methods.

A. M. Mosa suggested a neural network-based approach for diagnosing pavement distresses and optimizing solutions for maintenance techniques suggestions. The created system supplied the optimal solutions taking into consideration technological, economic, and environmental requirements [17].

The results of the mentioned literature review showed the ability of neural network models to represent the complex and nonlinear relationship between several variables. Therefore, it can contribute to solving road engineering problems. We also note the use of most previous studies of ANN models with an inverse propagation logarithm, and we will mention a summary of them in the following section.

Description of back-propagation artificial neural networks:

The back-propagation algorithm is one of the most widely utilized algorithms of artificial neural network models. It has a high capacity and speed in processing new data after conducting several iterations for a set of data during the education stage [18, 19].

The structure of the back-propagation algorithm for artificial neural networks consists of three or more layers, including the input layer, the output layer, and one or more hidden layers, as shown in Figure 1. The function of the neurons inside the input layer is to receive data and then pass it through the hidden layers, which have the ability to examine the correlations between variables and process the data to the output layer, which provides the results by the neurons in it [20] .

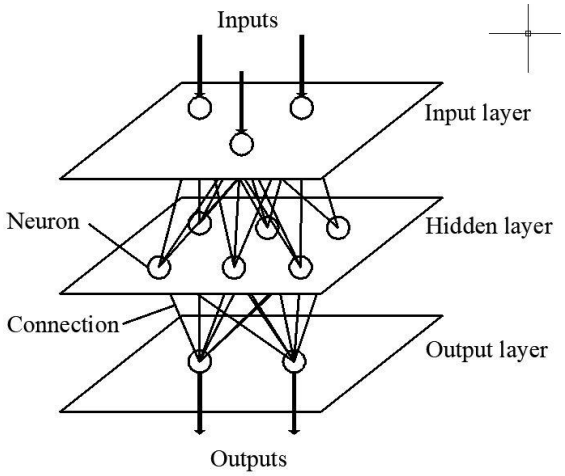

Fig. 1. Artificial Neural Network Construction Layers

In order for the neural network to perform the function assigned to it, the data must pass through three stages. The first is the process of training the network, in which it understands the effect of each variable and its relationship to other variables. Then we move on to the second stage, which is the validating process of the model, and finally, the network testing stage [21].

The back-propagation approach employs supervised learning, which implies that we supply examples data for the inputs and outputs to the network for learning [22]. The model assumes random weights for each variable and then passes the data forward to calculate the output. After calculating the difference between the computed output and the target values during the back pass, the weights are adjusted again to reduce the error rate and return the data from the output layer through the hidden layer to the input layer. The described learning process is repeated several times until the learning process is stopped when the error reaches an allowable value [19].

The weights determined during the training phase are employed in the testing process to calculate the output of a new input data set that was not used during the learning process. An evaluation of the ANN model is based on the amount of computed error.

The research scopes:

The study aims to use the field of artificial intelligence to build a model that helps engineers or decision-makers who prepare a road maintenance map to know the condition of the pavement without the need to conduct a periodic visual inspection. This reduces the dangers to individuals in charge of the examination process, as well as the effort, time, expense associated with it, and the errors that occur throughout the measuring procedure. To achieve this goal, we utilized the values of the deflection measurements coming from the falling weigh deflection test and the pavement condition index values from the Russian Road Company project for developing the M4 highway between the periods

from 2014 to 2018. We prepared a database for training and testing artificial neural network models by MATLAB software. The importance of this research is to accurately describe the future condition of the asphalt pavement to use the appropriate maintenance method to slow down the rate of asphalt deterioration.

Materials and Methods

Preparation of the database:

The data obtained for constructing the ANN model were collected from a study carried out by the Russian Road Corporation for developing the M4 highway between Moscow and Krasnodar. The available data includes inspection date, air temperature, asphalt layer thickness, base layer thickness, traffic volume, and precipitation rate and deflection values based on the falling weight deflectometer test.

The database was used to calculate three criteria that express the condition of the asphalt surface, which are the probability of success of the pavement sectors against the following three defects: fatigue, roughness, and rutting, as well as the modulus of elasticity of the pavement layers (asphalt layer, base layer, and subgrade layer) that were determined using a software package PRIMAX as input data and Regarding calculating the input parameter of "pavement surface life", it was determined by taking the difference between the deflection survey date and the date of construction or last rehabilitation date. Also, the initial pavement condition mentioned in the same study, represented by PCI values, was used as output data to train ANN models to predict PCI values.

Calculating pavement defects using the logistic model:

Non-destructive testing is an important approach for evaluating pavement structures and is widely accepted as a reliable way of determining the structural condition of existing pavements [23]. The falling weight deflectometer (FWD) is well-known for its effectiveness in determining the structural condition of pavement and assisting in defining the best treatment option possible, which reduces the deterioration of the pavement [24, 25].

The values expressing the resistance of the pavement sections to the above three pavement defects were calculated using the logistic model equations developed by the Federal Highway Administration Long-Term Performance (LTPP).

Equations 1 and 2 show the general formula, the linear formula, that were produced from the logistic model to calculate the three distress indicators of the pavement for all sectors used in building the ANN model.

Equation (1) described the general formula of the logistic model.

$$p(event) = \frac{1}{1 + e^{-b}} \quad (1)$$

Equation (2) described the calculation formula of the exponent term in the general linear.

$$b = a_0 + a_1 b_1 + a_2 b_2 + \ldots + a_n b_n \quad (2)$$

where p represents the probability of an event occurring, b represents the exponent variable and (a_0, a_1, a_2 ... a_n) are the constants of the variables of the linear equation.

The variables that influence pavement fatigue to determine the value of the parameter (b) are:

– D_1 denotes the deflection measured in the loading plate's midpoint;

– AADTT;

– the base layer type.

To compute the exponential component in equation (1), we utilized the variable values generated from the logistic model for pavement fatigue cracking in Table 1.

Table 1

The coefficients values utilized in the linear equation to calculate the condition of fatigue cracking

Variables (bi)	a_i	a_i = coefficient values of the equation. I_1 = The utilized deflection value's mutual index
I_1	154.764	
AADTT	–0.0005073	
Pavement type	0.3774	
Constant	–0.2202	

Equation (3) is used to find the variable I_1 [26].

$$I_1 = \frac{1}{D_1} \quad (3)$$

The variables that influence pavement roughness to determine the value of the parameter (b) are:

– D_2 is the measured deflection value at distance 200 mm from the center of the loading plate;

– the volume of trucks in the Class 9 classification;

– the pavement surface age from construction or from the latest maintenance.

To compute the exponential component in equation (1), we utilized the variable values generated from the logistic model for pavement roughness in Table 2.

Table 2

The coefficients values utilized in the linear equation to calculate the condition of roughness distress

Variables (*bi*)	a_i	a_i = coefficient values of the equation. I_2 = The utilized deflection value's mutual index.
I_2	239.849	
Current life	–0.189	
Class 9 volume	–0.0006781	
Constant	0.8375	

Equation (4) is used to find the variable I_2 [26].

$$I_2 = \frac{1}{D_2} \quad (4)$$

The variables that influence pavement rutting to determine the value of the parameter (*b*) are:

– D3 is the recorded deflection at a distance of 300 mm from the load plate's center;

– D4 is the deflection recorded at 450 mm from the load plate's center;

– the volume of trucks in the Class 9 classification;

– average annual precipitation in the zone area (mm).

To compute the exponential component in equation (1), we utilized the variable values generated from the logistic model for pavement rutting in Table 3.

Table 3

The coefficients values utilized in the linear equation to calculate the condition of rutting distress

Variables (*bi*)	a_i	a_i = coefficient values of the equation. CI_3 = Curvature index for the i^{th} deviations values.
CI_3	–0.01146	
Precipitation (mm)	–0.0005259	
Class 9 volume	–0.0007688	
Constant	2.6586	

Equation (5) is used to find the variable CI_3 [26].

$$CI_3 = D_3 - D_4 \quad (5)$$

Initial Database for Neural Networks

The database for entry in the neural network is comprised of a set of input data and a set of output data. The input data are the measured values of the following parameters: pavement surface life, asphalt layer thickness, base layer thickness, p(fatigue), p(roughness), p(rutting), the elastic modulus of (surface layer, base layer, and subgrade layer) shown as their mean value for an individual pavement segment. The model outputs are the pavement condition index values for the pavement sections that are available in the database. The goal of this database is the preparation and sorting of data in a format appropriate for entering it into the neural network.

Application of ANN

For the objective of this study, artificial neural networks with back-propagation algorithms and different numbers of neurons (8, 9, 10, 11, 12, 13, and 14) in two hidden layers were applied using the MATLAB software. The total quantity of inspection data utilized in the construction of the ANN model was 1,614 representing 51 different sectors along the M4 highway. The data used in the training process included the minimum and maximum values of the variables to increase the efficiency of the models.

The database was divided into three groups: a large amount of database in which the neural network conducts the learning process on 70 % of the randomly selected data; the second group represents the validation process with 15 % of the database; the remaining 15 % of the data for the third group was for testing the developed network. Figure 3 shows the configuration for one of the created neural networks during training.

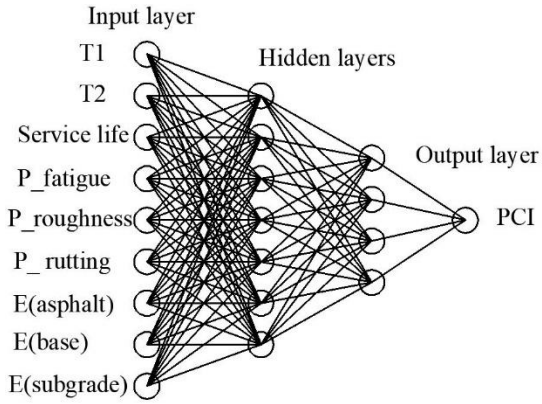

Fig. 2. The Applied ANN Model Structure

Each of the input parameters is represented by one of the nine neurons in the input layer. Eleven neurons are applied in the hidden layers, split into seven neurons in the first hidden layer and four neurons in the second layer. The output layer includes one neuron that represents the number of output data. The previous figure shows the direction of data transmission from the input layer to the output layer through two hidden layers and vice versa to correct the error rate in the output values until the permissible limit is reached.

Several numbers of layers and neurons inside the hidden layers were applied to increase the performance of the developed network. The training procedure was repeated several times until the optimal model that accurately expressed the relationship between the input and output data was found. The effectiveness of the trained models were compared using statistical analysis of the outputs, which were represented by the mean absolute error (MAE), and coefficient of multiple correlations (R^2), Root Mean Square Error (RMSE), and mean absolute percentage deviation (MARD).

Results. After the learning step, the neural network was subjected to testing. In the testing process, weights were fixed to values adopted at the end of the learning process. A new group of input and output data was offered to the network. Network output results were compared with required output and statistically analyzed.

The following regression and performance plots illustrate the output of the network models concerning training, validation, and test sets. Throw the training process, the optimal values of the network elements were carried out after 1,000 repetitions with (MSE = 0.0224). The best validation performance of the demonstrated model was 0.0344, which was achieved after 22 repetitions for the model with structure (9–10–1), as shown in Figure 3 (*a*, *b*). The optimal values of the network elements were carried out after 1,000 repetitions with (MSE = 0.0234). The best validation performance of the demonstrated model was 0.03171, which was achieved after 11 repetitions for the model with structure (9–11–1), as shown in Figure 4 (*a*, *b*). The low value of MSE of the selected models indicates that pavement conditions of roads in the same domain may be anticipated more accurately.

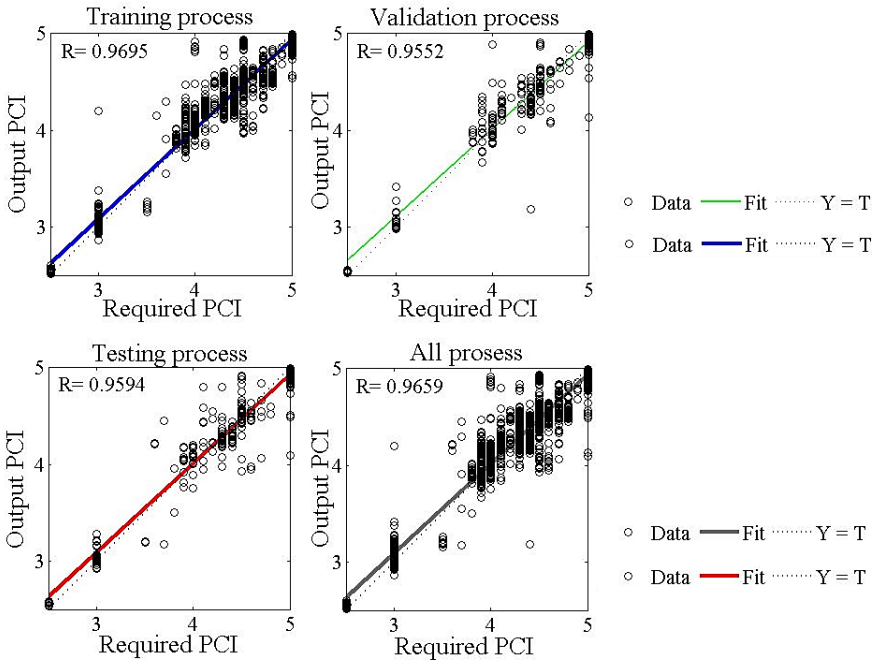

a)

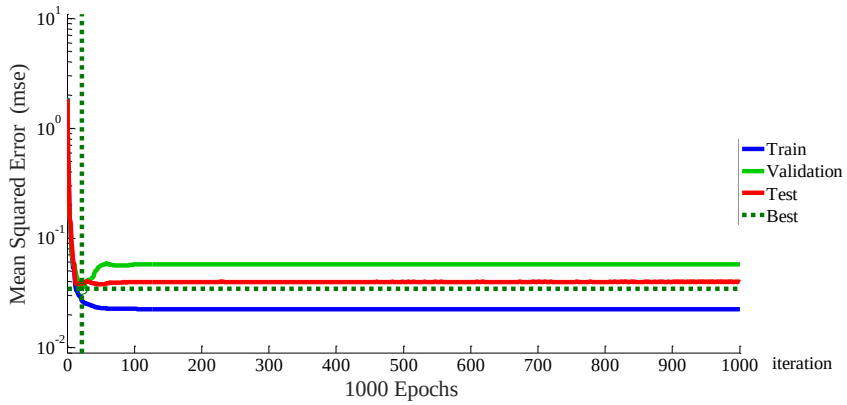

b)

Fig. 3. Results of training an ANN model with a structure (9–10–1): *a* — regression graphs; *b* — performance chart

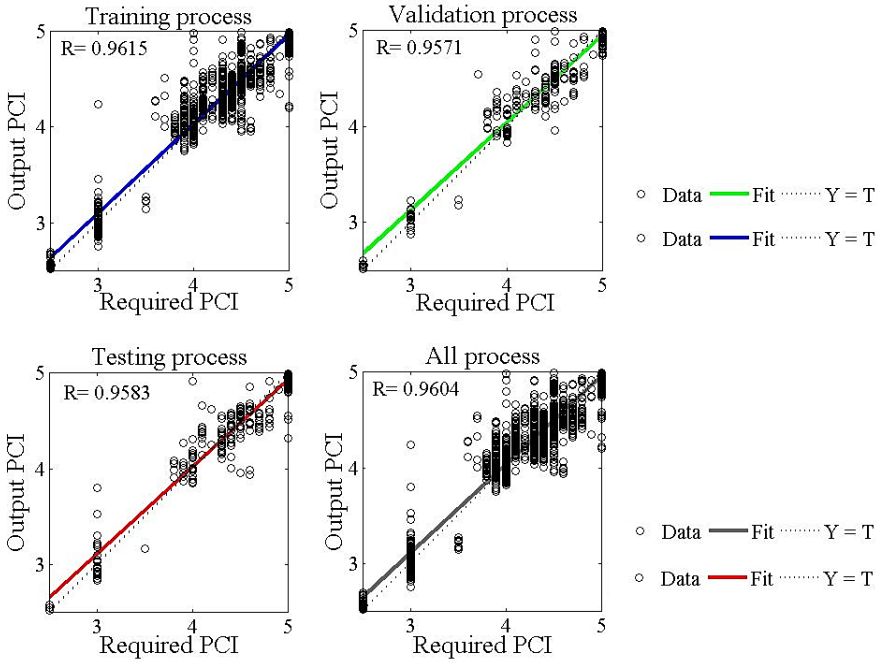

a)

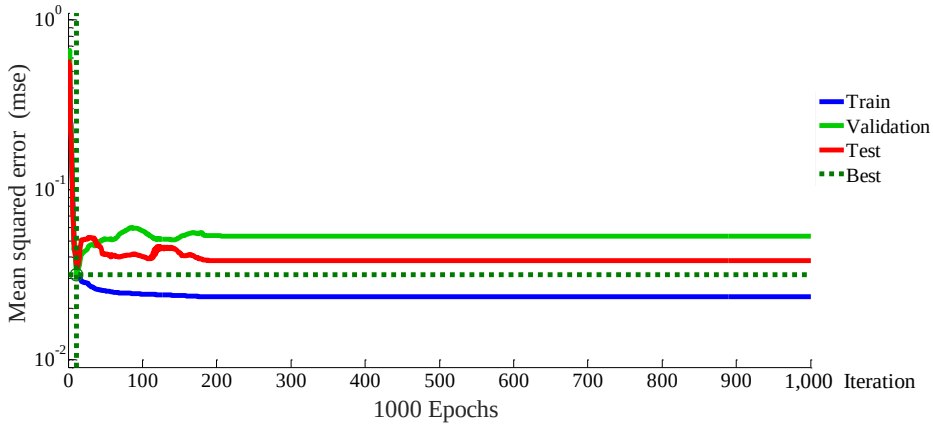

b)

Fig. 4. Results of training an ANN model with a structure (9–11–1): *a* — regression graphs; *b* — performance chart

According to the output results, notice a high correlation coefficient between the outcomes of the neural network computation and the needed outputs. There is a significant correlation between them where most of the data falls near a

45-degree line. As shown in the previous regression charts displayed for all stages, whether training, validation or testing phases, the correlation coefficients (R) values are greater than 95% for all stages, indicating the quality of the generated models and the ability to estimate the outputs correctly.

Evaluation of Artificial Neural Network:

The created ANN model may be saved as a MATLAB file once the training procedure is completed, and the desired accuracy is achieved. We can use it to do a forward computation and forecast pavement conditions for maintenance and rehabilitation purposes.

For this purpose, a new dataset of 37 sections was assigned to asphalt pavement to evaluate the ability of the developed neural networks used in the previous section to predict the output values. In this step the models were defined by input data for the specified parameter values, which were: (asphalt layer thickness, base layer thickness, surface life, p (fatigue), p (roughness), p (rutting), E (asphalt), E (base), and E (subgrade)). As a result, the created networks were able to anticipate output data (pavement condition index- PCI) based on early experience.

The criteria for choosing the best iteration for every model were: mean absolute error (MAE), coefficient of multiple correlations (R^2), Root Mean Square Error (RMSE), and mean absolute percentage deviation (MARD) of the estimates (PCI). They ensured that the predicted values were within reasonable data limits, as shown in Table 4. Figure 6 (*a*, *b*, *c*, *d*, *e*, and *f*) presents the relationship between the prediction results of the best iteration for every model with different numbers of neurons in the hidden layers, and the target output results.

Table 4

Statistical assessment of the created models' output (forecasted results)

Statistical comparison criteria	Pavement Condition Index – PCI						
	8n	9n	10n	11n	12n	13n	14n
MAE	0.1415	0.1242	0.1185	0.1317	0.1362	0.1594	0.1190
R^2	0.9204	0.9493	0.9451	0.9365	0.9342	0.8686	0.9483
RMSE	0.2058	0.1651	0.1710	0.1840	0.1862	0.2765	0.1666
MARE	3.4478	3.0430	2.8738	3.1545	3.2909	3.9488	2.9649

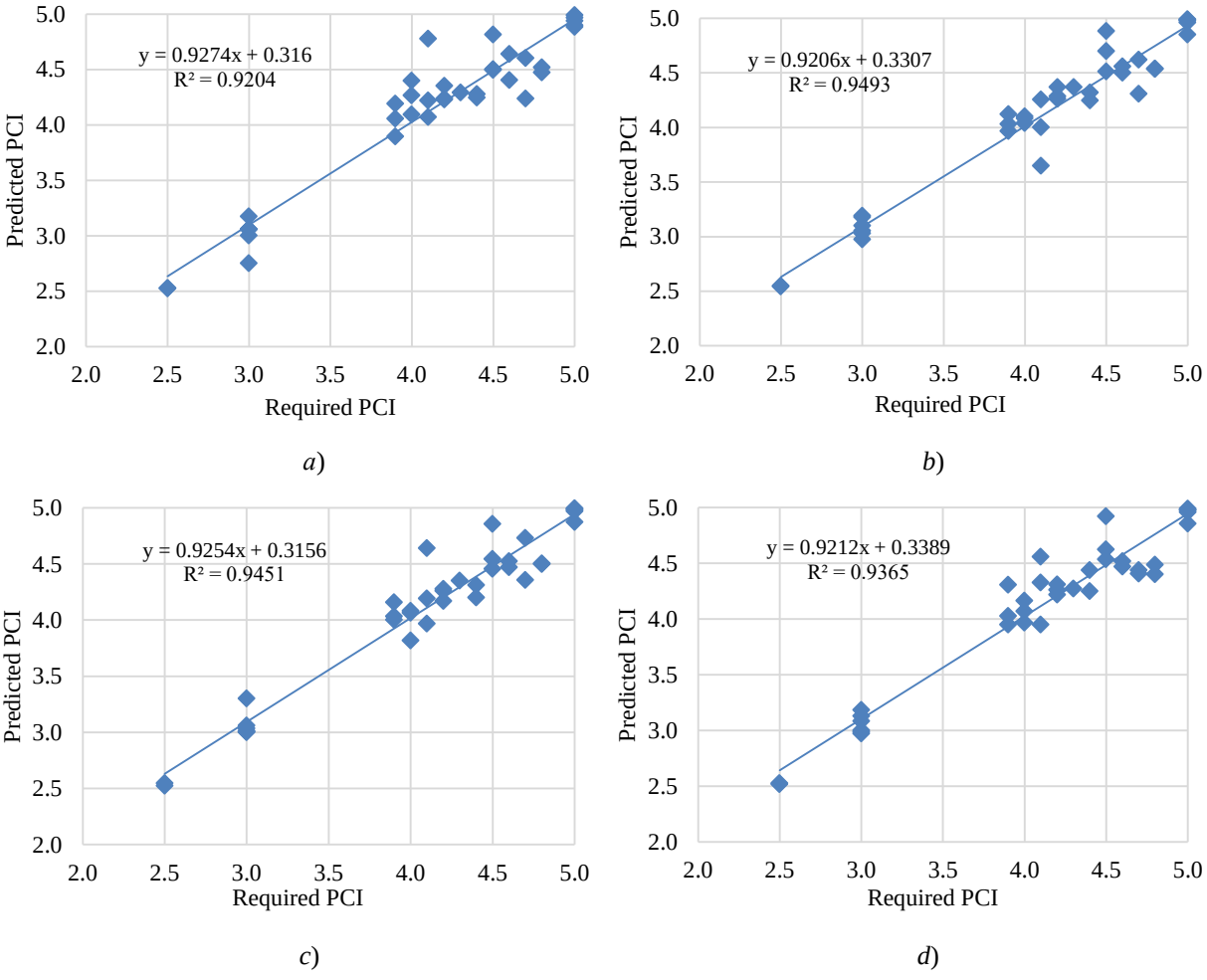

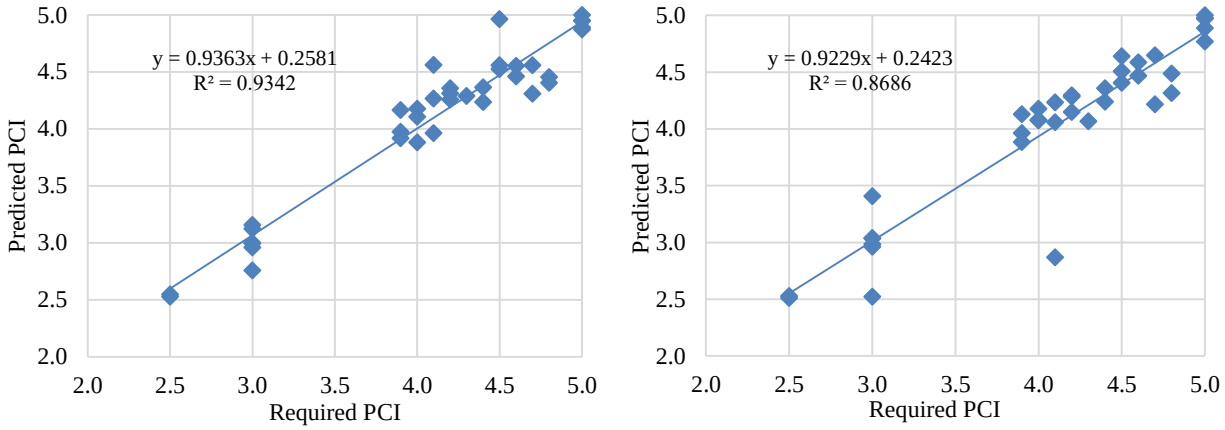

e) *f*)

Fig. 5. Relation between actual PCI and predicted PCI for all ANN models: *a* — model with 8 neurons; *b* — model with 9 neurons; *c* — model with 10 neurons; *d* — model with 11 neurons; *e* — model with 12 neurons; *f* — model with 13 neurons

Looking at the results of the statistical analysis of the outputs of the developed models represented in Table 4 and Figure 5 (*a*-*f*), we find that they have an acceptable ability to predict the condition of pavement based on the variables that were used in training the models. Also, notice that the best results were for two models with the structure (9–9–1) and (9–10–1), as they had the highest coefficient of multiple correlations (R^2), which is 0.9493, 0.9451, as well as the lowest values of MAE, RMSE, and MARE.

Evaluation of pavement deterioration via ANN model:

To recognize that the developed neural network models can help in predicting the rate of pavement deterioration, the idea arose to select several asphalt sectors and determine the effect of changing the operational life on the condition of each sector. To achieve this goal, each model defined the input values for each sector and fixed them, except for one variable, which was the operational life. Then we left the opportunity for the models to calculate the output values based on their previous experience. The sectors that were subjected to this experiment were numbers 504, 1227, 430, and 544, as shown in Figures. 6 (*a*, *b*, *c*, and *d*).

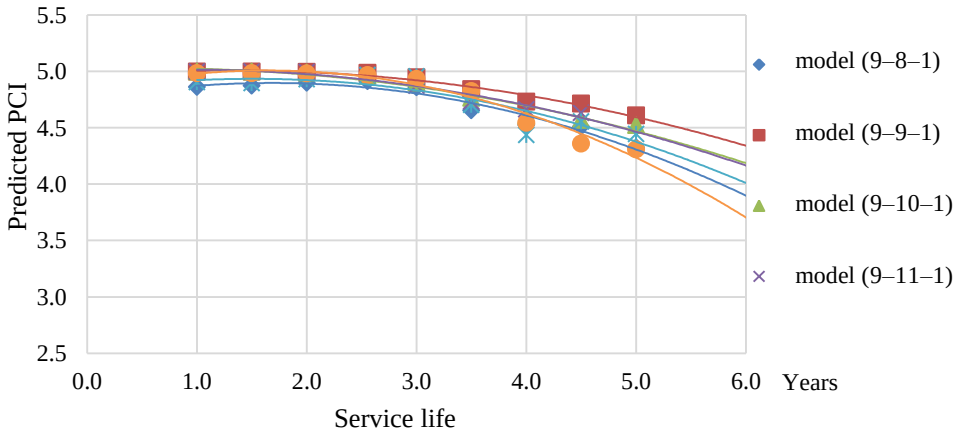

a)

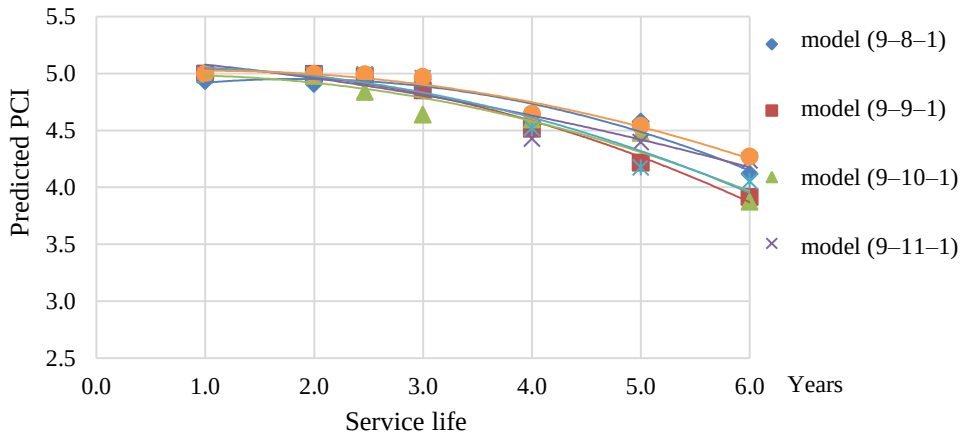

b)

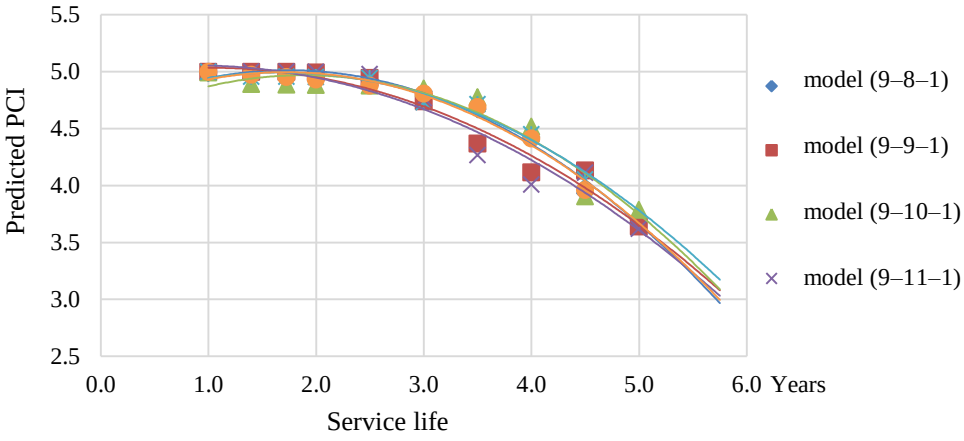

c)

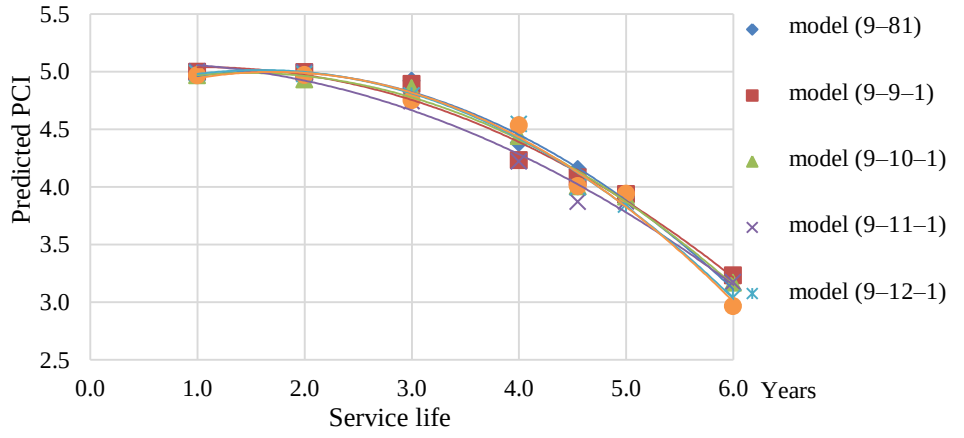

d)

Fig. 6. Pavement sections deteriorations against service life: *a* — deterioration of section no. 504; *b* — deterioration of section no. 1227; *c* — deterioration of section no. 430; *d* — deterioration of section no. 544

It is clear from the previous figures that the developed models have the ability to predict the condition of the asphalt as a result of the change in the service life. Where the value of the PCI reduces as the operational life increases, which is consistent with what happens in the field.

This research may help those in charge of developing a road maintenance plan in order to limit the deterioration of the pavement condition by anticipating the pavement condition in advance and intervening promptly by choosing the appropriate treatment method in proportion to the capabilities available to the authority entrusted with this matter.

Discussion and Conclusions. To achieve the objectives of this research, artificial neural network techniques were used to construct condition data deterioration models for pavement surfaces to assist decision-makers to choose the most efficient pavement maintenance solutions. Artificial neural networks (ANN) were utilized together with back-propagation algorithms to train the forecasting models for selecting appropriate options for treatment based on the value of the pavement condition index (PCI). A wide range of 1,614 cases of pavement condition description were provided

from previous investigations for various sectors of the Russian highway network to use as a database helping in creating the developed ANN models. Using MATLAB software, a large number of models with different numbers of neurons in the hidden layers were established, trained, and the results validated. The results of the models were studied, and the following conclusions were made:

– ANN models showed their ability to represent the nonlinear relationship between a large number of variables and the pavement condition coefficient with high accuracy, as indicated by the high value of the multiple correlation coefficient (R^2) for all stages of model learning (training, validation, and testing).

– According to models' validation, the variations between the actual PCI values and the predicted output results of the models were close to each other.

– Evaluation of models generated with different numbers of neurons in the hidden layers showed that they all assumed close patterns as well as similar flows of surface deterioration rates.

– The developed models save a lot of time and effort to determine the condition of the pavement and reduce the risks for the examiners compared to the visual examination method due to its dependence on the results of the dropped pregnancy test.

– The obtained results suggested that decision-makers might use the created modeling to optimize maintenance or rehabilitation methods for the most impacted roads to lower the rate of degradation based on available resources.

References

1. Schnebele E, Tanyu BF, Cervone G, et al. Review of Remote Sensing Methodologies for Pavement Management and Assessment. European Transport Research Review. 2015;7:1–19. https://doi.org/10.1007/s12544-015-0156-6

2. Jianyou Zhao, Xiaoyu Fu, Yunjiao Zhang J. Research on Risk Assessment and Safety Management of Highway Maintenance Project. Procedia Engineering. 2016;137:434–441. https://doi.org/10.1016/j.proeng.2016.01.278

3. Santero NJ, Horvath A. Global Warming Potential of Pavements. Environmental Research Letters. 2009;4:034011. https://doi.org/10.1088/1748-9326/4/3/034011

4. Schlegel T, Puiatti D, Ritter H-J, et al. The Limits of Partial Life Cycle Assessment Studies in Road Construction Practices: A Case Study on the Use of Hydrated Lime in Hot Mix Asphalt. Transportation Research Part D: Transport and Environment. 2016;48:141–160. https://doi.org/10.1016/j.trd.2016.08.005

5. Ameri M, Jarrahi A. An Executive Model for Network-Level Pavement Maintenance and Rehabilitation Planning Based on Linear Integer Programming. Journal of Industrial and Management Optimization. 2020;16:795–811. http://dx.doi.org/10.3934/jimo.2018179

6. Karleuša B, Dragičević N, Deluka-Tibljaš A. Review of Multicriteria-Analysis Methods Application in Decision Making about Transport Infrastructure. Građevinar. 2013;65:619–631. https://doi.org/10.14256/JCE.850.2013

7. Dabous SA, Zeiada W, Zayed T, et al. Sustainability-Informed Multi-Criteria Decision Support Framework for Ranking and Prioritization of Pavement Sections. Journal of Cleaner Production. 2020;244:118755. https://doi.org/10.1016/j.jclepro.2019.118755

8. Setyawan A, Nainggolan J, Budiarto A. Predicting the Remaining Service Life of Road Using Pavement Condition Index. Procedia Engineering. 2015;125:417–423. https://doi.org/10.1016/j.proeng.2015.11.108

9. Chengjia Han, Tao Ma, Guangji Xu, et al. Intelligent Decision Model of Road Maintenance Based on Improved Weight Random Forest Algorithm. International Journal of Pavement Engineering. — 2022. — Vol. 23. — P. 985–997. https://doi.org/10.1080/10298436.2020.1784418

10. Abiodun OI, Jantan A, Omolara AE, et al. State-of-the-Art in Artificial Neural Network Applications: A Survey. Heliyon. 2018;4:e00938. https://doi.org/10.1016/j.heliyon.2018.e00938

11. Kumar R, Suman SK, Prakash G. Evaluation of Pavement Condition Index Using Artificial Neural Network Approach. Transportation in Developing Economies. 2021;7:1–15. https://doi.org/10.1007/s40890-021-00130-7

12. Hamdi, Hadiwardoyo SP, Correia AG, et al. Prediction of Surface Distress Using Neural Networks. AIP Conference Proceedings. 2017;1855:040006. https://doi.org/10.1063/1.4985502

13. Thube DT. Artificial Neural Network (ANN) Based Pavement Deterioration Models for Low Volume Roads in India. International Journal of Pavement Research and Technology. 2012;5:115–120.

14. Lingyi Yao, Qiao Dong, Jiwang Jiang, et al. Establishment of Prediction Models of Asphalt Pavement Performance Based on a Novel Data Calibration Method and Neural Network. Transportation Research Record. 2019;2673:66–82. https://doi.org/10.1177/0361198118822501

15. Shtayat A, Moridpour S, Best B, et al. An Overview of Pavement Degradation Prediction Models. Journal of Advanced Transportation. 2022;2022:7783588. https://doi.org/10.1155/2022/7783588

16. Mazari M, Rodriguez DD. Prediction of Pavement Roughness Using a Hybrid Gene Expression Programming-Neural Network Technique. Journal of Traffic and Transportation Engineering (English Edition). 2016;3:448–455. https://doi.org/10.1016/j.jtte.2016.09.007

17. Mosa AM. Neural Network for Flexible Pavement Maintenance and Rehabilitation. Applied Research Journal. 2017;3:114–129.

18. Ceylan H, Gopalakrishnan K, Bayrak MB. Neural Networks Based Concrete Airfield Pavement Layer Moduli Backcalculation. Civil Engineering and Environmental Systems. 2008;25:185–199. https://doi.org/10.1080/10286600701838667

19. Elshamy MM, Tiraturyan AN, Uglova EV, et al. Comparison of Feed-forward, Cascade-forward, and Elman Algorithms Models for Determination of the Elastic Modulus of Pavement Layers. In: Proc. 2021 4th International Conference on Geoinformatics and Data Analysis. 2021. P. 46–53. https://doi.org/10.1145/3465222.3465235

20. Ceylan H, Gopalakrishnan K, Bayrak MB, et al. Noise-Tolerant Inverse Analysis Models for Nondestructive Evaluation of Transportation Infrastructure Systems Using Neural Networks. Nondestructive Testing and Evaluation. 2013;28:233–251. https://doi.org/10.1080/10589759.2012.742084

21. Issa A, Samaneh H, Ghanim M. Predicting Pavement Condition Index Using Artificial Neural Networks Approach. Ain Shams Engineering Journal. 2022;13:101490. https://doi.org/10.1016/j.asej.2021.04.033

22. Taher KA, Jisan BMY, Rahman MM. Network Intrusion Detection Using Supervised Machine Learning Technique with Feature Selection. In: Proc. 2019 International Conference on Robotics, Electrical and Signal Processing Techniques (ICREST) – IEEE. 2019. P. 643–646. https://doi.org/10.1109/ICREST.2019.8644161

23. García JAR, Castro M. Analysis of the Temperature Influence on Flexible Pavement Deflection. Construction and Building Materials. 2011;25:3530–3539. https://doi.org/10.1016/j.conbuildmat.2011.03.046

24. Donovan P, Tutumluer E. Falling Weight Deflectometer Testing to Determine Relative Damage in Asphalt Pavement Unbound Aggregate Layers. Transportation Research Record. 2009;2104:12–23. http://dx.doi.org/10.3141/2104-02

25. Elshamy MMM, Tiraturyan AN, Uglova EV, et al. Development of the Non-destructive Monitoring Methods of the Pavement Conditions via Artificial Neural Networks. Journal of Physics: Conference Series. 2020;1614:012099. https://doi:10.1088/1742-6596/1614/1/012099

26. Stubstad R, Carvalho R, Briggs R, et al. Simplified Techniques for Evaluation and Interpretation of Pavement Deflections for Network-Level Analysis: Guide for Assessment of Pavement Structure Performance for PMS Applications. Turner-Fairbank Highway Research Center; 2012. P. 34. — URL: https://www.fhwa.dot.gov/publications/research/infrastructure/pavements/ltpp/12025/12025.pdf

Received 09.08.2022
Revised 29.08.2022
Accepted 08.09.2022

About the Authors:

Mohamed Mostafa Mahmoud Elshamy, PhD student of the Motorways Department, Don State Technical University (1, Gagarin sq., Rostov-on-Don, 344003, RF), assistant lecturer at Faculty of Engineering, Al-Azhar University (1, Al Mokhaym Al Daem St., Cairo, Nasr-City, 11884, Arab Republic of Egypt), ScopusID, ORCID, mm.elshamy85@gmail.com

Tiraturyan, Artem N., associate professor of the Motorways Department, Don State Technical University (1, Gagarin sq., Rostov-on-Don, 344003, RF), Dr.Sci. (Eng.), associate professor, ScopusID, ResearcherID, ORCID, tiraturjan@list.ru

Uglova, **Evgeniya V.,** associate professor of the Motorways Department, Don State Technical University (1, Gagarin sq., Rostov-on-Don, 344003, RF), Dr.Sci. (Eng.), professor, ScopusID, ResearcherID, ORCID, uglova.ev@yandex.ru

Mohamed Zakaria Elgendy, lecturer at the Faculty of Engineering, Al-Azhar University (1, Al Mokhaym Al Daem St., Cairo, Nasr-City, 11884, Arab Republic of Egypt), ScopusID, ORCID, mohamedelgendy@azhar.edu.eg

Claimed contributorship:

M. M. M Elshamy: preparation of the text; preparation of the results and graphs; formulation of conclusions. A. N. Tiraturyan: a review of literature sources, calculations, computational analysis, analysis of the research results. E. V. Uglova: basic concept formulation; formulation of the research objective and tasks; academic advising; text processing; correction of the conclusions. M. Z. Elgendy: the text revision; discussion of the results.

Conflict of interest statement

The authors do not have any conflict of interest.

All authors have read and approved the final manuscript.

INFORMATION TECHNOLOGY, COMPUTER SCIENCE, AND MANAGEMENT

UDC 004.032.26, 531.3:625.7
https://doi.org/10.23947/2687-1653-2022-22-3-285-292

Original article

Solving the Problem of Determining the Mechanical Properties of Road Structure Materials Using Neural Network Technologies

Natalia E. Babushkina ✉, Alexandr A. Lyapin
Don State Technical University, 1, Gagarin sq., Rostov-on-Don, Russian Federation
✉ copybird@yandex.ru

Abstract

Introduction. Determination of mechanical properties of layered structures of highways is an urgent task. This is due, firstly, to the need to control the quality of new sections during the construction of highways. Secondly, to assess the condition of existing roads with the accumulation of damage and defects is of interest. The formation of multiple defects (cracks) changes the averaged viscoelastic properties of the components of the structure, specifically, the surface asphalt-concrete layers. The article discusses the use of neural network technologies to improve the accuracy of the recovery of viscoelastic properties. This approach is based on experimental methods. As an example, we can give the definition of the dynamic deflection of a structure from a falling weight, FWD.

Materials and Methods. The elastic modulus of a three-layer structure was determined on the basis of a neural network. To find out the solution accuracy, it was compared to the results of mathematical modeling and experimental data.

Results. The experimental and calculated parameters of the elastic modulus of individual layers of the road structure turned out to be very close. The proposed approach to determining the mechanical properties of materials of road structures allowed us to apply the obtained results to examination of the condition of individual elements and the entire road structure.

Discussion and Conclusions. The prospects of using artificial intelligence to determine the mechanical properties of layered structures was shown. Further improvement of methods and tools for analyzing the behavior of road structures under dynamic loading will expand existing approaches to assessing the condition of road structures.

Keywords: neural network, non-destructive testing, modulus of elasticity, regression analysis, multilayer network, impact indentation, neural network technologies.

Acknowledgments. The authors express their gratitude for the financial support of the research.

Funding information. The work was done on RFFI grant no. 22–29–01259, https://rscf.ru/project/22-29-01259/

For citation. N. E. Babushkina, A. A. Lyapin. Solving the Problem of Determining the Mechanical Properties of Road Structure Materials Using Neural Network Technologies. Advanced Engineering Research, 2022, vol. 22, no. 3, pp. 285–292. https://doi.org/10.23947/2687-1653-2022-22-3-285-292

Introduction. Assessment of the state of road structures enables to predict the process of road operation, plan the timing and volume of repair and restoration activities, affect the efficiency and safety of road transport. Non-destructive

testing methods are actively used[1]. In a number of scientific papers [1, 2], the authors noted the reliability and cost-effectiveness of this approach. The non-destructive methods include the determination of the dynamic deflection of a structure from a falling weight (FWD). This approach involves the registration of the degree of deflection of the road structure surface at a certain distance from the impact point. At the same time, during the installation, the elastic modulus of the layers is calculated, the load and thickness of the layers of the structure are determined.

One of the major scientific research objectives in this direction is to provide timely detection of defects and changes in the components of road structures. The researchers have identified the factor that influences the main characteristics of the dynamic stress-strain state of the "road structure — ground" system more than others. This is a change in the dynamic elastic modulus of the elements of the pavement, the base, and the ground [3–5].[2]

An alternative tool for monitoring the state of road surfaces can be a neural network trained according to the results of experiments [6, 7]. It is worth noting that neural networks are extensively used in the construction, including road construction. Neural networks are an effective tool for solving some classification problems, including construction. They help to perform regression analysis as well. The traditional approach to the construction of nonlinear models has a number of limitations. They are connected, firstly, with complex, hidden nonlinear relationships of the source data. Secondly, over time, it is possible to modify the structure of the links, which necessitates the transformation of the nonlinear model structure. The use of neural network technologies makes it possible to eliminate the disadvantages of the traditional approach. A neural network is able to independently determine functional dependences, approximate nonlinear functions with a given accuracy, and rebuild its architecture in the learning process. The above verifies the timeliness of the presented work.

Neural network technology opens up new opportunities for solving problems of design, optimization and diagnostics of building structures [8–11]. O. M. Maksimova writes that the possibility of additional training of the neural network provides refining the construction structure, improving its management [12]. In [13], it is noted that artificial intelligence can reduce the costs of companies, thanks to the timely diagnosis of construction projects. In [14], a broad overview of the possibilities of using neural networks in construction is presented. The author notes the multivariant use of artificial intelligence to solve a variety of complex nonlinear problems of forecasting, evaluation, optimization.

In [15], special attention is paid to the quality and state of the road network. Based on experimental data, two models are compared: multidimensional analysis and artificial neural network. They were developed to create a decision support system for assessing the operational condition of roads due to the hydrogeological situation. The author concludes that the neural network model is more reliable and efficient.

The selection of the type of neural network is of particular note. The authors [16] conclude that the type of neural network does not significantly affect the solution to the problem of calculating the elasticity modulus of the pavement layers. At the same time, the most similar results between the model and the target values were provided by a feedforward neural network model.

The study aims at solving the problem of reverse calculation of the elastic moduli for the dynamic deflection bowls from the impact of the FWD unit. The results of simulation of dynamic impact on the road structure, and those obtained by a neural network, are compared.

Materials and Methods. The dynamic effect of the FWD unit was simulated with the help of the program for calculating wave fields in the structure. The model of axisymmetric deformation of the medium used in the calculation can be analytically described as a multilayer half-space D, consisting of N layers in a cylindrical coordinate system (R, θ, Z). The axis of symmetry OZ is directed vertically upwards and is orthogonal to the boundary plane of the half-space and its layers (Fig. 1).

[1] Eremin RA, Kulizhnikov AM, Pudova NG. Metodika kompleksnogo obsledovaniya dorozhnoi odezhdy avtomobil'nykh dorog s primeneniem metodov nerazrushayushchego kontrolya. In: Proc. 16th All-Russian Sci.-Pract. Conf. of Survey Contractors. Moscow: Geomarketing; 2021. P. 438–446. (In Russ.)

[2] Qinwu Xu. Development of a Computational Method for Inverting Dynamic Moduli of Multilayer Systems with Applications to Flexible Pavements under FWD Tests: dis. … doc. of philos. Texas, 2014. 223 p.

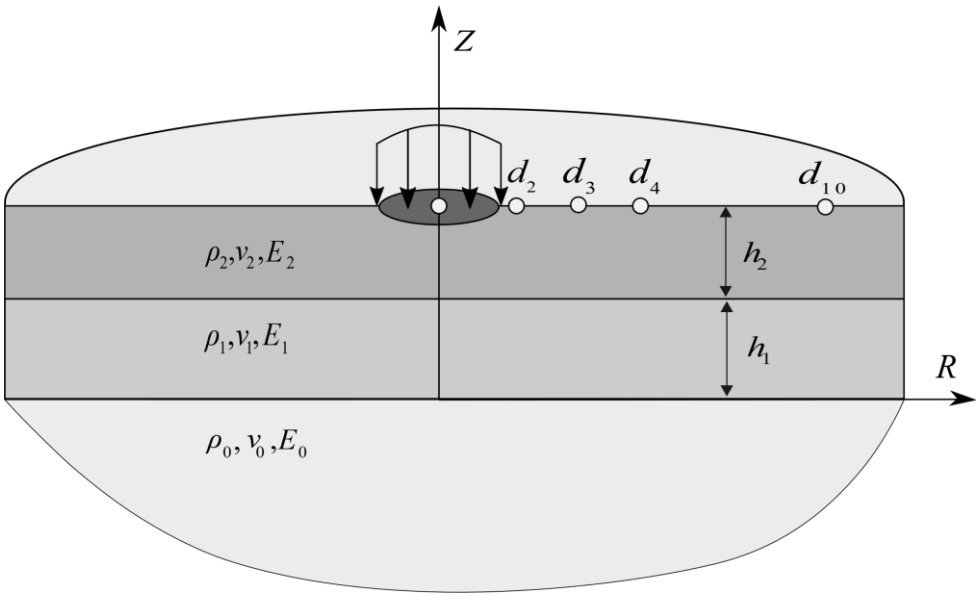

Fig. 1. Multilayer construction of pavement in longitudinal section

The medium motions are described by the dynamic Lamé equations in displacements for a homogeneous linear elastic material within each layer:

$$(\lambda + 2\mu)\,\mathrm{grad\,div}\,u(r,t) - \mu\,\mathrm{rot\,rot}\,u(r,t) = \rho\ddot{u}(r,t), \quad (1)$$

where $u = (u_R, u_Z)$ — displacement vector, r — radius vector of the observation point, λ, μ — Lamé elastic coefficients, ρ — material density.

The layers of half-space D are rigidly fastened to each other. When passing through flat interface boundaries, the displacement and stress vectors must match (σ_z, τ_{zr}).

Each layer of the half-space has the following characteristics: thickness h_i, density ρ_i, elasticity modulus $E_i = \mu_i \frac{3\lambda_i+2\mu_i}{\lambda_i+\mu_i}$, Poison's ratio $\nu_i = \frac{0{,}5\,\lambda_i}{\lambda_i+\mu_i}$.

Boundary conditions for stress vector $s = (\sigma_z, \tau_{zr})$ at the upper boundary of the multilayer medium D, distributed over the spot radius r_0 of the contact between the wheel and the road structure, can be written as:

$$\sigma_z(R,t) = \begin{cases} P_0 sin\left(\frac{\pi t}{\tau}\right), t \in [0,\tau] \\ 0, t > \tau \end{cases}, \tau_{zr} = 0, \quad (2)$$

where P_0 — constant intensity of impact loading with duration τ.

To solve the problem, the integral Hankel transform is used in the radial Fourier coordinate and in time. As a result, a representation of the wave field is obtained:

$$u(r,t) = \int_0^\infty d\omega exp(-i\omega t) \int_0^\infty Q(u,\omega) \cdot S(u,\omega) J_{0,1}(uR) u du. \quad (3)$$

Here, $S(u,\omega)$ — the Fourier–Hankel transform from the external load vector s; $Q(u,\omega)$ — Green's matrix–function for a multilayer half-space obtained through the superposition principle as a sum of matrices for homogeneous half-space, as in [4].

To analyze the properties of the structure in solving the inverse problem, the results of experimental measurements of the bowl of dynamic deflections at specified observation points on the surface $R = d_k$, $k = 1, 2, ..., 10$, are used. The average distance between them is 0.3 m. The measured characteristic at each point on the surface:

$$\max_t |u_z(d_k,t)|.$$

Figure 2 shows an example of the behavior of vertical deflection functions over time for a typical three-layer road structure.

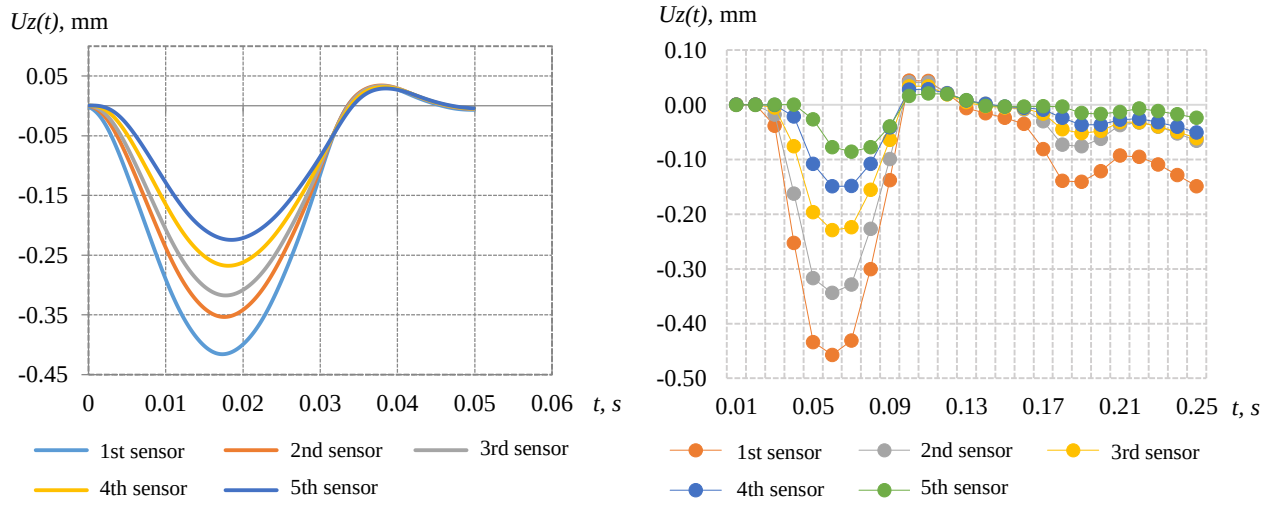

a) *b*)

Fig. 2. Time dependences of vertical deflections $u_z(d_k, t)$: *a* — simulation data; *b* — experimental data

The procedure for restoring the elastic modulus of structure E_i is based on minimizing the quadratic error function:

$$F(E_i) = \sum_{k=1}^{10}\left(\xi_k(E_i) - \xi_k^{exp}\right)^2,$$

where ξ_k^{exp} were obtained from an experiment using the FWD unit. The Levenberg-Marquardt method was chosen as the minimization algorithm. The elements of the gradient and the Hesse matrix of function F were calculated through finite differences of the 1st order. At the same time, the output of elastic modules E_i beyond the physical ranges of changes in these parameters was controlled.

To solve the problem with the help of neural networks, a standard pavement design was considered (Table 1).

Table 1

Experiment pavement design

Structural elements	Thickness, cm	Elastic modulus limits, MPa	
		upper	bottom
Asphalt concrete layer	10	4,200	1,200
Crushed-stone layer	44	1,500	100
Ground	∞	300	20

Table 1 shows the main structural elements of the road section under study. The model was constructed with a maximum elastic modulus (4,200 MPa), since the experimental measurement results were tied to an average air temperature of 20 °C. To determine the elastic modulus in the winter period, it is required to recalculate the indicators.

A fully connected neural network was implemented in Python using Keras deep learning library. Basic network parameters were as follows:

– 300, 30, 3 neurons in layers;

– 3,000 eras of learning.

The activation function in the hidden layers was ReLu, in the output layer — sigmoid. The network processed normalized data in the range from 0 to 1. After network calculations, denormalization into a numerical form was performed. The neural network was trained on a data set of 1,000 values obtained under modeling. On average, the error of neural network calculations on the test set was within 10%.

The neural network inputs were bowls of dynamic deflections. Figure 3 shows them at different moduli of elasticity of the layers of the road structure. The network outputs are values of elastic moduli of structural elements of the pavement.

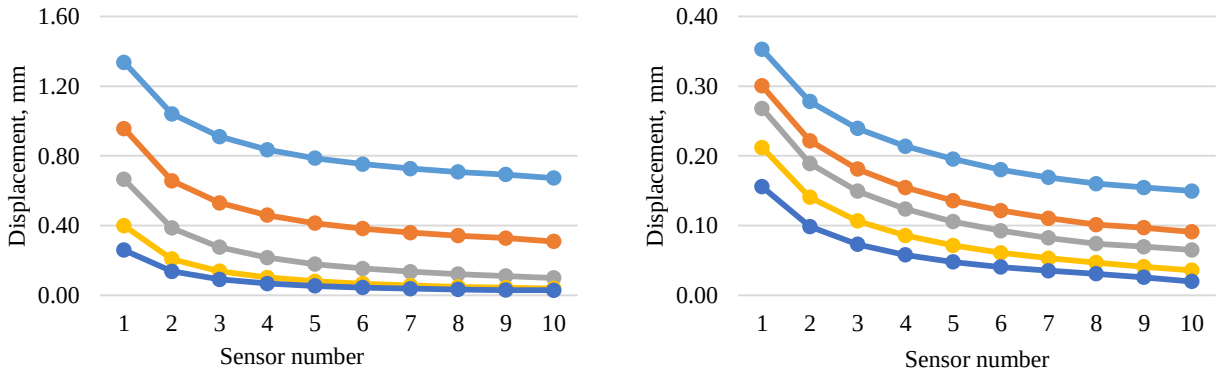

Fig. 3. Bowls of dynamic deflections with different elastic modules

Experimental data for the study were obtained using FWD unit on a road section with an asphalt concrete coating thickness of 10 cm, and a crushed stone layer thickness of 44 cm. The elastic moduli of the layers of road clothes were determined (Table 1). The layout of the sensors-geophones: 0 — 20 — 30 — 45 — 60 — 90 — 120 — 150 — 180 — 210 cm from the impact point.

Research Results. The authors have elucidated various combinations of structural elements:

– asphalt concrete layer + crushed stone layer;

– asphalt concrete layer + ground;

– crushed stone layer + ground;

– asphalt concrete layer + crushed stone layer + ground.

Let us study visualizations of the results of neural network calculations. Figure 4 shows the results obtained by the neural network during the test calculation for the 1st option. The accuracy of calculations exceeded 90 %.

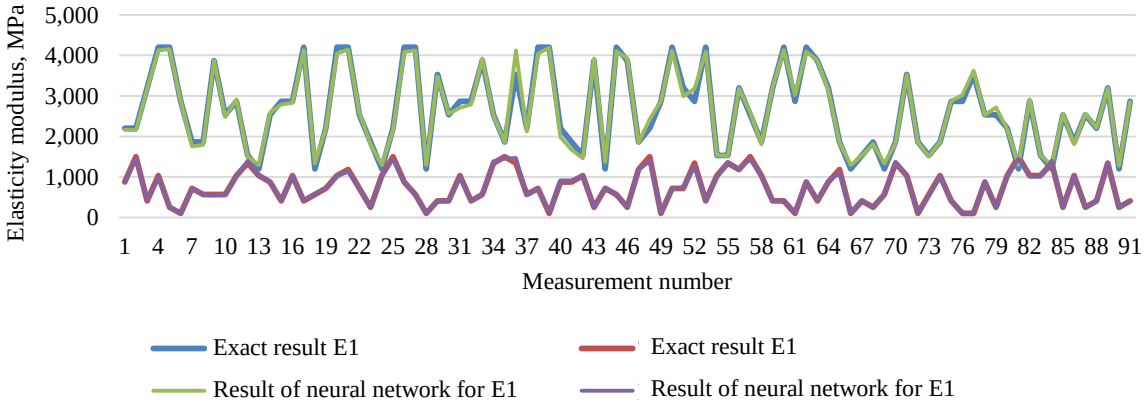

Fig. 4. Result of neural network training in option 1 — “asphalt concrete layer + crushed stone layer”

As for the test calculations for options 2 and 3, in general, the calculation results were close to the first one. Figure 5 shows a good result of neural network training on all layers of the structure. The presented values were obtained on the test set by a random sample.

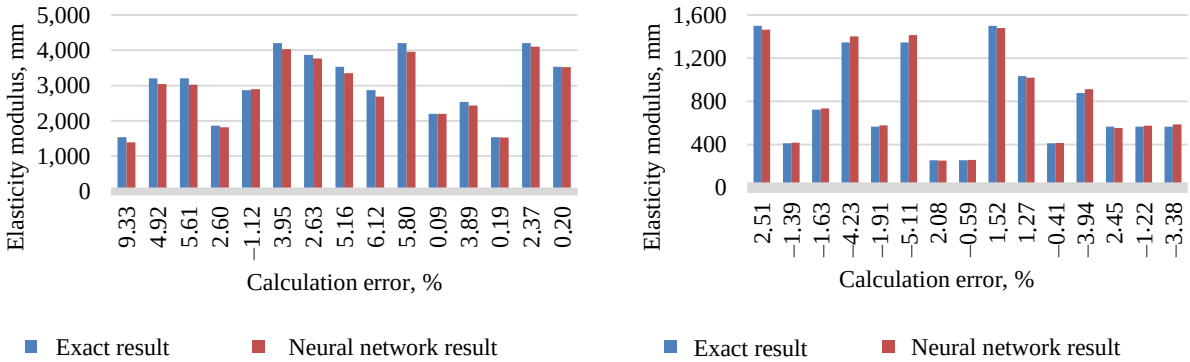

Fig. 5. Error of neural network calculations under option (1)

The graphical representation of the ratio of the expected and the obtained result of the elastic modulus in Figure 5 indicates insignificant errors in the test calculation of the layers of the road structure for option 1.

Special attention should be paid to the text calculation for option 4.

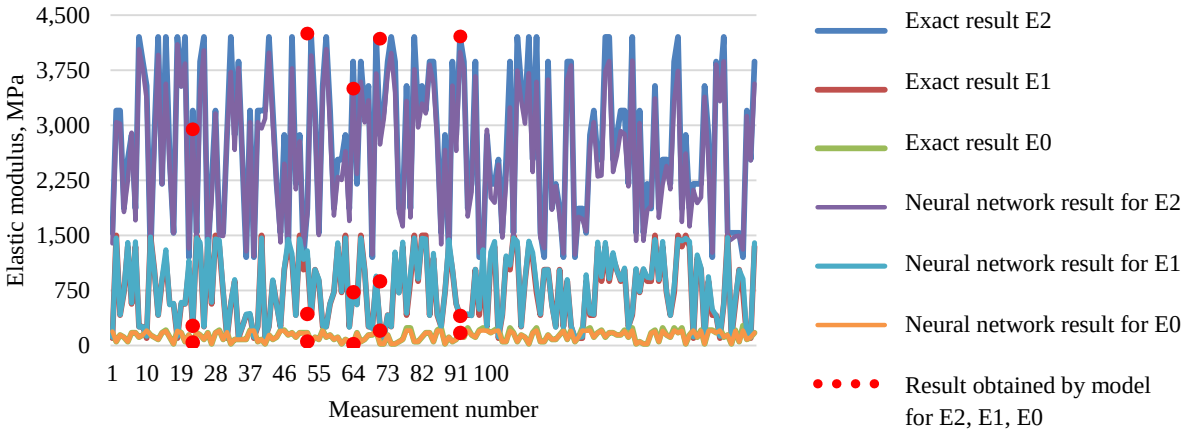

Fig. 6. Result of neural network training in option 4 — "asphalt concrete layer + crushed stone layer + ground"

Figure 7 shows the statistical distribution of the error of neural network calculations. Note that the average error of most measurements is about 10 %. However, in some cases, there is maximum deviation close to 23 % (on the histogram, this is a group of 20 % or more).

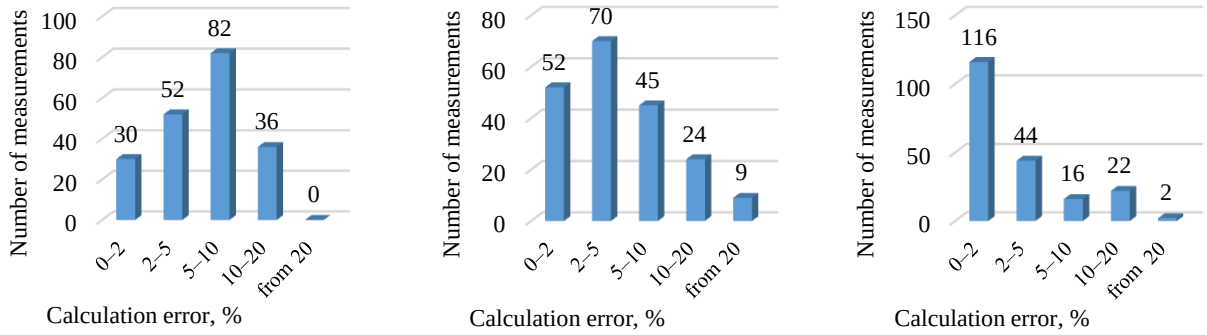

Fig. 7. Error of neural network calculations under option 4 — "asphalt concrete layer + crushed stone layer + ground": *a* — at $E_2 \in [1{,}200;\ 4{,}200]$ MPa; *b* — at $E_1 \in [100; 1{,}500]$ MPa; *c* — at $E_0 \in [20, 300]$ MPa

From the data in Figure 7, conclusions can be drawn about the accuracy of neural network calculations on the test set. In the first case (Fig. 7 *a*), we note that of the entire test set, 41 % (82 measurements) had an error in the range of 5–10 %. Similar indicators of 52 measurements (26 %) — 2–5 %. In 30 cases (15 %), values of 0–2 % were recorded. 36 measurements (18 %) yielded results of 10–20 %.

In Figure 7 *b*, the maximum indicator was 70 values for errors of 2–5 %. According to Figure 7 *c*, the results of calculations of the elastic modules of the ground had the smallest error. Thus, there are 116 values within 0–2 %. This is 58 % of the test set. 44 and 16 values are within 10 % of the error (22 % and 8 %, respectively).

Discussion and Conclusions. Hence, neural network technology has proved to be an effective tool for determining the mechanical properties of materials of road structures. When solving the inverse problem, a high degree of recovery of the elastic modulus values was noted. The average error of calculations did not exceed 10 %.

The neural network training options according to the values of the elastic moduli of the layers were studied. The error recorded in these cases was mainly due to insufficient training of the network. To solve the problem, it is required to increase the amount of data for training.

The results of the neural network technology application were consistent with the experimental data obtained after the operation of the FWD dynamic loading unit.

References

1. Fedosov AV, Gaynullina LA. Methods of Non-Destructive Testing. Electrical and Data Processing Facilities and Systems. 2015;11:73–78.

2. Kychkin VI, Jushkov VS. Not Destroying Dynamic Quality Monitoring of Road Clothes. Naukovedenie. 2013;14:34.

3. Uglova EV. Estimation of Modules of Elasticity of Road Construction Layers at the Stage of Highways Operation. Journal of Construction and Architecture. 2009;23:170–178.

4. Uglova EV, Tiraturyan AN, Liapin AA. Integrated Approach to Studying Characteristics of Dynamic Deformation on Flexible Pavement Surface Using Nondestructive Testing. PNRPU Mechanics Bulletin. 2016;2:111–130. https://doi.org/10.15593/perm.mech/2016.2.08

5. Titaturjan AN, Olkhovoy SA. Evaluation of Strength Degradation of Non-rigid Road Constructions on the Basis of Field Measurements at the Site of the Highway M4 “Don” p. Tarasovskiy. Engineering Journal of Don. 2017;45:122.

6. Babushkina N, Lyapin A, Kovaleva A. Analysis of Neural Network Results Based on Experimental Data during Indentation. E3S Web of Conferences. 2020;224:01018. 10.1051/e3sconf/202022401018

7. Babushkina N, Lyapin A. Solving the Problem of Classification of Material Properties Using a Neural Network. Journal of Physics Conference Series. 2021;2131:032084. https://doi.org/10.1088/1742-6596/2131/3/032084

8. Kulkarni PS, Londhe SN, Deo MC. Artificial Neural Networks for Construction Management: A Review. Journal of Soft Computing in Civil Engineering. 2017;1/2:70–88. 10.22115/SCCE.2017.49580

9. Baturina NYu. Neuronetwork Models in Research Problems Construction Designs. Engineering Journal of Don. 2013;27:201.

10. Elfaki AO, Alatawi S, Abushandi E. Using Intelligent Techniques in Construction Project Cost Estimation: 10-Year Survey. Advances in Civil Engineering. 2014. Art. 107926. https://doi.org/10.1155/2014/107926

11. Patel DA, Jha KN. Evaluation of construction projects based on the safe work behavior of co-employees through a neural network model. Safety Science. 2016:89:240–248. https://doi.org/10.1016/J.SSCI.2016.06.020

12. Maksimova OM. Neuronet Technology Development and Application for Solving Mechanical and Engineering Structures Problems. Proceedings of Irkutsk State Technical University. 2013;79:81–89.

13. Gazarov AR. Advantages of Using Artificial Intelligence in the Field of Construction. Izvestiya Tula State University. 2020;4:136–139.

14. Waziri BSh, Bala K, Bustani ShA. Artificial Neural Networks in Construction Engineering and Management. International Association for Sustainable Development and Management (IASDM). 2017;6:50–60. 10.7492/IJAEC.2017.006

15. Dell’Acqua G, De Luca M, Zilioniene D. Using Artificial Neural Network and Multivariate Analysis Techniques to Evaluate Road Operating Conditions. Journal of Risk Research. 2018;21:679–691. https://doi.org/10.1080/13669877.2016.1264445

16. Elshamy MMM, Tiraturyan AN, Uglova EV. Evaluation of the Elastic Modulus of Pavement Layers Using Different Types of Neural Networks Models. Advanced Engineering Research. 2021;21:364–375. https://doi.org/10.23947/2687-1653-2021-21-4-364-375

Received 14.06.2022
Revised 01.07.2022
Accepted 15.07.2022

About the Authors:

Babushkina, Natalia E., postgraduate student of the Information Systems in Civil Engineering Department, Don State Technical University (1, Gagarin sq., Rostov-on-Don, 344003, RF), ScopusID, ORCID, copybird@yandex.ru

Lyapin, Alexandr A., Head of the Information Systems in Civil Engineering Department, Don State Technical University (1, Gagarin sq., Rostov-on-Don, 344003, RF), Dr.Sci. (Phys.-Math.), professor, ScopusID, ORCID, lyapin.rnd@yandex.ru

Claimed contributorship:

N. E. Babushkina: concept formulation; research objectives and tasks; computational analysis; text preparation; conclusions. A. A. Lyapin: academic advising; analysis of the research results; the text revision; correction of the conclusions.

Conflict of interest statement

The authors do not have any conflict of interest.

All authors have read and approved the final manuscript.